DELFT UNIVERSITY OF TECHNOLOGY

AEROSPACE ENGINEERING

AERODYNAMICS, WIND ENERGY AND PROPULSION

An experimental investigation of crossflow instability interaction with forward facing steps

Author
Niveditha RAJENDRAKUMAR

Supervisor
Marios KOTSONIS
Co-supervisor
Alberto Felipe Rius VIDALES

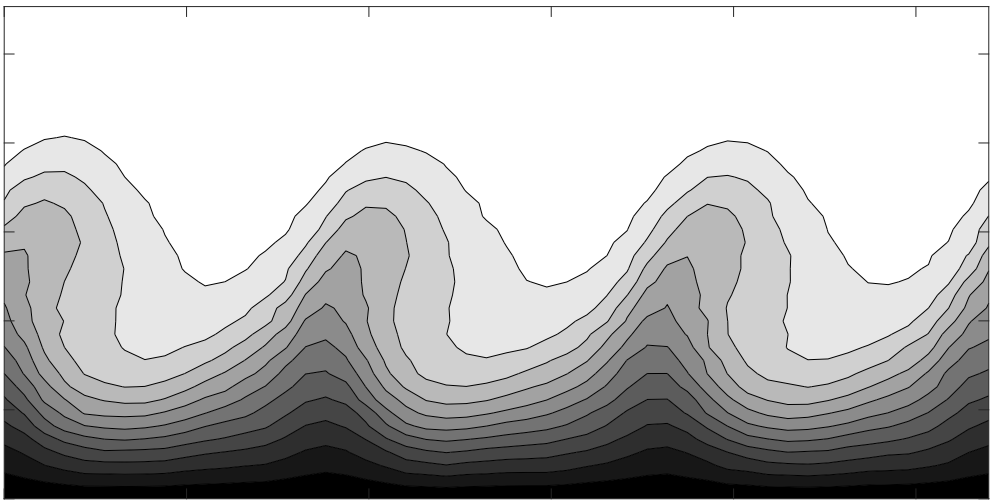

AN EXPERIMENTAL INVESTIGATION OF CROSSFLOW INSTABILITY INTERACTION WITH FORWARD FACING STEPS

A thesis submitted to the Delft University of Technology in partial fulfillment
of the requirements for the degree of

Master of Science in Aerospace engineering

by

Niveditha RAJENDAKUMAR

September 30th, 2021

Student number: 5020425

Thesis Committee:

Dr.Marios Kotsonis, TU Delft, Associate professor
Dr.Daniele Ragni, TU Delft, Associate professor
Dr.Theo Michelis, TU Delft, Postdoctoral researcher
Ir.Alberto Felipe Rius Vidales, TU Delft, PhD Candidate

An electronic version of this thesis is available at http://repository.tudelft.nl/.

CONTENTS

PREFACE

The past nine months have been enriching to say the least, filled with a lot of learning and new experiences. There have been good days, and not so good days but I was grateful to have shared these days with the few people that I would like to thank here in my thesis.

I'm grateful for the constant stream of advice and guidance from my supervisor Dr. Marios Kotsonis. I thoroughly enjoyed my meetings with Marios, where his insightful feedback would push me to sharpen my thinking. I'd like to express my gratitude to my daily supervisor, Beto for his patience and support when I was finding my bearings during my work at the lab. I learned a great amount during our discussions and appreciate his time and effort for making my time at the lab a memorable experience.

Special thanks to Giulia, Theo, Kaisheng and Alessandro for offering their expertise and helping out in my preparation for the experimental campaigns. I'm also grateful for the technical support offered by Stefan and Emiel. I appreciate the support of my colleagues Joerie, Marina and Kristie, without whom the long hours in the wind tunnel would not have been as enjoyable.

I was lucky to have the emotional support of my friends and housemates: Snigdha, Praneetha, Harshini and Martijn, also to have had my friends back home Tanya, Drisya, Mercy and Heera for their love and encouragement. Lastly, ofcourse thanks Appa, Amma, Mithi and Varsha for being my rock.

Niveditha Rajendakumar
Delft, September 2021

ABSTRACT

The growing need to curtail emissions in commercial aerospace motivates research focussed on drag reduction on swept wings. A possible solution is the application of laminar flow control (LFC) techniques to delay laminar-turbulent boundary layer transition. To ensure the effective and robust application of LFC in real flight environments, there have been research efforts focussed on the fundamental study of the transition mechanism prevalent on swept wings.

Crossflow instability develops on three-dimensional boundary layers subject to a favorable pressure gradient and are sensitive to the presence of surface roughness. Previous research efforts on the interaction of stationary crossflow vortices with forward facing steps have shone light on the various factors at play. One such factor is the effect of initial crossflow amplitude.

Experimental measurements are performed on a 45^o swept flat plate model at the low speed laboratory (LSL) at the Delft University of Technology, in a low turbulence environment to stimulate the development of stationary crossflow. The swept flat plate model is equipped with two linear manual stages to create forward and backward facing steps. Preliminary measurements characterize the pressure gradient over the swept flat plate model under study. In the preliminary study , hot-wire anemometry (HWA) measurements characterize the flow over the swept plate without steps over a large chordwise domain with and without forcing by discrete roughness elements (DREs). The DREs are spaced at a spanwise wavelength corresponding to the overall maximum N factors from LST. The mean velocity contours and N factor trends presented in these measurements reinforced the need for DREs to control flow. Spectral content is monitored and the frequency bands associated with probe vibration and travelling crossflow interaction were delineated.

Infrared thermography was employed to observe the movement of transition front with varying step heights and initial crossflow amplitudes. When the DRE height increases, the transition front moves upstream consistently for all step heights. Furthermore, when the DRE height is kept a constant , but the array is moved upstream and downstream of the neutral point, the transition front moves upstream for all step heights. In order to observe the flow in the vicinity of the step, HWA was once again used to quantify the interaction of crossflow with FFS. The clean, short FFS and supercritical step height configurations identified from the IR study, are studied for two initial amplitudes. For the supercritical step configuration, bandpass filtered fluctuations are found to align with a high wall normal and spanwise shear region which has been identified in previous work. It is postulated to be associated with a vortex shedding mechanism, for which frequency bands are delineated. Estimates of the range of recirculation bubble length were made and a flapping frequency range was also demarcated. In this study, a vortex shedding scenario is used to explain the presence of these near wall fluctuations. To conclude the report, recommendations are made for extending the present study for future work.

List of Figures

LIST OF TABLES

List of Symbols and Abbreviations

α	Angle of attack/Streamwise wavenumber
β	Spanwise wavenumber
ρ	Density
μ	Dynamic viscosity
ν	Kinematic viscosity
Λ	Sweep angle
δ^*	Displacement thickness
θ^*	Momentum thickness
$\epsilon_{\overline{Q}}$	Statistical uncertainty of mean velocity
ψ	Angle of instability with streamwise direction
	ϕ Eigenfunction
C_p	Coefficient of pressure
c_X	Airfoil chord
c_x	Airfoil chord in orthogonal reference frame
N	N factor
q	Dynamic pressure
Q	Resultant velocity
h	Step height
$Re_{c,X}$	Chord Reynolds number
Tu	Turbulence intensity
U, V, W	Velocities in wind tunnel coordinate system
u, v, w	Velocity components in swept wing coordinate system
u_s, v_s, w_s	Velocity components along inviscid streamline
X, Y, Z	Axes in wind tunnel coordinate system
x, y, z	Axes in swept wing coordinate system
x_s, y_s, z_s	Axes in invisid streamline coordinate system
$U_{\overline{Q}}$	Uncertainty of mean velocity
ALC	Attachment line contamination
BFS	Backward facing step
CFI	Crossflow instability
CFV	Crossflow vortex
DRE	Discrete roughness element
DNS	Direct numerical simuation
FFT	Fast fourier transform
FFS	Forward facing step

HWA	Hot wire anemometry
IR	Infrared thermography
LE	Leading edge
LFC	Laminar flow control
LSB	Laminar separation bubble
LTT	Low turbulence tunnel
LST	Linear stability theory
PIV	Particle image velocimetry
TS	Tollmien-Schlichting
TE	Trailing edge
OS	Orr-Sommerfeld
PSD	Power spectral density
PET	Polyethylene terephthalate

1

INTRODUCTION

Drag is an important factor which plays to the disadvantage of the aerodynamic performance of any aircraft. Minimizing drag on a commercial transport aircraft could prove to be a solution to improving fuel efficiency [19]. Total drag is made up to include pressure and skin friction drag. While pressure drag is controlled by the shape of the body, the skin friction drag coefficient has a unique inverse proportionality with the Reynolds number over the lifting surfaces. The expressions provided in the next chapter will show that skin friction drag associated with turbulent boundary layers is larger than that in laminar boundary layers, for similar Reynolds numbers. A study conducted by Thibert et al. at Onera [35] showed that the skin friction drag contributes to about half of the total drag in a subsonic transport aircraft. Thus, it becomes desirable to capitalize on the lower drag of laminar boundary layers. To achieve laminar flow over a greater portion of the airfoil, one must look into delaying laminar-turbulent boundary layer transition. Transition from laminar flow to turbulence is a direct consequence of the growth of perturbations inside the boundary layer. This brings the reader to the domain of laminar flow control (LFC) : LFC works towards restricting the growth of these disturbances. The four instability types which could cause transition in flight conditions are: Tollmien-Schlichting (TS) waves, Crossflow (CF) vortices, Attachment line contamination (ALC) instability, and Görtler vortices.

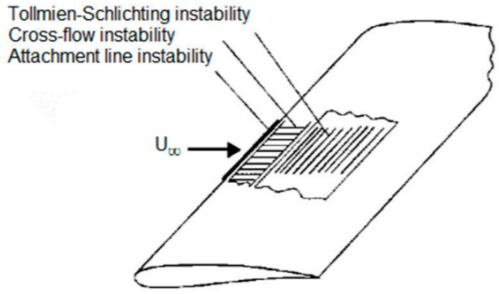

Figure 1.1: Swept wing representing the various mechanisms of transition on its surface (Reproduced from [26])

There have been different laminar flow control strategies employed to stabilize the boundary layer specifically designed for each of the instability types. Saric et al. [71] recommend various strategies to implement passive flow control transonic transport aircraft. Uniform wall suction is a strategy which is found to stabilize Tollmien-Schlichting waves (TS), attachment line contamination (ALC), Görtler and Crossflow (CF) vortices. Weak wall suction was incorporated in Pfenninger's X-21 ([66]) where laminar flow was achieved at transition Re of 27×10^6 with a 20 % reduction in total drag. It was also incorporated by means of a Krueger flap to facilitate hybrid LFC on the Boeing 757 ([22] cited by [71]). Another method involved the development of a flat plate wherein the sweep was reduced to stabilize CF instabilities and an accelerating pressure gradient was imposed to stabilize TS waves . This method was studied extensively in the development of the Aerion supersonic jet ([31]). A third method [71] suggested polishing the leading edge to minimize the surface roughness from which stationary crossflow vortices draw their initial amplitude. Finally, spanwise periodic distributed roughness elements (DREs) were investigated [71]. A double layer of

DREs about $12\mu m$ high, spaced at half the critical wavelength resulted in the transition location being pushed back to around 60% of the chord, thus doubling the laminar flow region.

Notwithstanding the low drag incurred, laminar boundary layers are notorious for flow separation. Laminar boundary layer flow is not characterized by mixing of flow but instead by parallel uniform streamlines. Thus, it is sensitive to transition to turbulence in the presence of even minor protuberances/excrescences or acoustic disturbances on lifting surfaces. These imperfections can be operational in nature which includes accumulation of insects, dirt, erosion, atmospheric ice crystals, and foreign object damage. They could be due to surface irregularities from manufacturing processes which include panel joints, seams, seals and paint. They could also arise from acoustic sources such as propulsion systems and airframe noise [7]. Consequently, the implementation of LFC on laminar boundary layers in flight conditions subject to any of the above disturbances, is difficult to achieve. This difficulty is highlighted by Saric and Reed [72] where they address the challenges which could be faced in the implementation of LFC in unswept and swept wings and specify the importance of ensuring a smooth surface, particularly avoiding steps and gaps to maintain the effectiveness of LFC techniques. Spanwise invariant surface excrescences which present as forward and backward facing steps and gaps have been studied experimentally and computationally as a topic of interest in designing for effective LFC ([30], [48] , [47]). Of forward and backward facing steps, studies ([76], [32], [30]) have shown that forward facing steps are the preferred surface irregularity, owing to the observations that they are associated with a smaller transition movement towards the step with respect to their backward facing counterparts.

On identifying that LFC techniques are most sensitive to smoothness of the surface, the logical next step would be to study how transition to turbulence occurs in the presence of the surface irregularities. Bushnell [12] in his review of laminar flow control highlights that the fundamental issue in the implementation of LFC lies in the identification and categorization of the mechanism for transition. The two classes of transition distinguished by the amplitude of disturbances are: natural and bypass. Natural transition is described initially by linear stability theory. The transition process proceeds in an ordered fashion : the boundary layer becomes receptive to the instability, following which the amplification of instability ensues, pushing the development of secondary instabilities leading to laminar flow breakdown. This is prevalent when the disturbances are small. However, for large amplitude disturbances, the linear instability amplification is bypassed and the flow directly goes to nonlinear laminar flow breakdown [74]. Jones [10] discusses the investigations in 1930 which reported that small roughness and waviness at high Reynolds number (Re) has potential for the reduction of the extent of laminar flow. The existence of an imperfection stimulates eigenmodes into the boundary layer. Here, transition to turbulence can occur in one of two ways based on the height of the imperfection: When the height of the imperfection or the Re increases, flow separation carrying with it inflectional velocity profiles can occur. So, the inviscid instability can grow and induce transition. Else, if the imperfection size is large enough, the linear amplification is bypassed and nonlinear transition processes arise.

Besides the amplitude of disturbances, out of the transition mechanisms (listed above) which arise in swept wing flows widely employed in subsonic transport aircraft, the crossflow instability is the most relevant. This is because other instabilities have shown to be suppressed by geometrical modifications made to the wing. Over the past two decades, computational and experimental research has been focussed on the transition mechanism at play when crossflow vortices interact with steps and gaps ([48], [3], [5], [41], [29]) on swept flat plate and swept wing boundary layers. While there have been great strides made in the study of growth and development of CF vortices, there remains much to be understood with respect to the mechanism behind the interaction of crossflow vortices with steps. Hereinafter, state of the art experimental and numerical investigations are required to obtain acceptable manufacturing tolerances to put laminar flow control into operational service.

2

PHYSICAL BACKGROUND

The following chapter presents the theoretical background which would be useful for the reader in following the upcoming sections of text. The chapter addresses the various boundary layer parameters, the steps involved in laminar-turbulent boundary layer transition, and linear stability theory, all of which would be referenced further on within this report.

2.1. BOUNDARY LAYER THEORY

As mentioned previously, laminar turbulent transition is initiated by the growth of disturbances within the boundary layer. Thus, the key concepts of the boundary layer are essential for understanding the process of transition. But first, what is the boundary layer? For application to aerospace, we will be restricting our study to the flow of air. The viscosity of a fluid such as air is not high (at 25 °C, $\mu = 18.37 \times 10^{-6}$ Ns/m^2), thus air flow is associated with high Reynolds number which is defined as the ratio of inertial force to viscous force. However, this lack of viscosity for the flow of air is not indicative of the entire domain. For instance, at the wall, the velocity must go to zero by the no-slip condition. To facilitate the no-slip condition , air flow can be divided into two unequal regions: the thin flow region close to the wall surface where viscous effects are not neglected and the bulk flow region away from the wall surface where the viscous effects can be neglected. The thin region close to the wall where viscous effects are dominant, is called the boundary layer. This division of the flow field into inviscid flow and the boundary layer brings with it simplifications to how the air flow over a wall can be treated. [26].

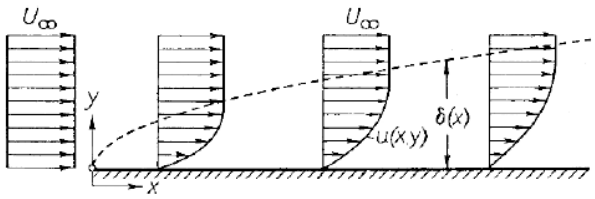

Figure 2.1: Laminar boundary layer development over flat plate (Reproduced from [26])

Considering a flow over a flat plate as illustrated in Figure 2.1, the layer of fluid particles retarded by the wall due to viscosity increases in thickness as one proceeds downstream. This implies that the thickness of the boundary layer increases as the distance from the leading edge increases. However, the boundary layer thickness is an artificial parameter introduced in fluid mechanics to demarcate the continuous transition from boundary layer flow to inviscid flow. In practice, the boundary at every streamwise location is taken to be the points where the local velocity reaches 99% of the undisturbed external velocity U_e and this thickness is given as $\delta_{99}(x)$. This parameter for the laminar boundary layer is estimated by equating the inertial and viscous forces since the forces are in equilibrium in this case [26]. The exact solution of Blasius equation gives the approximation parameter for laminar boundary layer thickness. The boundary layer thickness for the turbulent boundary layer is estimated from Prandtl's one-seventh law and the Von Karman integral momentum equation. The expressions for the laminar and turbulent boundary

layer thicknesses are given to be the following:

$$\left(\frac{\delta_{99}}{x}\right)_{laminar} = \frac{5.0}{\sqrt{Re_x}} \qquad \left(\frac{\delta_{99}}{x}\right)_{turbulent} \approx \frac{0.38}{(Re_x)^{1/5}} \tag{2.1}$$

where Re_x is the Reynolds number at a local streamwise location x. Furthermore, the thickness can be defined by the amount by which the inviscid streamlines are displaced by the boundary layer. This definition gives rise to the parameter called displacement thickness $\delta^*(x)$ and it is given by the following formula:

$$\delta^*(x) = \int_0^\infty \left(1 - \frac{u}{U_e}\right) dy \tag{2.2}$$

The displacement thickness expressions for the laminar and turbulent boundary layers are given to be the following:

$$\left(\frac{\delta^*}{x}\right)_{laminar} = \frac{1.72}{\sqrt{Re_x}} \qquad \left(\frac{\delta^*}{x}\right)_{turbulent} \approx \frac{0.048}{Re_x^{1/5}} \tag{2.3}$$

The displacement thickness $\delta*$ is about 1/3 of the δ_{99}. When the thickness is defined by the integral drag on the flat plate, this definition gives rise to the parameter called momentum thickness θ . The momentum thickness is given by the following formula:

$$\theta(x) = \int_0^\infty \frac{u}{U_e}\left(1 - \frac{u}{U_e}\right) dy \tag{2.4}$$

The momentum thickness expressions for the laminar and turbulent boundary layers are given to be the following:

$$\left(\frac{\theta}{x}\right)_{laminar} = \frac{0.664}{\sqrt{Re_x}} \qquad \left(\frac{\theta}{x}\right)_{turbulent} \approx \frac{0.037}{Re_x^{1/5}} \tag{2.5}$$

In addition to the displacement and momentum thickness, the skin friction coefficient is an important parameter in judging when a flow is laminar or turbulent. Laminar boundary layer is associated with parallel streamlines, wherein the lack of mixing within the boundary layer is attributed to the decreased skin friction drag. On the other hand, turbulent boundary layers are associated with flow mixing and are thus associated with higher levels of skin friction drag. The total local skin friction coefficient expressions for the laminar and turbulent boundary layers are given as follows:

$$C_{f,laminar} = \frac{0.664}{\sqrt{Re_x}} \qquad C_{f,turbulent} \approx \frac{0.059}{Re_x^{1/5}} \tag{2.6}$$

These expressions qualify what was stated in chapter 1 that the skin friction drag associated with a turbulent boundary layer is larger than that associated with a laminar boundary layer at comparable Reynolds numbers.

While the above expressions were given in terms of the local Reynolds numbers , there are a few other definitions of Reynolds numbers which would be commonly referred to in this report. Transition Reynolds number Re_{tr} is defined in terms of the transition location. It is formed from the integration of the boundary layer edge properties from the stagnation point to the transition location x_{tr} [1].

$$Re_{tr} = \int_0^{x_{tr}} \frac{u_e}{\nu_e} ds \tag{2.7}$$

The critical Reynolds number Re_k is used frequently in literature to describe the Reynolds number associated with the critical step height.

$$Re_k = \frac{U_\infty k}{\nu} \tag{2.8}$$

where k is the critical height of the step. The critical step height is defined as the height of the step which would advance the transition to a location forward of the location it would occur at , in the absence of the step [8].

While the above discussion pertains to flat plate flow, the flow over the wing is heavily associated with a pressure gradient. When the flow hits the airfoil at the stagnation point, the velocity drops to zero and the static pressure skyrockets. As the flow climbs over the surface of the airfoil, it experiences a favorable pressure gradient (high pressure to low pressure), causing the flow to accelerate by the Bernoulli equation. This acceleration continues until a pressure minimum, beyond which the flow experiences an adverse pressure gradient (low pressure to high pressure) and the flow decelerates. This deceleration of the flow in the adverse pressure gradient region makes it prone to separation. To simulate a pressure gradient on a flat plate, a ceiling liner with a pressure body is employed in experimental set ups [41],[37]. A pressure body is a curved structure which is made to vary the height of the test section. When the height varies, the hydrostatic pressure acting on the flat plate varies. Thus a pressure gradient is imposed. Once the key concepts of the boundary layer are understood, the next step would be to study the process of transition that is initiated due to disturbances within the boundary layer.

2.2. TRANSITION PREDICTION - STABILITY ANALYSIS

2.2.1. ROUTE TO TURBULENCE

It has been established that for subsonic commercial aircraft, the low skin friction drag associated with laminar flows is desirable. Thus, the understanding of laminar-turbulent transition is key for achieving laminar flow over a considerable portion of the lifting surface. It is understood that the transition depends on various parameters such as Reynolds number, pressure gradient, external disturbances etc.[11]. The route to turbulence is best understood by considering the Morkovin diagram illustrated in Figure 2.2. When environmental disturbances are introduced to a flow, receptivity mechanisms take hold. Receptivity is connected with the means by which the external disturbances such as noise, vibrations, roughness etc. are internalized by the boundary layer. After the disturbances are internalized, two broad types of transition can be distinguished:

- When the amplitude of the disturbance forcing the boundary layer is small, development of regular oscillations is observed. These waves are called primary instabilities and they form the eigenmode growth in the laminar boundary layer. This stage can be described by linear stability theory. The growth of these disturbances is weak occurring over a viscous length scale and can be modulated by pressure gradient,mass flow, temperature gradient etc. [25]. The nonlinear interactions of primary instabilities lead to secondary instabilities, which eventually breakdown to turbulence. This path illustrated in Figure 2.2 is the path of natural transition.
- When the forcing disturbances are not weak such as large isolated roughness elements, three-dimensional disturbances grow dramatically [63]. Nonlinear processes develop and the transition to turbulence ensues almost rapidly via bypass mechanisms, wherein the linear stages of transition process are bypassed. The use of linear stability theory to describe this route to turbulence is therefore not justified. This path illustrated in the Morkovin diagram is the Bypass transition.

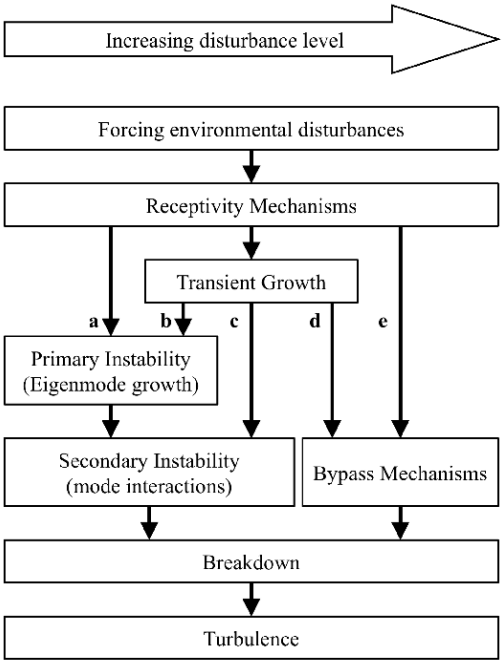

Figure 2.2: The routes to turbulence through natural and bypass transition illustrated by Morkovin Diagram (Reproduced from [52])

Flows over surfaces on subsonic transport aircraft encounter small amplitude disturbances, which could be operational in nature such as insect debris, dirt, engine noise, etc. and due to manufacturing processes such as joints, seams and seals. Thus, the path of natural transition will be referenced in this report. The growth of these small amplitude disturbances can be studied by a popular method called linear stability theory.

2.2.2. LINEAR STABILITY THEORY

Stability analysis is a procedure of great relevance in laminar turbulent transition. Stability theory tracks temporal and/or spatial development of the introduced disturbance in the transition regime. It should be noted that stationary

crossflow vortices are very weak (small amplitude v' disturbances), which motivates the use of analytical models based on linear theory to predict their growth. There are two stability approaches available: local and non local approach. The local approach involves solving the Orr-Sommerfeld equation, while the non-local approach involves solving parabolized stability equations. Since only the local approach was employed in the present study, the same would be covered within this chapter.

THEORETICAL BACKGROUND - LOCAL APPROACH

The basic assumptions behind this theory include:

- Parallel flow assumption : The implication of this assumption indicates that at any station in the xz plane, the stability is independent of all other stations [11]. The streamwise velocity component must not vary in the stream-wise direction else it would simulate non parallel nozzle flow. The pressure only varies in the stream-wise direction.

$$V = 0 \quad U = U(y,t) \quad W = W(y,t) \quad P = P(x,t) \tag{2.9}$$

- 3D incompressible steady basic flow : This implies that the basic flow variables are independent of time.

$$U = U(y,\not{t}) \quad W = W(y,\not{t}) \quad P = P(x,\not{t}) \quad v' = V = 0 \tag{2.10}$$

- The introduced perturbation is a small amplitude disturbance.

The flow to be studied is decomposed into the basic flow and the time varying disturbance.

$$u = U(y) + u'(x,y,z,t) \quad w = W(y) + w'(x,y,z,t) \quad p = P(x) + p'(x,y,z,t) \tag{2.11}$$

These resulting variables replace the velocities and pressure in the 3D, unsteady, incompressible Navier Stokes equations. After applying Prandtl's boundary layer approximation and linearizing the equation, the resulting equation is the disturbance equation and it becomes the starting equation for the derivation of the Perturbation differential equation or the Orr Sommerfeld equation [25]. For the derivation of the Orr Sommerfeld equation, the introduced perturbation is defined as a progressive wave comprising of sinusoidal waves. Thus, an exponential function is used to represent sines and cosines by the Euler's formula :

$$\hat{u}(x,y,z,t) = \phi(y)e^{i(\alpha x+\beta z-\omega t)} \tag{2.12}$$

Where x, y, z is an orthogonal coordinate system and y is taken to be the direction normal to the surface. For the introduced perturbation, the complex amplitude function ϕ represents the amplitude of the vertical perturbation which depends only on y. From the above equation, α is the streamwise wavenumber (growth rate), β is the spanwise wavenumber (growth rate) and ω is the frequency. At this juncture, there can be two descriptions of stability: temporal stability and spatial stability. In temporal stability, the wave amplitude is constant in space but varies in time. The spanwise and streamwise wavenumbers are fixed and thus are real, while the frequency ω is complex. In spatial stability, the wave amplitude grows in space but is constant in time. The frequency ω is fixed and thus real. The spanwise and streamwise wavenumbers are complex [45]. Spatial stability approach is commonly utilized as this is a more realistic description of the disturbance propagation in the boundary layer [11]. This is because when the frequency is fixed, we subscribe to an Eulerian frame of reference, which is akin to seeing the wave grow from an observer's frame outside the wind tunnel. The difference between a temporally and spatially unstable one dimensional wave is shown in Figure 2.3.

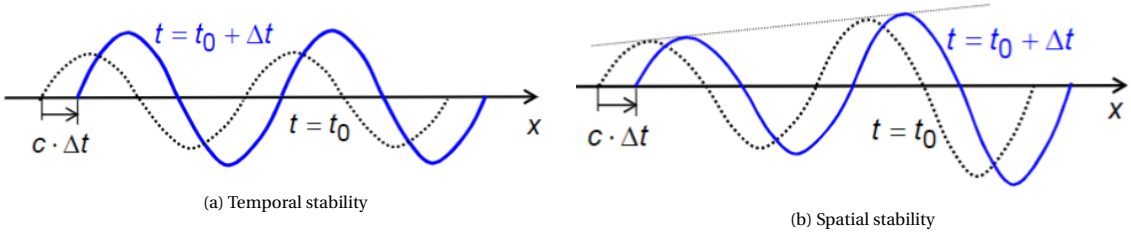

(a) Temporal stability

(b) Spatial stability

Figure 2.3: Temporally and Spatially unstable 1D wave (reproduced from [45])

On substituting the introduced perturbation in the disturbance equation (nonlinear PDE) , the Orr Sommerfeld equation (linear homogeneous fourth order ODE) results. The fourth-order linear differential equation can be represented as an eigenvalue problem, solving for which gives the eigenfunctions (vertical velocity disturbance profiles) and eigenvalues (wave number). For a given basic flow , the following six parameters exist to test stability in the Orr Sommerfeld equation : $\alpha_i, \beta_i, \alpha_r, \beta_r, \omega, Re$.

Given a velocity profile and Reynolds number, assuming a real frequency, the eigenvalue problem is solved for the wave numbers (α and β) and stability is decided based on the sign of the imaginary part of the wave number. For instance, when the spanwise growth rate $\beta_i = 0$ (spanwise invariance/infinite wing assumption), the wave is unstable when $\alpha_i < 0$ in the stream wise direction. The wavenumber vector k is given by $[\alpha_r, \beta_r]$. The angle that the instability takes with the streamwise direction can be calculated from LST :

$$\psi = \arctan\left(\frac{\beta_r}{\alpha_r}\right) \tag{2.13}$$

For different sets of frequencies and Re, a stability diagram is populated with growth rates (wave number vectors).These points represent a parameter space forming the bounds for instability. Figure 2.4a shows a typical spatial stability diagram. The parameter sets (frequency and Re) which lie inside a 'neutral stability curve' correspond to unstable modes and those which lie outside the curve correspond to stable modes. This implies that if a disturbance is excited at a frequency and at a stream wise location lying inside the curve, the disturbance will grow in amplitude. Within the present study, the local approach is used in estimating the stability characteristics of the developed boundary layer.

e^N METHOD

The transition prediction method based on linear stability theory - e^N method developed by van Ingen [36] is considered the most useful practical transition prediction method for many applications. It involves calculation of the amplification factor by integrating the growth rate from the neutral stability point to a location downstream of the body. Given that the stability diagram is available for sufficient number of streamwise stations (x), at a particular station x, the amplification rate of a spatially growing wave can be calculated as follows:

$$\sigma(x) = ln\left(\frac{A}{A_o}\right) = \int_{x_o}^{x} -\alpha_i dx \tag{2.14}$$

where x_o is the location where the disturbance with amplitude A_o first becomes unstable. $\sigma(x)$ represents the amplification factor and $-\alpha_i$ represents the spatial growth rate or amplification rate. A set of amplification rate curves is obtained on calculating the amplification factor for a series of x positions. The envelope of these curves gives the maximum amplification factor or N factor. Thus, the transition is predicted as follows:

$$\left(\frac{A}{A_o}\right)_{trans} \approx e^N \tag{2.15}$$

It must be noted that the N factor calculated is unique to the conditions in which the method is carried out. If any components of the e^N method changes, such as a change in experimental conditions or a change in wind tunnel, the method would need to be re-calibrated.

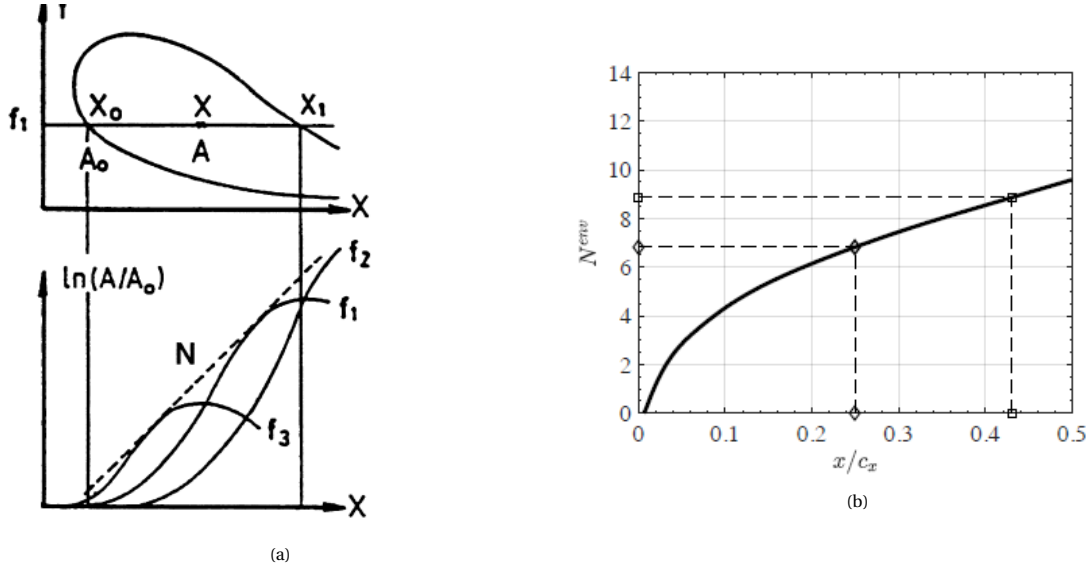

(a) (b)

Figure 2.4: a) Generation of envelope curve from stability diagram (reproduced from [11]) and b) N factor envelope (reproduced from [3])

Figure 2.4a illustrates how the envelope curve is obtained from the stability diagram. Considering a wave propagating downstream from x_o at a fixed frequency f_1, the amplification rate at a particular x location is calculated from Equation 2.14. This process is repeated for every x location to get the characteristic curves. The envelope of all the frequency curves gives the N factor envelope shown in Figure 2.4b.

In the preliminary measurements performed for the present study, the spanwise spacing of the discrete roughness elements (DREs) is decided by N factor envelopes generated for a range of wavelengths. In practice, DREs are used to generate steady disturbances because they allow the introduction of specific and well-controlled disturbance wavelengths [14] . When assuming $\omega = 0$ in linear stability theory formulation, the wavelength corresponding to the maximum N factor is associated with the most amplified stationary CF. Since stationary crossflow vortices are non-moving in time, when $\omega = 0$ by Equation 2.12, the perturbation formulation becomes fixed in time. [3].

In the research works which will be mentioned in the next chapter, the N factor envelope will be generated from the pressure distribution for every experimental condition (Re_x and α) on a clean surface without surface irregularities. The experimentally/computationally observed transition location will thus be used to find the N factor corresponding to laminar-turbulent boundary layer transition in the clean and step cases. The difference between the two is the ΔN factor criterion which will be adressed in the next chapter.

3

STATE OF THE ART

The following chapter serves as a survey of the literature available in the domain of crossflow dominated transition with surface roughness. The following sections concisely present the literature review on the instability mechanisms in swept wing flows. The objective of the chapter is to review the experimental and numerical work in the effect of surface roughness on crossflow dominated transition.

3.1. INSTABILITY MECHANISM IN SWEPT WING BOUNDARY LAYERS

Swept wings are a common design feature in commercial transport aircraft. They are employed for commercial flights to be able to travel at high speeds without encountering wave drag. Wave drag is the component of drag on aerodynamic surfaces which occurs due to the presence of shock waves on the surface. Since the chordwise component of freestream velocity over a swept wing is reduced due to the presence of the sweep, a reduced component of airflow is accelerated over the wing. This implies that the aircraft can fly at higher Mach numbers before encountering wave drag [17]. Owing to the relevance to commercial aerospace, this literature survey will be restricted to application on high subsonic transport aircraft. At this juncture, it is important to highlight that the transition on swept wings occurs due to four primary instability mechanisms: Crossflow, Tollmien-Schlichting, Görtler and attachment line contamination (ALC).

3.1.1. TOLLMIEN-SCHLICHTING INSTABILITY

In two-dimensional flows, transition begins with the amplification of wave like disturbances called Tollmein-Schlichting (TS) waves first identified by Schubauer and Skramstad [74]. These TS waves first exhibit an exponential growth which can be calculated by linear stability theory (LST). Downstream, however, these waves gain amplitude and their development begins to deviate from LST. These two dimensional TS waves are found to break down into a series of peaks and valleys [57]. Further downstream of the break down, nonlinear characters begin to emerge where these peak valley structures are stretched into horseshoe vortices breaking down to form smaller vortices. These fluctuations eventually become random and turn into a turbulent spot. The streamwise location where the spots first occur is taken to be the onset of transition. Arnal and Casalis [11] indicate that the linear amplification process occurs for about 75-80% of the distance between the leading edge to onset of transition justifying the usage of LST for transition prediction. Tollmien-Schlichting instability is seen in the mid-chord region of swept wing flows and is destabilized by an adverse pressure gradient [71].

3.1.2. GÖRTLER INSTABILITY

One of the many mechanisms that can destabilize the boundary layer is in the form of steady, streamwise-oriented, counter-rotating vortices called Görtler vortices. In the boundary layer over curved walls, the forces which are at play are centrifugal forces and pressure gradient. These centrifugal forces reduce in amplitude as we move closer to the wall due to the effect of viscosity on the momentum. For a boundary layer over a curved surface, as seen in Figure 3.1 (bottom left), at the center of curvature $rU_\infty = 0$ and at the wall $r_w U = 0$, where r is the radius of curvature. At the location where the local velocity equals the free stream $U = U_\infty$, rU_∞ increases with r. Thus, as maximum rU exists, this brings into effect a region where $d|rU|/dr < 0$. Floryan [43] noted that the stability of the flow depends on the monotonic behaviour of the velocity profiles. The following figure illustrates the left velocity profile which leads to centrifugal instability on a concave surface due to the non-monotonic nature of the profile. The profile on the

bottom right is it's stable counterpart. On convex surfaces, however, the opposite scenario unfolds. Since there is no slip at the wall, the velocity is zero there and the velocity increases as we move away from the radius of curvature.

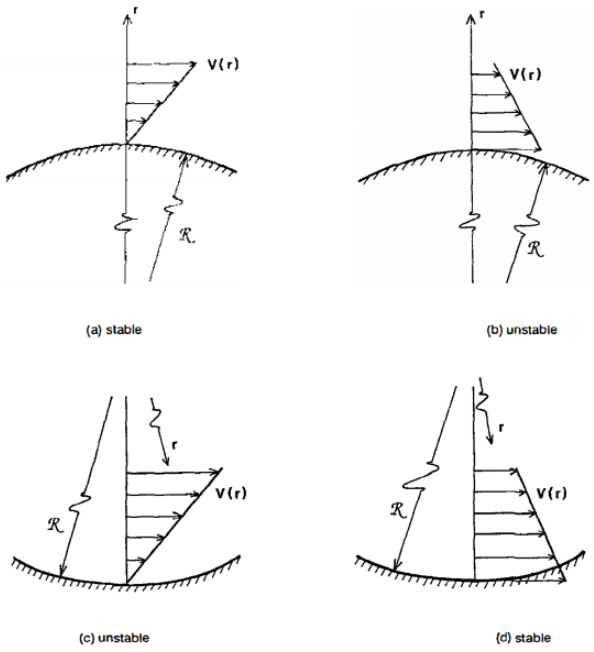

Figure 3.1: Stable and unstable velocity profiles over curved surfaces (reproduced from [70])

Since the Görtler vortices have been established to be a geometry-induced phenomenon, the curvature of the leading edge of a swept wing is connected to the stabilization of the flow which is susceptible to this instability. From the above illustrative theoretical understanding of the development of this instability, many works that followed observed that a convex leading edge stabilizes the instability, whereas a concave leading edge destabilizes it.

3.1.3. ATTACHMENT LINE CONTAMINATION INSTABILITY

Gray [69], in certain flight experiments noticed transition occurring close to the leading edge in swept wings. This transition mechanism was triggered by a critical speed and depended on leading edge sweep angle as well as radius. Naphthalene sublimation photographs of the transition region showed fine striation patterns. Extending upon this, experimental studies conducted by Northrop Corporation [67] observed turbulent bursts at the front attachment line of a 45^o swept wing causing early transition. It was hypothesized that amplified high frequency attachment line boundary layer oscillations induced by wind tunnel screen turbulence in combination with random low frequency oscillations (induced potentially by free stream eddies), could be the reason for the observed turbulent spots.

In order to avoid wing-root disturbances to trip the boundary layer and kick off this instability mechanism, it was reported by Saric [72], that the momentum thickness Reynolds number (Re_θ) at the attachment line should be kept below 100. This could be achieved by Pfenninger's [66] relation :

$$Re_\theta = 0.404\sqrt{\left(\frac{U_\infty r \sin^2\Lambda}{(1+\epsilon)\nu\cos\Lambda}\right)}$$

where r is the radius of the nose, Λ is the leading edge sweep angle, ν is the kinematic viscosity and ϵ is the ellipticity of an equivalent ellipse. Practical applications in commercial transport aircraft require that reduction in the leading edge radius and sweep angle is a good thumb rule for the suppression of transition due to attachment line contamination instability.

3.1.4. CROSS-FLOW INSTABILITY

Since modifications to the shape of the airfoil and the pressure gradient are known to keep the previously discussed instabilities at bay, the study of crossflow instability is critical to the present research work. Observations in flight tests indicated that turbulence occurred much closer to the leading edge on a swept wing than on an unswept wing

([69]) . These observations gave rise to experimental and theoretical studies on rotating disk flow, where inflectional instability due to crossflow was identified as the causative agent for destabilization of the swept wing boundary layer. It was subsequently established that crossflow instability appears in swept surfaces with pressure gradient or on rotating disks.

ORIGIN OF CROSSFLOW

Flow over a swept wing is three-dimensional, in that it involves three components of velocity : the chordwise/streamwise component , the spanwise component , and the wall normal component. The spanwise component of velocity w which arises as a result of the sweep, is assumed to be a constant along the span, assuming an infinite wing.

With an orthogonal coordinate system xyz aligned with the swept wing, an inviscid streamline outside the boundary layer is governed by spanwise and the streamwise components of velocity. When the undisturbed freestream velocity U_∞ meets the stagnation point, the streamwise component u goes to zero while the spanwise component w is a finite constant. As a result, the streamline curves in the direction of sweep, dominated by the spanwise component w. As one proceeds downstream, the flow accelerates from the favorable pressure gradient, so the streamwise component of velocity increases as w remains constant. This path continues until a pressure minimum is reached and the flow then begins to decelerate. Then, u decreases and W dominates the trajectory.

Within the boundary layer, there exists a play between pressure and centrifugal forces. To understand this, consider a particle on the inviscid streamline B in Figure 3.2. A normal drawn at that point, indicates the direction in which the pressure gradient would act. A point on the normal to the left on streamline A, experiences a higher pressure than a point on the normal to the right on streamline C. Thus the pressure gradient acts towards the right. The centrifugal or inertial force acts to the left to keep the forces on the particle on the inviscid streamline at equilibrium. The pressure gradient is constant in the wall normal direction. However, if this particle were moved within the boundary layer, the inertial force keeping the balance decreases, due to the reduction in velocity which persists from viscous effects. The particle is thus projected in a direction normal to the inviscid streamline. This forms the crossflow velocity profile. As the distance close to the wall decreases, the inertial force decreases further and the crossflow velocity increases. This profile shows an inflection close to the wall when the shear dominates to ensure no slip at the wall [65].

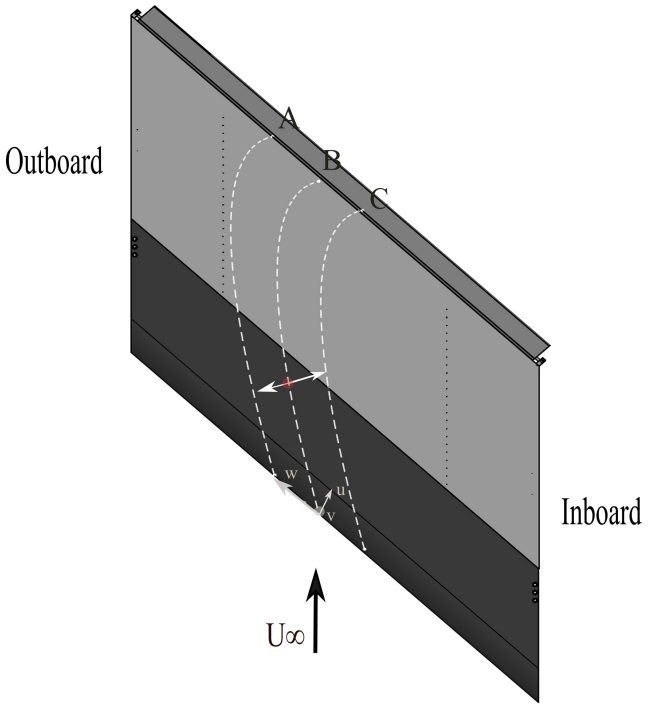

Figure 3.2: Schematic illustrating the crossflow development over a swept flat plate model. Dashed lines indicate inviscid streamlines.

As a result, in three-dimensional boundary layers, such as in the case of a laminar boundary layer developing on a swept wing , the mean velocity profile decomposes into the streamwise component (parallel to streamline) and the

crossflow component (normal to streamline). The resultant of the two (Figure 3.3) leads to the inflectional profile. When the Orr-Sommerfeld equation is solved at the inviscid limit ($Re \rightarrow \infty$) , an important result states that in order for an instability to exist there must be an inflection in the velocity profile. So, any perturbation in the form of a wave that exists due to surface roughness or other external factors develops crossflow vortices due to the inflection point in the crossflow velocity profile.

The direction of rotation of the crossflow vortices is determined by the orientation of the crossflow velocity component inside the boundary layer since this defines the vorticity direction at the point of inflection [41]. Very near the leading edge, where the inviscid streamline inclination with the chordwise direction is the largest, these crossflow vortices appear rotating in the anticlockwise direction (in the given case - since within the boundary layer the crossflow component is directed to the inboard side/root and outside the boundary layer the spanwise velocity component is directed to the outboard side/tip) as illustrated in Figure 3.2.

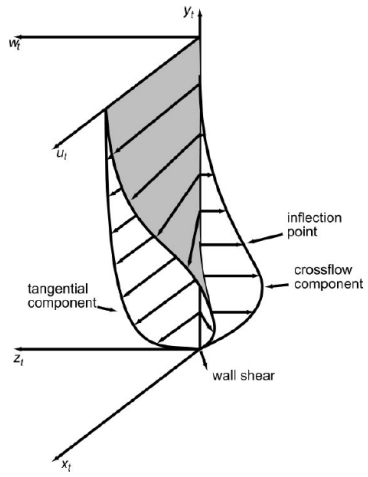

Figure 3.3: Boundary layer velocity profile in swept wing presents the crossflow and tangential components to form the shaded resultant inflectional velocity profile (reproduced from [73])

Thus, a favorable pressure gradient plays a destabilizing role giving rise to cross flow instability. This contrasts with 2D boundary layer flows where an adverse pressure gradient destabilizes the flow causing Tollmien-Schlichting waves.

The question arose regarding whether the flow over a swept wing would be subject to an absolute instability or a convective one. To answer this question, streamwise vortices were stimulated using a spanwise array of heating elements spaced at the wavelength of the most amplified stationary vortices. It was found that on switching off the heating elements, at low velocities, the flow was restored to the state as before the heating was switched on. This proved that the instability was convective [56]. Evidence that the crossflow instability was convective in nature motivated the study of its spatial, and not temporal growth in linear stability analysis.

PRIMARY AND SECONDARY INSTABILITIES

The crossflow instability mechanism in natural transition (as mentioned in subsection 2.2.1) proceeds with first the appearance of primary CF vortices which undergo nonlinear mechanisms and result in secondary instabilities [41]. Primary crossflow vortices modify the base flow as they grow. The first stage is the receptivity process. Since primary stationary CF vortices are rotating structures, they move higher momentum flow from the higher regions of boundary layer and displace it to the lower momentum flow (downwelling/downdraft) and vice versa (upwelling/updraft). These primary vortices grow by redistributing momentum, much like the growth observed in Kelvin Helmholtz instability. The redistribution of momentum gives rise to high pressure and low pressure regions associated with the slower moving updraft and the faster moving downdraft, respectively. The pressure difference causes the growth of the stationary crossflow vortices. This growth of crossflow vortices continues until a "saturation amplitude" is reached which occurs due to the dominance of wall shear [34]. The low momentum fluid above the high momentum fluid produces an inflection point in the velocity profile normal to the wall. This inflectional profile is eventually destabilized by high frequency secondary instability.

Malik et al [50] first reported the classification of the secondary instability into three modes that occur at different frequency bands and at different locations within the boundary layer. The first two are Kelvin Helmholtz modes due

to the shearing of the CF vortices: first being the high frequency type-I mode, coincides with the region where there is local minimum of the spanwise gradient $\frac{\partial U}{\partial Z}$ (z mode) found on the outer side of the upwelling (updraft) region of the primary crossflow vortex. The second high frequency mode is the type-II mode, or y-mode, found on the top of the primary crossflow vortices in regions where there are high levels of wall normal gradient $\frac{\partial U}{\partial Y}$. A third region of fluctuations on the inner side of the updraft near the wall is associated with the local maxima of the spanwise gradient. The disturbances are related to the interaction between the stationary and travelling primary CF modes and were characterised as a low frequency type- III mode [56].

STATIONARY AND TRAVELLING MODES

Based on the nature of the external forcing, the transition due to crossflow instability is dominated by either stationary waves (zero frequency) with constant spanwise wavelength in low turbulence environments or travelling waves (along the spanwise direction) in high turbulence environments [53],[24]. The effect of low free stream turbulence intensity ($Tu < 0.07\%$ which is representative of a flight environment) on the development of cross flow disturbances was studied by Downs and White [59]. They performed wind tunnel experiments varying the turbulence intensity in the wind tunnel between 0.02-0.2% of the freestream velocity. Their hot-wire measurements confirmed that surface roughness forces the primary stationary crossflow instability, while the free stream turbulence and surface roughness forces the primary travelling modes. Moreover, Bippes [23] reported that stationary vortices are excited by a spanwise array of heating or roughness elements, while travelling waves are excited by a spanwise array of oscillators. It should be noted that although the initial conditions cause a dominance of either stationary/travelling crossflow waves, both modes persist in the flow.

Deyhle and Bippes [24] in their work on the identification of initiators of cross-flow waves had found that of the various perturbations and non-uniformity which come under the broad umbrella of environmental disturbances, the major players were three-dimensional surface roughness and free stream turbulence. It was noted that the receptivity of a three dimensional swept flat plate boundary to sound and two dimensional surface roughness was weak. The effect of surface roughness on cross flow waves was established experimentally by Muller and Bippes [9]. Their hot-wire anemometry measurements of the stationary disturbance pattern showed that the pattern remained fixed with respect to the plate as the test article was moved in the spanwise direction. Later, flow visualization studies showed a characteristic sawtooth transition front as seen in the oil flow visualization Figure 3.4. These turbulent wedges were also previously observed in the computational results of Wassermann and Kloker [56]. White and Saric [15] in their experimental study at the ASU wind tunnel on a 45° swept wing model, detail the origin of the turbulent wedges observed. The authors observe from the mean flow velocity contours at a particular streamwise location that there is high shear associated with the left side of the upwelling region of the stationary vortices and the upwelling region has a wider and flatter apex rather than a narrow one seen in upstream locations. The velocity fluctuation rms contours confirmed that the turbulent fluctuations promoting the mixing of high momentum (downwelling) and low momentum (upwelling) fluid, was the reason for the high shear seen in the mean velocity contours. The authors note that mode-I secondary instability sets off the sawtooth pattern. The upstream tips of the pattern is associated with the points (in the spanwise location) where the instability is closest to the wall on the left side of the upwelling region. This cascading breakdown of secondary crossflow vortices from these tips creates the repeating wedge pattern.

White's [13] analysis on the effect of surface roughness and freestream turbulence showed that a saw tooth transition pattern associated with stationary vortices was observed at a turbulence intensity of Tu=0.003, and when a spanwise roughness array (λ_k = 8 mm with k=50 μ m and 2 mm diameter roughness elements) was activated, this saw tooth transition front was replaced by a smooth spanwise invariant transition front associated with travelling waves. This implied that travelling waves resulted from velocity fluctuations interacting with surface roughness and turbulence intensity. Further, although surface roughness forces stationary vortices, increasing roughness amplitude did not make stationary waves more likely than travelling wave. An important inference was thus made: the turbulence intensity and surface roughness together have a role to play on which modes of crossflow instability are triggered. Furthermore, natural surface roughness was also identified to be a source of crossflow waves. A painted model (9 μ m r.m.s) was found to exhibit transition around 30% of the chord length earlier than an a model with a polished surface (0.25 μ m r.m.s) [58].

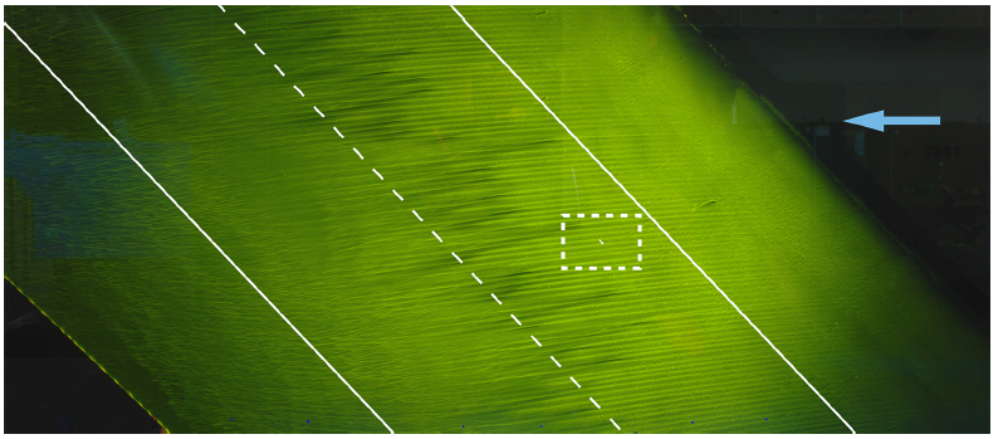

Figure 3.4: Sawtooth transition front observed in fluorescent oil flow visualization. Flow comes from the right (indicated by blue arrow). $Re = 2.12 \times 10^6, \alpha = 3^o$. White dashed line indicates the wing mid section x/c = 0.50. Left solid white line indicates x/c=0.75 and right solid white line indicates x/c = 0.25. (reproduced from [33])

CONTROL BY DREs

DREs have been used to condition the modes to achieve distinct and coherent CF instability evenly spaced at the forcing wavelength in a wind tunnel environment. These micron sized roughness elements are placed near the leading edge to ensure spanwise uniformity of the stationary vortex amplitudes and transition location. In experimental studies by Saeed et al. [64] on a 40^o swept wing model, spanwise uniform discrete roughness elements (DREs) of varying heights were placed at different chordwise locations to excite primary stationary crossflow vortices. Naphthalene flow visualization was employed to locate transition in the cases studied. The principle behind this flow visualization technique is the property that naphthalene sublimates at room temperature and the rate of sublimation depends on the skin friction. Since turbulent flow is associated with higher skin friction, this leaves a distinction between the laminar and turbulent zones, to identify the transition location. The transition front showed the characteristic saw tooth pattern detailed above which indicated that the transition was dominated by stationary CF vortices. Stationary disturbance amplitude plots showed no influence of the strip until a critical height of 330 μm. Larger strip heights were associated with high frequency unsteadiness in the flow . For the strip placed near the leading edge, there was a considerable increase in the initial disturbance amplitude. When the strip was moved downstream, the flow was more prone to high frequency unsteadiness.

Zoppini et al.[20] study the effect of DRE location and amplitude on the transition location. In this receptivity study, they use four DRE heights and DRE locations before and after the neutral point. The authors observed through infrared thermography (IR) measurements, an advancement in the transition location when DRE height increased. This was attributed to the higher initial amplitude introduced by a taller DRE element array. A downstream movement of transition location was reported when the DRE array was shifted to a downstream chordwise station, which is linked to the late growth of CF vortices. The crossflow velocity profile was obtained from PIV data at multiple chordwise locations and the higher amplitude instabilities triggered an increase in the maximum of the velocity profile which continued to increase until saturation. The monotonic trends of transition location shift with DRE amplitude and location was not recorded to be linear.

3.2. EFFECT OF EXCRESCENCES ON CROSSFLOW INSTABILITY

Aerodynamic surfaces are prone to non-uniformity which could arise as a result of operational environments such as insect contamination, atmospheric ice crystals, debris and engine noise. They could also arise due to manufacturing processes such as joints, seals, and seams. A persistent problem that is actively being researched upon is the effect of steps on transition in a swept wing flow. Two dimensional (spanwise invariant) steps are common surface features which are of practical interest found in subsonic transport aircraft. Since the skin of the aircraft is formed from multiple aircraft panels integrated together by lap-splice or a single strap joint (Figure 3.5), this arrangement gives rise to forward and backward facing steps and gaps respectively [3]. Since the effect of surface imperfections on transition in swept wing flows has been identified [8], many studies have been devoted to the effect forward and backward facing steps have on boundary layer transition.

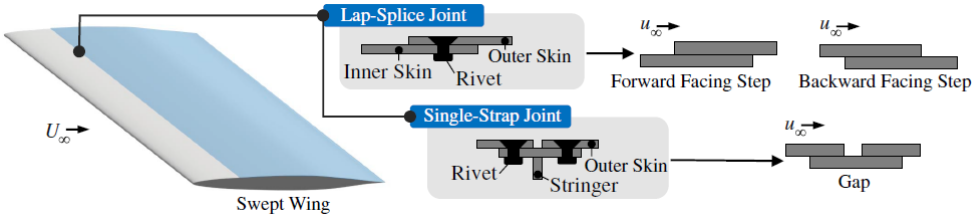

Figure 3.5: Formation of forward and backward facing steps and gaps on a swept wing (reproduced from [5])

As discussed in chapter 2 , laminar flow is associated with lower skin friction drag than turbulent flow. For the purpose of increasing fuel efficiency, it becomes important thus to maintain laminar flow over a larger portion of the wing. Subsequently, in order to design aircraft components for laminar flow, it is important to specify manufacturing tolerances for the size and shape of the excrescence. This can only follow the fundamental study of effects of surface excrescences on laminar boundary layer stability.

Manufacturing requirements for a global criterion to determine the critical step height or gap width which would advance transition has driven research efforts over the past two decades centered around transition driven by the most relevant instability dominant in the swept wing: CF instability and its interaction with FFS and BFS. A summary of the relevant research which study the effect of steps on crossflow transition, is presented in the coming sections.

3.2.1. FLOW TOPOLOGY IN PRESENCE OF STEP

SWIFTER experiments carried out at Klebanoff-Saric wind tunnel by Duncan et al. [21], were used to study the crossflow instability interaction with a forward facing step on a 30^o swept wing model. The authors observed two separated regions, one near the step was speculated to be the result of a shear layer instability and the other due to the crossflow instability. A spanwise non-uniformity in transition front was observed, which was hypothesized to be due to the travelling crossflow coupled with the freestream frequency non-uniformity persistent in the wind tunnel.

Tufts et al. [48] performed a computational study to highlight the interaction at play between two dimensional excrescences and cross-flow instability in a swept wing. The authors extend the test conditions of the SWIFTER [21] and SWIFTEST experiments to the computational domain. It was observed that the forward facing step was associated with 2 regions of recirculating flow (Figure 3.6): one in front of the step and one on top of it. These re-circulating helical flow regions had a mean velocity directed from the root to the tip , and these regions were reported to be open and not closed. While there was a favorable pressure gradient on the majority of the wing, the authors report a local adverse pressure gradient near the step followed by a small favorable pressure gradient and then another adverse pressure gradient region. The size of both of the helical flow re-circulation regions was reported to increase as the step size increased. Front re-circulation region was found to be as high as a quarter the step height for small forward facing steps and half the step height for larger forward facing steps. The top re-circulation region also scaled with step height but was observed to have a higher aspect ratio than the lower re-circulation region.

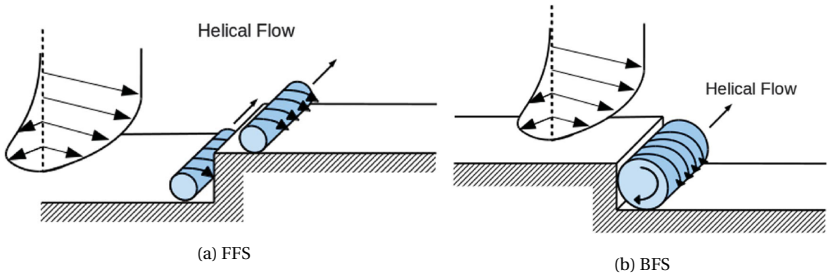

(a) FFS (b) BFS

Figure 3.6: Recirculation regions associated with forward and backward facing steps (reproduced from [48])

While the existence of the second flow reversal region on the step was contested by Cooke et al. [16], a recent DNS study carried out by Casacuberta et al. [29] observed the presence of second separation bubble, however only for larger step heights. The authors note that the presence of a separation bubble is induced by the geometry of the step while the crossflow reversal observed is induced by the adverse pressure gradient brought on by the presence of the step.

Rius-Vidales et al. [4] studied the impact of a forward facing step on crossflow instability with Infrared thermography measurements on an in-house built swept wing model. IR works on the principle that the turbulent boundary

layer is associated with a higher wall shear stress than the laminar boundary layer. This increased wall shear causes an increase in heat transfer. So when actively heated, the final wall temperature is lower in a turbulent boundary layer than its laminar counterpart. Infrared thermography measures this temperature gradient to identify the location of transition. Their studies confirm the pressure gradient signature (favorable at step, followed by adverse then favorable downstream) seen by Tufts, from the observed outboard-inboard-outboard tilting of their crossflow trajectories.

As the CF vortices approach the step, an outboard tilting of the trajectory results in a spanwise velocity increase. A component of this spanwise velocity is converted to vertical velocity at the step due to the upward deflection of the flow. Using $Z-Y$ plane contours of time averaged vertical velocity, the v component was found to reach its maximum on the inner side of the upwelling region of the CF vortex. Downstream of the step, the authors report a second amplification of the spanwise disturbance profile and an inboard tilt (due to favorable pressure gradient) of the crossflow vortices. This second amplification triggers an increase in mean flow distortion leading to saturation of primary CF vortices. As a result, further downstream, the authors observe CF decay and the vortices undergo another outboard tilting (due to adverse pressure gradient).

RAMPED STEPS

It was proposed by Tufts to study the effect of ramped FFS on CF dominated transition (drawing upon the work by Holmes [8] for TS dominated transition), since it would aid in delaying transition when compared to the unramped FFS. Eppink and Casper [41] research the effect of ramped FFS on delaying transition using stereoscopic PIV measurements at and downstream of the step. Stereoscopic PIV involves the placing of two cameras to collect all three velocity components in a two dimensional domain (planar laser sheet). The model used was a 30° swept flat plate and the measurements were performed at a single freestream velocity of 26.5 m/s . In order to force the stationary crossflow vortices, discrete roughness elements were placed at a spanwise wavelength of $\lambda_z = 11mm$ corresponding to the most amplified stationary wavelength calculated from LST for the case without step.

A forward facing step of height in the supercritical regime (from Eppink [41]), 1.95 mm (square, 30° and 45° ramp) was used for the purpose of the study. The measurements were performed perpendicular to the step at span-wise intervals of 1 mm, using a profileometer fitted with an optical distance sensor mounted on a linear traversing platform allowing for measurements of the 2D step. Contours of span-wise averaged velocity profiles downstream of the step indicated the expected result that, as the ramp angle decreases, the step delays transition compared to the unramped cases.

3.2.2. EFFECT OF STEPS ON MEAN FLOW

TUFTS-REED HYPOTHESIS

Tufts et al. [48] introduce a parameter called the vortex core height which they claimed correlated with the step height. This height took into account the upstream development of the boundary layer as well as the stability behaviour. For subcritical steps, when the step height was lower than the core height of the incoming crossflow vortex, the crossflow and helical flow interaction was reported to be destructive on top of the step . Helical flow and the lower half of the crossflow vortices oppose each other in direction. This is illustrated in Figure 3.7 (left).

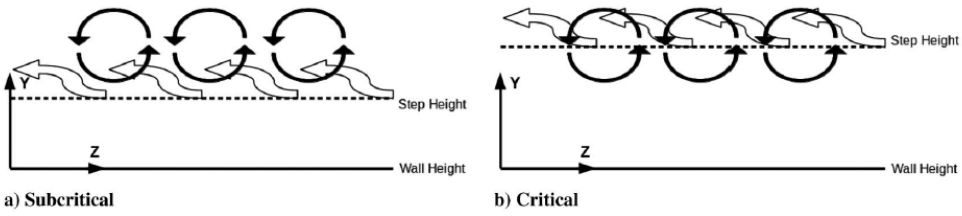

Figure 3.7: Helical and crossflow vortices in the presence of an FFS/BFS. (reproduced from [48])

This destructive interaction was claimed to be the reason stationary CF vortices did not grow for subcritical step heights. On the other hand when the step height is higher than the vortex core height, the interaction between helical and crossflow was found to be constructive as the z component of velocity moved in the same direction and as a result, the transition front displaces towards the step . This is illustrated in Figure 3.7 (right). They suggest that the constructive interaction between the incoming stationary crossflow vortices and helical flow forms the mechanism for increased growth of the stationary crossflow mode beyond a critical step height. If the core height of the vortex can be predicted, then the authors indicate that this value would be close to the critical step height (as this is the

height at which constructive interaction would occur). For the wavelength corresponding to the maximum amplification of the crossflow vortices (highest N factor) by LST, the vortex core height was taken to be the wall normal distance corresponding to the approximately (97% of maximum) maximum amplitude of the V perturbation profile.

Additionally, the authors suggest that the manufacturing tolerances for FFS would be less conservative compared to that for BFS and that decreasing the size of the upper re-circulation region (which could be achieved by ramping or rounding the FFS edge as suggested by an early study by Holmes [8] for TS waves) may diminish the effect of the forward facing step. As it has been established that forward facing steps have a less severe negative effect on swept and unswept boundary layer transition (i.e. irrespective of whether the dominant instability mechanism is crossflow or TS) than their backward facing counterparts, more research efforts were focused on defining tolerances for FFS.

Extending the Tufts Reed criterion to the experimental domain, Rius-Vidales et al. [3] studied the effect of 2D forward facing step on a 45^o swept wing.

The authors performed a linear stability analysis to obtain the change in N factor due to the excrescence. The vortex core height was calculated for the maximum amplification wavelength by the procedure stated in Tufts et al [48]. For a vortex core height ratio $y_c/h >> 1$, i.e. when the vortex core height far exceeded the height of the step, only a small reduction in critical N factor was observed. However, when the vortex core height was much smaller than the step height, there was a greater critical N factor reduction indicating a stronger effect on transition. Furthermore, increased relative step height h/δ^* was associated with a greater critical N factor reduction for a fixed vortex core height ratio y_c/h. The authors thus highlight that the two parameters cannot be considered independently of one another in analysing the effect of FFS on swept wing transition.

CONTRADICTIONS TO TUFTS REED HYPOTHESIS

In order to, characterize the mechanism for the increased stationary crossflow amplitude near the forward facing step, and the eventual growth and breakdown downstream of the step, detailed experimental investigations on a 30^o swept flat plate were performed at the Low speed boundary layer channel at NASA Langley research center by Eppink [40]. The author employs naphthalene as a sublimating surface coating for identification of the transition location. The flow was studied for five step heights from 1.27 mm to 1.7 mm, which corresponded to 53% – 71% of the local (at the step location) undisturbed boundary layer thickness δ_{99}. For all the step heights, the initial stationary cross flow amplitude was decided by placing a single layer of DREs near the leading edge. An added test case (k = 1.4 mm) studied flow at an increased initial stationary crossflow amplitude by placing four layers of DREs. The critical step height for the single layer of DREs through naphthalene flow visualization was identified to be 1.6 mm. Interestingly, an advancement in the transition location for the step height case corresponding to an increased initial stationary crossflow amplitude showed that the initial stationary CF amplitude played a governing role.

Spanwise averaged crossflow velocity contours illustrated an outboard to inboard crossflow rotation upstream of the step following which the crossflow reversal occurs. This was explained with the computational observations of Tufts et al. [48], detailing an adverse pressure gradient before the step, a favorable pressure gradient on top of it, and then again an adverse pressure gradient after it. Boundary layer velocity profiles of the streamwise velocity, showed about a 50% decrease in boundary layer thickness δ_{99}. A thinner boundary layer could amplify even smaller wavelength disturbances greatly, which confirmed the effect mentioned in the work of Tufts et al [48].

However, the stationary crossflow U perturbation profiles calculated at locations upstream of the step lift up off the surface, indicating that the center of the crossflow vortex does not correspond to the critical step height as was proposed by Tufts et al. [48]. Thus the author refutes the claim that the vortex core height plays a governing role in the interaction.

Furthermore, the contours of U-disturbance velocity, showed that the separation bubble found on top of the step were purely a result of the inflectional CF profiles. The author disagrees with the claim by Tufts et al. [48], that a constructive interaction between the helical flow and incoming CF vortices beyond a critical step height, causes stationary crossflow growth. The author theorizes that the observed gradual increase in the initial growth rate of stationary CF vortices (primary instability) with increasing step height supports the idea that the strength and size of the separation bubble increases as the step height increases, and thus increasing the impact on the incoming stationary CF vortices. Eppink emphasizes that the transition does not occur due to a sudden critical behaviour defined by the vortex core height as suggested by Tufts et al. [48].

Another contradiction to the Tufts-Reed hypothesis, was reported in Rius-Vidales et al. [5]. The measurements were performed at the LTT facility in Delft University of Technology on a swept wing model. In the study, the authors identified three modes of forcing the stationary crossflow were identified : early growth mode ($\lambda_z = 4.5mm$), midgrowth mode ($\lambda_z = 5.5mm$) and late growth mode ($\lambda_z = 7.5mm$). The early growth mode corresponds to the wavelength smaller than the one most amplified at the step location. Mid growth mode corresponds to the wavelength associated with most amplifed crossflow at step location. Late growth mode corresponds to the wavelength

larger than the one most amplified at the step location. For the mid-growth mode , the short FFS showed a minor change in transition location, however, as the step height increased, the transition location moved towards the forward facing step. The authors observed that the unforced case, exhibited subcritical behaviour for all FFS (Δx_t around unity) even when there was a decrease in vortex core height ratio and increase in step height ratio. These trends led to the inference that the vortex core height was not directly correlated to the critical step height unlike what was stated by Tufts et al. [48].

3.2.3. FLOW STRUCTURES DOWNSTREAM OF STEP

The work of Eppink and Casper [41] on ramped forward facing steps provided a description of the flow field dominated by stationary crossflow before and after the forward facing step. Using spanwise averaged perturbation velocity profiles (steady disturbance profiles) the authors showed that the initial growth of U'_{rms} was due to crossflow reversal and separated flow from the strong inflection points. The authors identified two locations of importance downstream of the step:

- Near step region : Inflectional profiles are important features in destabilizing the flow. High frequency fluctuations measured were hypothesized to trigger unsteady disturbances which amplified downstream. The authors proposed that the first region of growth was attributed to the strong inflectional profiles (which destabilize the mean flow) caused by the adverse pressure gradient near the step.

- Flow recovery region : Downstream of the separated profiles, after the stationary crossflow vortices grew and decayed, there was found to be a second region of growth. The authors found that of the many stationary crossflow modes present downstream of the step, some grow and decay in the near step region and others grow consistently from the step or from the separated region. On varying the initial stationary crossflow modes, the paper reported varied growth rates of the disturbances downstream of the same step. Thus, strong growth in the flow recovery region (second growth region) was deduced to be attributed to nonlinear effects due to the modulation of the recirculation region downstream of the FFS edge, resulting in the streamwise oriented vortices (discussed below) amplifying the harmonics of the primary mode. A similar amplification-decay-amplification pattern was observed in the peak amplitudes of spanwise velocity perturbation in Rius-Vidales et al. [4].

Eppink [41] describes the nonlinear mechanism associated with the second region of growth (secondary instability) of the stationary CF vortices observed downstream of the largest step height case (supercritical step height k= 1.7 mm). Immediately downstream of the step exist the recirculation region with positive spanwise vorticity ($\omega_z = \partial U/\partial y - \partial V/\partial x_c$) which are then bent into a U shape due to the due to the negative spanwise gradient in U velocity on the left of the separation bubble and positive spanwise gradient of U on the right of the separation bubble. Downstream of the reattachment of the separation bubble, exist stream-wise oriented vortices. This vortex shedding mechanism corroborated the pressure gradient signature described by Tufts et al. [48].

Extending on her own work, a detailed study of unsteady instabilities arising from forward facing steps on a 30° swept flat plate was performed [37]. In order to purely capture secondary instabilities, time-resolved PIV measurements were made with the cameras positioned downstream of the forward facing step. PIV works by releasing tracer particles which are carried by the flow, passing through a designated measurement region which is illuminated by a laser sheet to capture the images by strategically positioned high-speed cameras. Cross correlation techniques are employed on the imaged flow to obtain the flow velocities. When the step interacts with the stationary crossflow, strong crossflow vortices appear near the step, leading to a spanwise distortion of the separation bubble (helical flow region) downstream of the step. It was understood that the onset of separation and crossflow reversal are due to the presence of an adverse pressure gradient downstream of the step. The crossflow reversal destabilizes the stationary crossflow vortices rotating in a direction opposite to that of the initial primary crossflow vortices [41]. It was found that as the height of the step increased, the impact of stationary crossflow increased, which resulted in a more severe modulated flow in the separated regions. What follows thus are isolated zones of recirculating flow spaced with the wavelength of the primary stationary crossflow. Thus, it was deduced that the shear layer and reattachment of flow are responsible for the origin of the unsteady fluctuations. This separation region sets off a series of events which leads to the growth and development of secondary instabilities in the flow.

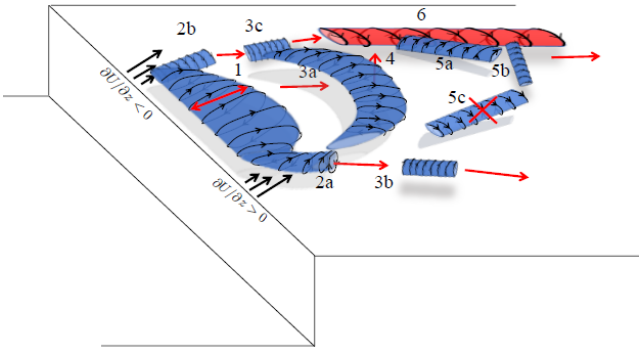

Figure 3.8: Proposed vortex shedding mechanism downstream of forward facing step (reproduced from [37])

From Figure 3.8, the route to turbulence downstream of the step as understood by Eppink [37] is summarized as follows:

- Incoming stationary crossflow vortices modulate the separated flow region (1) which faces unsteady disturbances due to either shear layer instability, high frequency secondary instability, unsteadiness in the shear layer, or all combined.
- The outboard (right) side of the separation bubble shows a positive spanwise gradient of streamwise velocity resulting in shear layer roll up (2a). This creates a structure similar to a tail rotating in the anticlockwise direction when viewed upstream.
- Due to the perturbation effect on the shear layer, there exists a phase where an adverse upstream and favorable downstream pressure gradient persists causing the separation bubble to be pulled apart and vortex shedding to occur (3a, 3c).
- The biggest and strongest of these vortices, which is initially distorted due to the distortion of the separation bubble further becomes distorted due to the positive wall normal velocity (V) which is the strongest near the center of the vortex. This velocity lifts the middle of the vortex and pushes it into regions of high streamwise U velocity. The resulting vortex is that of a hairpin vortex with counter rotating arms. Since the local mean flow only supports counterclockwise rotation , only one of the arms continues downstream (5a) .
- Here, the streamwise velocity gradient is positive, increasing the strength of the vortex through vortex stretching. The other arm becomes a weaker spanwise oriented vortex moving downstream (5b) which gives rise to the u' (streamwise) fluctuations measured in the region.
- The vortex shed from the right tail of the separation bubble (3b) rotates counterclockwise but appears weaker than the other streamwise oriented vortex (5a) , speculated to be due to the lack of vortex stretching. The fluctuations generated by this vortex merge and could interact with the fluctuations convecting downstream from the next separation bubble.
- Similarly, the mechanism repeats on the left side of the separation bubble (2b). Here the spanwise velocity gradient is opposite in direction, causing a clockwise rotating shear layer roll up. Consequently, a clockwise rotating vortex is shed downstream , passing through a region with a strong stationary crossflow vortex (6), and possibly interacts with it.

Casacuberta et al. [29], in their DNS study, arrive at the inconclusive result that either there exist two distinct secondary crossflow vortices upstream and downstream of the step (as proposed by Eppink [41]) or a single structure persists and undergoes distortion at the step corner. In Eppink's work, the author suggests that the secondary vortices induced upstream of the step create a perturbation in the wall normal direction which is sustained and in combination with strong crossflow reversal at the step creates a new secondary near wall vortex. While Eppink [41], suggests that the step-induced inflection points are responsible for perturbation growth downstream of the step, Casacuberta et al. [29] observed near wall vortices in his DNS study, which is postulated to be the major player in perturbation growth downstream of the step.

Recent hot-wire measurements performed by Rius-Vidales et al. [6] on the M3J, provides a detailed temporal analysis into the origin of instability in the boundary layer. The authors observe bandpass filtered fluctuations aligning with high wall normal gradients, corroborating the results of Eppink [37]. These fluctuations are theorized to present from unsteady mechanisms arising on the FFS edge.

3.3. SUMMARY

In order to achieve low levels of skin friction drag and thus improve fuel efficiency, studies have worked towards maintaining laminar flow over a large portion of the airfoil. This involved implementation of active and passive flow control techniques to delay boundary layer transition. However, research focused on extending the concept to operational environments have shown that constraints in manufacturing and maintenance suppress the effectiveness of laminar flow control techniques. It was identified that LFC depends heavily on the smoothness of the aircraft. Two dimensional irregularities due to steps and gaps are inevitable on aerodynamic surfaces. So efforts were directed to understanding the physics behind surface excrescences induced transition and to the development of correlations and criteria in order to predict the effects of these irregularities on the boundary layer. Past works have shown that forward facing steps are less sensitive to transition than their backward facing arrangements, and thus it becomes easier to define less restrictive tolerances for the same. While some studies have been conducted on unswept flat surfaces where TS waves are the dominant instability, others have experimented on swept surfaces wherein crossflow instability becomes prevalent. While there have been various advancements in this domain, what still lacks is a clear understanding of the physical mechanism at play, which is applicable across a range of testing and operational environments.

While unswept surfaces provide a great deal of information about the transition process, addressing the context of application to a modern subsonic transport aircraft, study on swept surfaces would be the more relevant choice. Although crossflow instability is only one among the four major instabilities generated on a swept wing, past works have illustrated that this instability is the least understood and the most relevant since the other instabilities can and have managed to be suppressed by making minor geometric changes to swept surface design.

It is known that inspection panels which contain joints (such as the lap splice joint) on a wing surface gives rise to forward and backward facing steps. However previous research has furnished that of these two types, the forward facing step is less sensitive to transition on swept as well as unswept surfaces. Consequently, it becomes less restrictive to specify manufacturing tolerances for a forward facing step. This quality of the forward facing step makes it an attractive option to have on aerodynamic surfaces and thus will be studied in this project.

Previous experimental works centered around studying the crossflow instability interaction with forward facing steps, have hypothesized with a wealth of information regarding the possible flow physics which occurs in the vicinity of the step. Some works have also gone on to provide criterion for predicting transition. However, as mentioned previously, these prediction tools could not be reproduced to a universal scale, such that it becomes applicable to any wind tunnel or operational environment. This can only be achieved on performing a fundamental study on the development and breakdown on stationary crossflow vortices. The main research objective of the current study is thus to further the understanding of stationary crossflow instability interaction with forward facing step on a swept flat plate. This leads to formulation of the following research questions.

3.4. RESEARCH QUESTION

The research question aims to address the physics behind the interaction between cross-flow instability and forward facing step and serves as a validation of mechanism observed in recent works.

How does the initial crossflow amplitude affect the growth and development of stationary crossflow vortices in their interaction with a forward-facing step on a swept flat plate?

- How do the experimental observations compare with the CF dominated transition scenario found in the literature and from numerical estimates?
- What effect does the variation of initial crossflow amplitude have on the movement of transition locations?

The upcoming research work hopes to provide more clarity in the description of the mechanism of interaction of the cross-flow instability in the vicinity of a forward facing step. The study will focus on the unsteady effects which are dominant in when stationary crossflow vortices interact with a forward facing step.

4

MEASUREMENT TECHNIQUES AND DATA ANALYSIS

The following chapter presents a theoretical background on the flow visualization and measurement techniques employed in this research work. Furthermore, the chapter provides the methodology and the flow metrics used in the analysis of the hotwire data and infrared images.

4.1. FLOW DIAGNOSTICS

The qualitative observation of the flow field can give numerous insights into the transition mechanism at play especially in complex flows which develop in the vicinity of a step. In any experimental study, the trustworthiness of the data is directly associated with the robustness and effectiveness of the flow measurement technique to be able to capture the flow field. For experiments which focus on development of instabilities in the flow, it becomes necessary to be able to observe the flow at distances from the wall at the the order of boundary layer thickness. While there are various flow measurement techniques which can achieve this, the shortcomings and uncertainties of the same must be understood to best quantify the data.

4.1.1. INFRARED THERMOGRAPHY

Infrared thermography takes advantage of the principle that the turbulent boundary layer is associated with a higher wall shear stress (C_f) than the laminar boundary layer as discussed in the previous chapter. Reynolds' analogy associates the increased wall shear to an increase in heat transfer. Therefore in the case of active heating, the final wall temperature is lower in a turbulent boundary layer than its laminar counterpart. The technique measures this temperature gradient to identify the location of transition. In this technique, the wind tunnel model is actively heated by irradiating halogen lamps, printed electric circuits by Joule effect or in the case of the present set up using a silicon heater and cooled by the flow convecting the heat from the body. IR assumes negligible heat conducted through the model. The infrared radiations emitted by the model are converted into current or voltage by a sensor. The advantage of IR is that it is a fast and robust flow visualization technique. It allows for multiple observations of the flow to be averaged in ordered to reduce the occurrence of uncorrelated sensor noise. In the present study, the thermal imaging was done by two Optris PI 640 (640 × 480 px^2, 7.5 - 13 μm spectral range, 75 mK of sensitivity and ± 0.1 C of accuracy) cameras with 60 mm lenses. As shown in Figure 4.1, IR-B was positioned to capture a zoomed in view close to the step (74 mm × 125 mm centered around $z/b_z = 0.43$ and $x/c_x = 0.49$). IR-A was adjusted to achieve full field view (207 mm × 313 mm centered around $z/b_z = 0.41$ and $x/c_x = 0.69$) . Uniformly active heating of the model was achieved through silicon heaters stuck in grooves behind the model.

CALIBRATION

A calibration is performed in order to transform the images from pixel space to physical space. This would aid in estimating transition locations. The calibration involves positioning of a white sheet with equidistant black dots on the model. When the model is actively heated by silicon heaters and halogen lamps without flow, the black dots radiate more heat than the surrounding white background, thus allowing them to become visible in the temperature maps. The known position of these black dots aid in dewarping the image and identifying the chordwise locations of

transition fronts. This process of dewarping and identification of the transition front will be elaborated upon in the coming section.

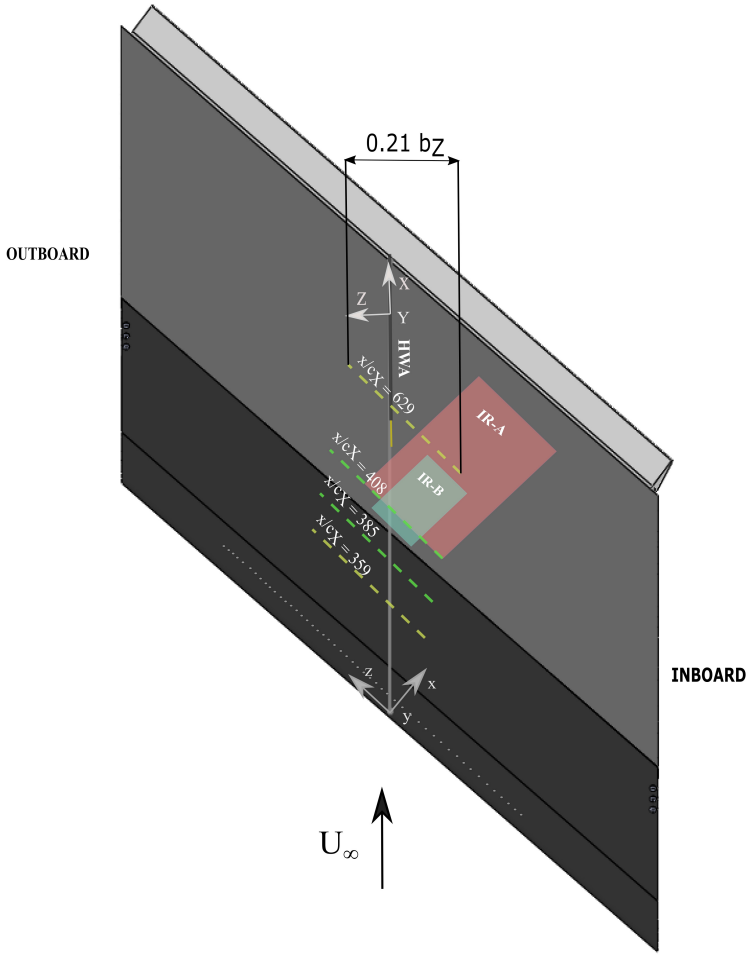

Figure 4.1: Schematic of flow visualization and measurement planes. Yellow dashed lines indicate the initial and final measurement planes for the preliminary measurement campaign. Green dashed lines indicate the initial and final measurement planes for the measurement campaign with steps.

4.1.2. HOT-WIRE ANEMOMETRY

While flow visualization provides a qualitative image of the flow, a flow measurement technique is essential in quantifying the relevant parameters within the flow field. Hot-wire anemometry serves this purpose by utilizing a small heated wire to obtain the velocities in the flow-field. A single wire P-15 Dantec boundary layer probe (the shape of the prong allows near wall measurements) was used. These probes were operated by a TSI IFA-300 constant temperature anemometer.

The Wheatstone Bridge is the main control circuit for the constant temperature measuring process involved in HWA. The Wheatstone bridge is said to be balanced when the ratio of two of its adjacent resistances is equal to the ratio of its other two adjacent resistances. The hot-wire probe acts as one of those resistances that is in balance with the other three resistances. When a specific amount of current passes through the wire (sensor), it is heated (by Joule effect) up to a particular temperature, which depends on the overheat ratio of the hot-wire.When the wire senses a fluid with higher velocity, more heat is lost through convection. In an attempt to keep the temperature of the wire constant, more current flows through the wire and by Ohm's law more voltage flows through wire. This increase of current heats up the hot-wire probe to its initial value such that the resistance that is required to restore the balance across the Wheatstone bridge is achieved. This voltage recorded is proportional to the velocity of the flow. A calibration curve is obtained by matching the voltage recorded to various known flow velocities. The calibration curve is fitted with a fourth-order polynomial to obtain the King's Law coefficients [27].

The hot-wire scanning was done on the $y-z$ plane at select chordwise stations. The probe was aligned with

the wind tunnel fixed coordinate reference system (XYZ), and thus the effective velocity measured Q is given as a resultant of the velocities (u, v, w) aligned with the model fixed coordinate system (xyz).

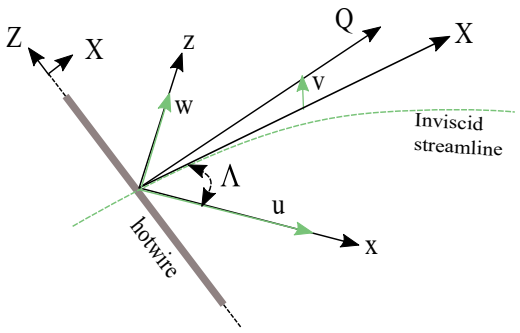

Figure 4.2: Hot-wire reference system

$$Q = \sqrt{(u\cos\Lambda)^2 + (w\sin\Lambda)^2 + v^2} \tag{4.1}$$

where Λ is the sweep angle. The effective velocity Q measured by the hot-wire holds the components of u, v, and w from the swept wing reference frame.

A constant temperature anemometer is preferred over a constant current variant because there is a decreased risk of burnout since the temperature is fixed and it is associated with a faster response attributed to the reduction in thermal inertia [27]. Furthermore, it has low sensitivity to noise at higher velocities. While hot-wire anemometry still remains a popular choice for experiments on transition , since it is associated with fast receptivity/dynamic response (accredited to the low heat capacities of the materials used to make up the wire such as gold and tungsten) being able to capture fluctuation velocities in the flow field. While this is true, HWA is an intrusive technique and a single wire probe can only measure the magnitude of the resultant velocity, making it a less attractive technique to study recirculating flows near steps.

The intrusiveness of this flow measurement technique calls into question its trustworthiness for flow stability experiments wherein the introduction of a small perturbation can become significant. However, as detailed in [15], previous investigators have shown using naphthalene flow visualization experiments ([44]; [58]) that hot-wire data correspond exactly to the flow visualization data, which does not employ any intrusive devices. Furthermore, there was excellent correlation between the experimental hot-wire data of [51] and the computational data of [65], which reinforces the idea that the boundary layer behaviour is unchanged by the presence of the hot-wire. Finally, in the breakdown region, the instability mechanism is driven by an inviscid instability that does not depend on the pressure gradient (which is modified in the presence of hot-wire and sting).

The measurements involving the characterization of the clean plate without step were performed over a larger streamwise extent , wherein the hotwire traversed from $X/c_X = 0.359$ to $X/c_X = 0.629$. The edges of this measurement domain is indicated as yellow dashed lines in Figure 4.1. On the other hand, for the measurements where in steps were employed, the hotwire traversed a shorter streamwise distance from $X/c_X = 0.385$ to $X/c_X = 0.408$ close to the step. This measurement domain is represented by blue dashed lines in Figure 4.1.

CALIBRATION

The hot-wire is calibrated by positioning a Pitot static tube close to the hot-wire in the wind tunnel test section such that the static port is aligned on the same chordwise plane as the hot-wire. This is because the total pressure is the same at every point inside the test section. The Pitot tube is placed in the freestream in the wall normal direction, such that the streamlines curving in the boundary layer does not affect the differential pressures measured by the Pitot tube. The Pitot tube measures the difference between the static and total pressures which corresponds to the dynamic pressure Δp. The flow velocity can be calculated from the dynamic pressure by Bernoulli equation as follows:

$$U = \sqrt{\frac{2\Delta p}{\rho}} \tag{4.2}$$

where ρ is the fluid density, which is related to the ambient conditions as $\rho = p/RT$, where p is the ambient pressure, T is the ambient temperature and R is the gas constant ($R_{air} = 287 J/(kgK)$). For the calibration, the flow velocity is

varied from 0 to the highest operating velocity for the experimental study. The velocity reading from the Pitot tube together with voltage reading from the hot-wire form the calibration curve by King's law:

$$E^2 = A + BU^n \tag{4.3}$$

where E is the voltage and A,B and n are the calibration constants. Since the velocity measured by the Pitot is dependent implicity on the ambient temperature and pressure, the calibration curve is sensitive to changes in these ambient conditions. As a result, within this study, for the preliminary measurements, hot-wire calibration is performed once before the unforced conditions and once before the forced. Moreover, for the final campaign, a calibration was performed before the lower amplitude forcing case and once after the bent hot-wire was replaced.

4.2. DATA ANALYSIS

Recapitulating what was described in the previous section, hot-wire probes are utilized to make a quantitative study of the flow field, while Infrared thermography provides a qualitative picture of the flow field and aids in identification of transition fronts. Since the location of concern for studying instability mechanism is very close to the wall, there arises a demand for capturing the velocity profiles in that zone. However there are certain limitations to the usage of hot-wire probes which when understood, gives the user an arsenal of tools to overcome them. The following sections expand up on the data analysis tools used for IR and HWA.

4.2.1. UNCERTAINTY ANALYSIS

Obtaining reliable results from hot-wire anemometry requires the quantification of uncertainty in the measurements. Error sources in HWA comes from probe contamination/oxidation, probe vibrations, wall proximity, ambient temperature changes, eddy shedding from cylindrical sensors [18]. While systematic errors come from the measurement system, random error is introduced into an experiment due to the inherent fluctuations of the quantity to be measured [28]. It is not possible to quantify the uncertainty from systematic errors. But, high accuracy levels can be ensured during the setting up of the hot-wire data acquisition system.

Random errors can be quantified by calculating the statistical uncertainty. In the present study, the quantity of relevance is velocity. For independent samples which follow a Gaussian distribution, wherein the measured velocities are within one standard deviation from the true value, the measurement uncertainty on the mean velocity is given by Sciacchitano et al. [2]:

$$U_{\overline{Q}} = \frac{\sigma}{\sqrt{N_{eff}}} \tag{4.4}$$

where σ is the velocity standard deviation and N_{eff} is the number of effective independent samples.

$$N_{eff} = \frac{T}{2T_I} \tag{4.5}$$

where T is the total measurement time and T_I is the integral time scale. The velocity standard deviation σ is estimated by:

$$\sigma = \sqrt{\left(\frac{1}{N-1}\sum_{i=1}^{N}(Q_i - \overline{Q})^2\right)} \tag{4.6}$$

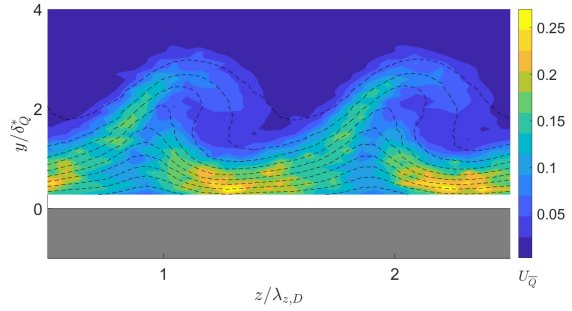

Figure 4.3: Velocity uncertainty field from preliminary hot-wire measurements, last plane of measurement $X/c_X = 0.629$, forced by DREs, $\lambda_{z,D} = 9$ mm, $Re_{c_X} = 1.08E+6$.

The uncertainty in the mean velocity is presented in Figure 4.3. The highest uncertainty is found to appear near the wall where there is a dominance of wall shear and strong velocity gradients. For an external velocity of 23.4 m/s, the maximum statistical uncertainty of the mean velocity is estimated as:

$$\epsilon_{\overline{Q}} = 0.25/23.4 = 1.07\%. \tag{4.7}$$

4.2.2. WALL FINDING

As mentioned above, one probe is used to measure the boundary layer velocities. However, the boundary layer probe does not give accurate measurement of velocities close to the wall. This limitation occurs due to two reasons [14] :

- At low velocity magnitudes close to the wall, the hot-wire probe is influenced by conduction of heat to the wall in addition to the convection with the flow. This conduction of heat to the wall, distorts the velocity profile near the wall.
- Since the wires are very fine, contact with a solid surface such as the wall very often damages the sensor. Thus it becomes common practice to omit velocity measurements between 12% to 20% (18% in White and Ergin [14]) of the free stream velocity.

This drawback of hot-wires to collect data close to the wall, implies that the location of the wall is unknown in the traverse's coordinate system. This brings into the picture a requirement to locate the wall. Numerous approaches have been established for wall finding. The most popular technique which is performed for the current study involves collecting the data for the entire domain and implementing the following steps:

- Perform a spanwise average of the velocities and wall normal y values. This spanwise average is valid since variation of the wall location in the spanwise direction is corrected for by the traversing script.
- The "tail" in the velocity profiles resembling an inflection (which originates due to the conduction of heat with the wall) is removed. The second derivative of velocity shows a peak where the inflection exists. The location of this inflection is taken to be the limit below which the velocity values are non-physical and thus are neglected.
- Once the tail is removed, a linear fit is performed using range of velocities upto a cut-off ($U(y) \leq 35\%$ of freestream velocity [59], [14]). The fit performed is linear due to the physical reason that a laminar boundary layer has a linear velocity profile near the wall.
- The location where this line meets the y axis is noted and the y coordinates are shifted in the positive y axis by this value.

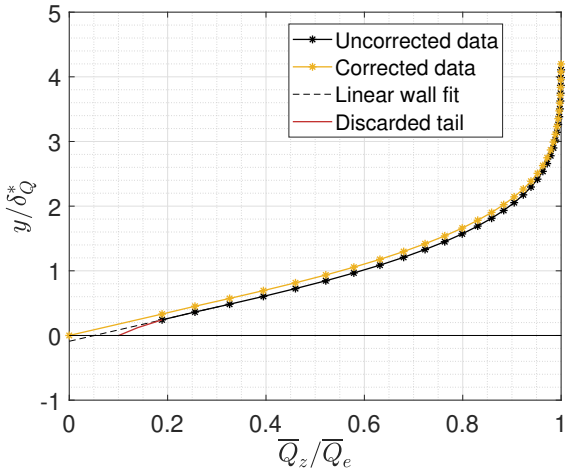

Figure 4.4: Linear wall fit

Another method referred to as Slice [14], involves finding the wall while the hot-wire scans across the y-z planes. Wall normal scans are made in for every spanwise location. This is an attractive choice since velocity profiles are obtained the way would picture a velocity profile to be. At the end of every scan, the points corresponding to velocity

less than 35% of the freestream are taken to generate a least squares linear fit. On estimating the wall location to be the point where $U = 0$, the profile is shifted in the positive y axis by the wall location value. Since data is obtained for every z station of the $y-z$ plane, the approach was titled slice. However the drawbacks that this method suffers have been reported by the authors. Firstly, the method produces erroneous wall estimates when the velocity profile has a considerable curvature near the wall. Furthermore, it does not compare the wall locations from one z location to the next.

The authors also describe another strategy to scan the flow field. The method called Dice involves positioning the hotwire outside the boundary layer, and moving it in the positive spanwise direction stopping to collect data at every z location for a particular wall normal location. Once the scan ends at that wall normal height, the wire moves back to the starting z location and then moves in the negative wall normal direction by one step, closer to the wall and repeats the scan. Here a local least squares fit is performed for every spanwise location with the points corresponding to velocity less than 35% of freestream velocity. The advantage of this approach is that the wall location estimate can only be performed at particular spanwise locations which are independent of upstream roughness. This omits the possibility of systematic errors. The local least squares fit is employed for spurious data in this study.

Additionally, Epplink and Wlezien [42] address the issues of misaligned traverse or minor surface roughness on the aerodynamic surface. This would cause a variation in the wall locations along the span. They suggest filtering out the variations used a spatial low pass filter, in order to keep only the high wavelength variations. The authors report that low wavenumber variations are attributed to traverse misalignment and/or surface roughness. Furthermore, the variations from profile to profile are also filtered out as they are attributed to the inherent uncertainty in the linear fit wall finding approach or the influence of being close to the wall on the HWA data.

4.2.3. SPATIAL ANALYSIS

The data collected from a hot-wire can be spatially and spectrally analyzed to study crossflow instability. $z-y$ contours of temporally averaged velocity can indicate qualitatively how the crossflow vortices are spatially located along the span and in the wall normal direction. The movement and evolution of the crossflow vortices in the streamwise direction can also be visualized. Contours of temporal root mean square of the velocity depict where the fluctuations in the plane arise and can be used to study the origin of instability. The steady velocity field can be spanwise averaged to give a mean velocity profile at each streamwise station $\overline{Q}_z(Y)$. This velocity profile represents the sum of the basic flow velocity and the mean of the steady disturbances. The standard deviation in the spanwise direction of the steady velocity field gives, what is called, the stationary crossflow mode shape $\langle \hat{q}(Y) \rangle_z$. The mode shape is a great indicator of the advent of nonlinearities in the flow field [51].

$$\langle \hat{q}(Y) \rangle_z = \sqrt{\frac{1}{n} \sum_{j=1}^{n} \left(\overline{Q}(Y, z_j) - \overline{Q}_z(Y) \right)^2} \tag{4.8}$$

The quantification of the strength of the crossflow vortices comes from a parameter called the stationary crossflow amplitude A, which as discussed in 2, is thus used in estimation of N factors. The stationary crossflow amplitude can be estimated by three methods.

$$A_{int} = \frac{1}{\delta_{99}} \int_0^{\delta_{99}} \langle \hat{q}(Y) \rangle_z dY \tag{4.9}$$

$$A_{max} = \max\left(\langle \hat{q}(Y) \rangle_z \right) \tag{4.10}$$

$$A_{zFFT} = \max\left(zFFT(\overline{Q}(Y)) \right) \tag{4.11}$$

In some cases, the integral and the maximum of the stationary crossflow mode shape yield amplitudes which are distorted by noise from the harmonics of the forced mode. In order to only acquire the amplitudes corresponding to the forced mode, a spatial fast fourier transform of the time-averaged velocity field is performed in the spanwise direction for every wall normal location. The amplitudes corresponding to the DRE forced wavelength are taken. Finally, the maximum of the amplitudes along the wall normal direction is taken to be the stationary crossflow amplitude. The N factors are calculated from the amplitudes by the formula derived from e^N:

$$N_{int} = log\left(\frac{A_{int}}{A_{0,int}} \right) \tag{4.12}$$

$$N_{max} = log\left(\frac{A_{max}}{A_{0,max}}\right) \tag{4.13}$$

$$N_{zFFT} = log\left(\frac{A_{zFFT}}{A_{0,zFFT}}\right) \tag{4.14}$$

It should be noted that A_0 corresponds to the crossflow amplitude of the most upstream measurement plane.

4.2.4. SPECTRAL ANALYSIS

While the spatial distribution of the velocity fluctuations provides useful information about the flow structures that occur after the step, the time-varying nature of the flow also warrants the study of spectral distribution of it's velocity fluctuations. The spectra at select locations are used to identify the dominant frequencies in the different modes (types 1, 2 and 3) of the secondary instability. The locations at which the spectra are sampled are decided by the locations along the span and wall normal direction at which the mode in question would occur. This was highlighted in subsection 3.1.4.

WELCH'S PERIODOGRAM

Welch's periodogram estimates the power spectral density and the process involves dividing the time signal into successive windows, forming the periodogram for each window, and averaging. For a time signal x(t), the average power is given by [55] :

$$P = \lim_{T->\infty} \frac{1}{T} \int_{-\infty}^{\infty} |x(t)|^2 dt \tag{4.15}$$

Parseval's theorem states that, the energy of a signal in the time domain is equal to the the energy of the transformed signal in the frequency domain. From Parseval's theorem, the average power is written in the frequency domain as follows:

$$P = \lim_{T->\infty} \frac{1}{T} \int_{-\infty}^{\infty} |\hat{x}(f)|^2 df \tag{4.16}$$

On evaluating the above integral, the power spectral density is given by:

$$S = \lim_{T->\infty} \frac{1}{T} |\hat{x}(f)|^2 \tag{4.17}$$

The frequency resolution of the time signal was set to 10 Hz. With 51200 Hz being the sampling rate of the signal, the number of samples in each window for which the Welch's method is employed effectively becomes :

$$\frac{51200}{10} = 5120$$

Windowing is a technique which is performed prior to Fourier decomposition, to account for the nonintegral number of periods in a real and continuous time signal. In this study, a Hanning window was used as it showed sufficient side lobe attenuation and amplitude reduction to 0 at the ends of the signal. The windows were overlapped at 50%. The power spectra of the windows are calculated by squaring the magnitude of the discrete Fourier transform of the time signal. The discrete Fourier transform is estimated by the fast fourier transform algorithm. Finally, the spectra are averaged to reduce the variation of the periodogram.

BUTTERWORTH FILTER

The Butterworth filter is a class of digital filters designed to have a frequency response as flat as possible in the passband [60]. The filter features a sharp frequency roll-off and a monotonically varying amplitude function with the frequency given by :

$$H(j\omega) = \frac{1}{\sqrt{1 + \left(\frac{\omega}{\omega_c}\right)^{2n}}} \tag{4.18}$$

where n is the filter order and ω_c is the cutoff frequency. In the present study, a 10th order IIR filter was used to generate band-pass filtered contours of temporal velocity fluctuations $\sigma_{Q,f}$. Zero phase filtering was employed meaning the signal is filtered in the forward and reversed direction to correct for the phase distortion from the first pass.

4.2.5. DIFFERENTIAL INFRARED THERMOGRAPHY

The infrared images obtained are subject to a series of post-processing steps before a unique transition front location can be identified. The methodology followed is based on the work presented by Rius-Vidales et al.[5]. For each case, a temperature map is obtained by time averaging 20 images collected over a span of 5 seconds. A dewarping of the time averaged heat map is performed by a semi-automated algorithm. The algorithm converts the warped image in pixel space to the physical space from a calibration image. The known position of a chosen reference dot in the calibration image allows for a close to accurate conversion of the image into physical space. In the dewarping algorithm, the black dots are identified and the image is transformed such that the flow is from right to left, the spanwise direction in vertical (top of image is inboard) and the chordwise direction is horizontal.

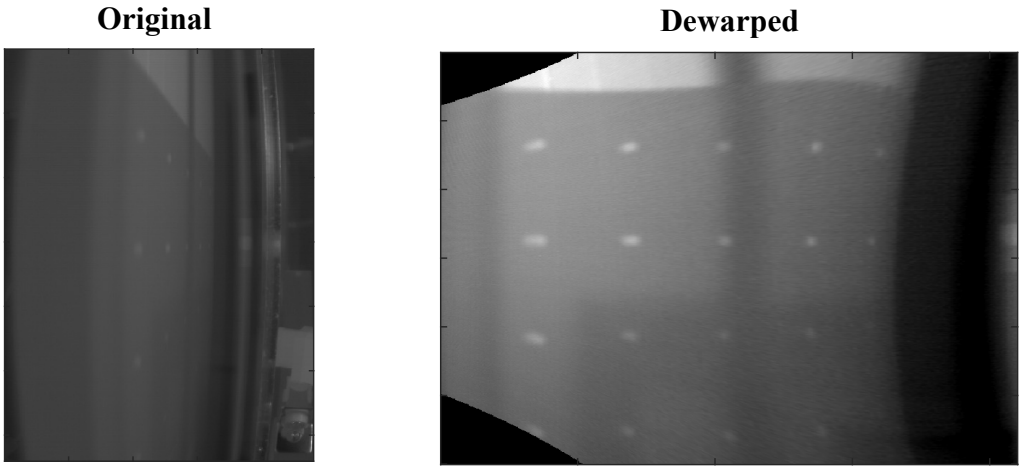

Figure 4.5: Dewarping of Infrared Calibration image

In order to reduce the possibility of a spurious identification of the transition front, differential infrared thermography (DIT) technique is employed. The infrared images are collected at two Reynolds numbers: one at the operating Reynolds number ($Re_{c_X,l} = 1.08 \times 10^6$) and the other at a higher Reynolds number ($Re_{c_X,u} = 1.28 \times 10^6$). The difference between the two time averaged temperature maps gives the required image:

$$\overline{I}_A - \overline{I}_B = \overline{I}_{DIT} \tag{4.19}$$

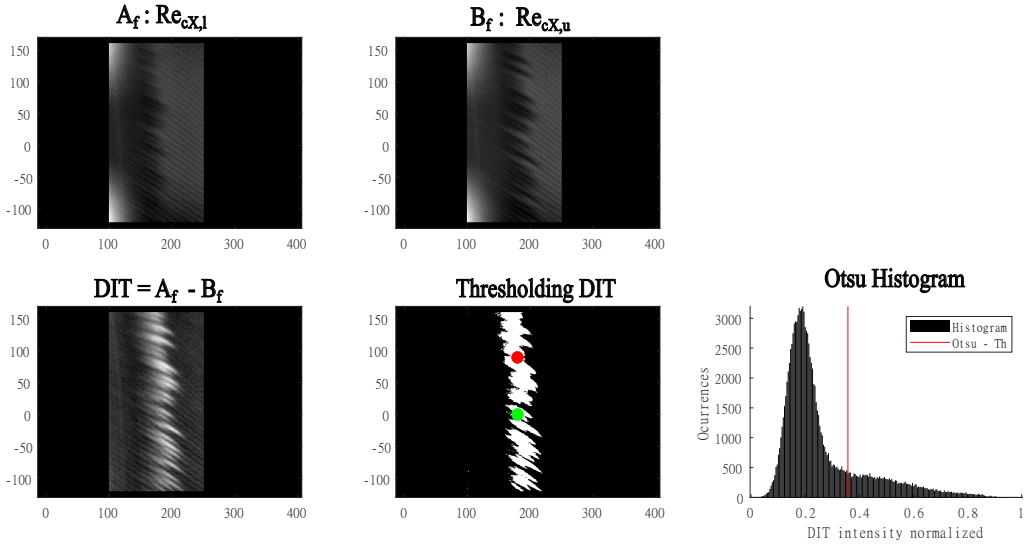

Figure 4.6: Thresholding by Otsu's method

The transition identification algorithm involves the method proposed by Rius-Vidales et al. [3]. To begin with, the DIT image is binarized by Otsu thresholding as seen in Figure 4.6. Otsu's method is reliable when a bimodal

distribution (of black and white pixels) in the histogram is obtained. Therefore, to avoid spurious estimation of a threshold, a mask is imposed to limit the parts of the image to be binarized [54].

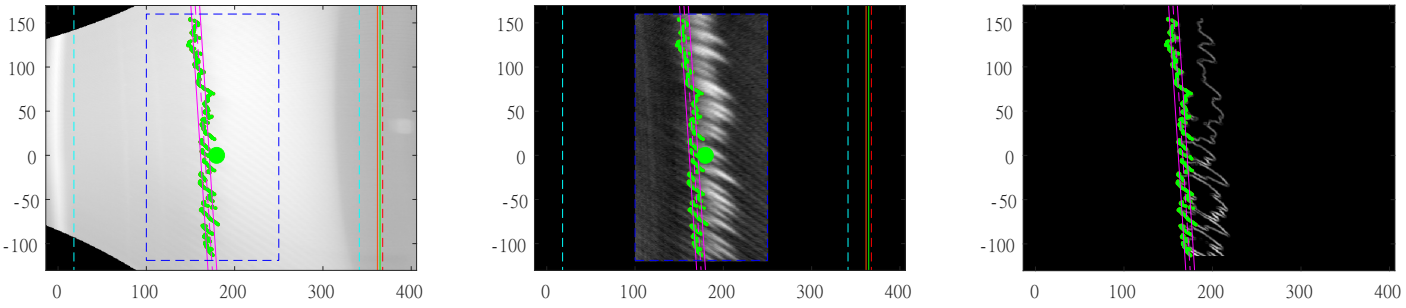

Figure 4.7: Identification of transition front at the lower Reynolds number $Re_{c_X,l} = 1.08 \times 10^6$. The images show the demarcation of domain and the identification of the transition front from the DIT image

The transition fronts are identified from the gradient of the binarized image for the low and high Reynolds number images and a linear fit is made. Using the linear fit, the transition location is calculated at the center of the domain.

5

EXPERIMENTAL SET UP

The test section with the swept flat plate model is designed and manufactured to facilitate fundamental studies on the interaction of steps with crossflow instability. Crossflow vortices develop in a favorable pressure gradient. However, as discussed in the literature study, swept plate boundary layers are susceptible to instabilities besides just the crossflow. Thus, it becomes important to both destabilize CFI while stabilizing other instabilities which may arise. This calls for design considerations being made to the model. Furthermore, to be able to perform quantitative and visualization studies on the flow, the test section as well as the model must be adapted. The adaptations and design considerations are discussed in the following sections. The experimental tests were performed with the facilities available at the low speed laboratory of the Delft University of Technology.

5.1. TEST SECTION

The test section shown in Figure 5.1 fitted with the model is composed of: Polycarbonate windows on the sides of the section, a flat plate model with a movable leading edge and flap, and a flexible wall connected to a series of actuators to create the target pressure distribution of the flat plate.

The Polycarbonate on the side walls of the test section serves as windows through which a Taylor-Hobson microalignment telescope looks to 'find the wall' for hot-wire measurements. The boundary layer which would enter the test section from the circular exit into the convergent duct would be unfavorable for this study, that is, it would be turbulent. If left untreated, this turbulent boundary layer on the side walls would contaminate the boundary layer on the flat plate. Thus, at the bottom of the Polycarbonate windows are aluminium fixtures to bleed the turbulent boundary layer of the wind tunnel and create a new laminar boundary layer on the side wall.

The model is an anodized aluminium 45° swept plate. The swept flat plate model allows for a continuous adjustment of step height by means of manual traversing stages with a resolution of 1 μ m. The back of the plate has a groove on which a silicon heating mat sits for infrared thermography measurements. Anodized aluminium is a poor material for infrared thermography as the material loses most of the heat energy to lateral conduction and not as much to radiation. The emissivity ϵ of anodized aluminium is around 0.77. To correct for this, a removable PVC plate (ϵ = 0.93) is fitted above the step to aid in concentrating the heat energy thus making up for the lack of emmissivity of aluminium. The model will be discussed in detail in the upcoming section. A structure to support a three dimensional hot-wire traverse sits on the back beam of the test section.

The door to the test section is fitted with actuator rods to control the deformation of a flexible PET foil, which serves as a pressure body. An assembly is hinged on the test section where a LASER scanner (Figure 5.1a) is placed to perform a quick characterization of step heights. Two infrared cameras are supported on beams on the door which give a full view of the flow field and a zoomed in view at the step location. The model and the pressure body will be discussed next in more detail.

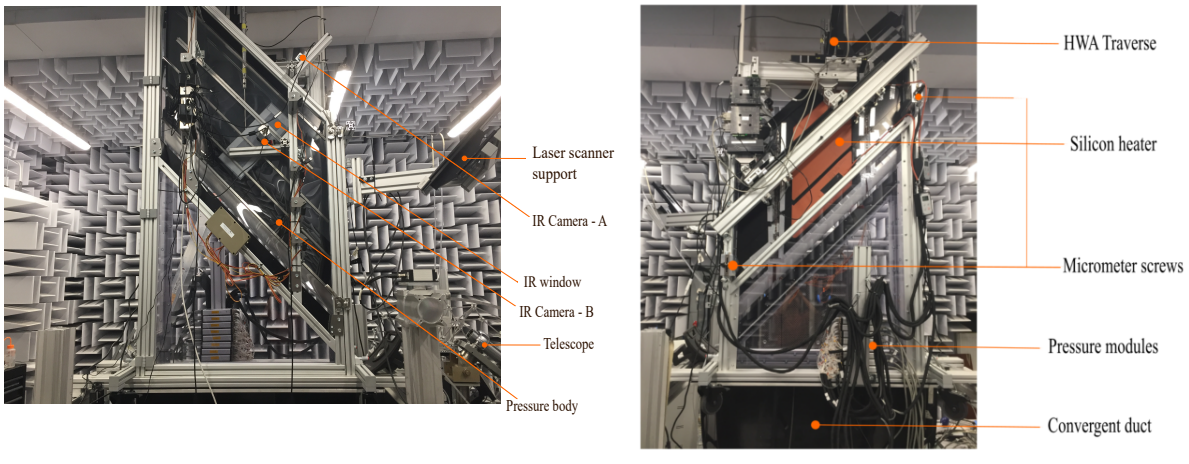

(a) (b)

Figure 5.1: Test section mounted on the convergent duct in the A-Tunnel at the Low Speed Laboratory, TU Delft a) Front view of the test section b) Back view of test section

5.2. MODEL

The model is an anodized aluminium 45^o swept flat plate with a leading edge designed as a modified superellipse (MSE). The motivation behind the MSE is to ensure that there is a smooth surface transition between the curved and flat surface leading to a low receptivity to freestream vorticity [46]. As imaged in Figure 5.2, 3 mm PVC plate is installed to allow IR imaging.

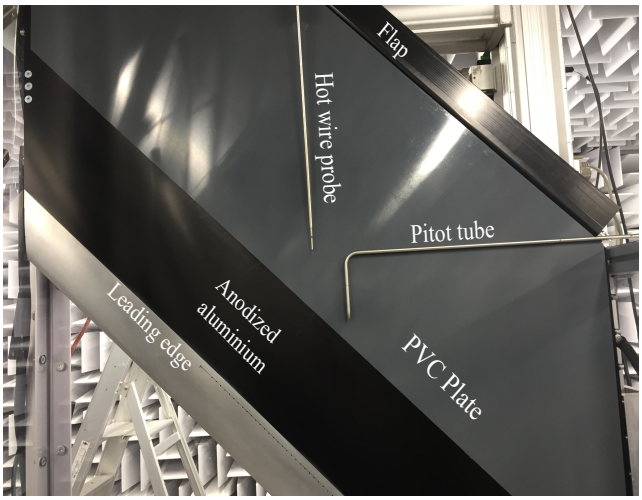

Figure 5.2: Swept flat plate model. The Pitot tube is placed for the purpose of in-situ calibration of the hot-wire.

The model is also fitted with a flap by a hinge mechanism to control the location of the stagnation point at the leading edge. The swept plate has 126 pressure ports of diameter 0.3 mm , 63 on the inboard side ($Z/b_Z = 0.214$) and 63 on the outboard side ($Z/b_Z = 0.775$) of the plate running in from the leading edge on the pressure side to the trailing edge on the suction side of the plate. Spanwise invariance of the flow is ensured by measuring the pressure distributions along the two rows. Of the 63 taps on each row, 32 taps have been drilled before the step location and 29 taps after the step. Of the 32 taps before the step, two taps were drilled on the pressure side of the model in order to identify the stagnation point varying with the flap angles. Owing to the usage of flow measurement and flow visualization techniques on the swept plate, it becomes important to distinguish the two orthonormal coordinate systems at use as shown in Figure 5.3. The model fixed coordinate system is denoted by xyz where positive x runs in the streamwise direction (i.e. normal to the leading edge towards the trailing edge), positive y runs from the wall directed towards the reader and positive z runs from the inboard side of the plate to the outboard side along the span. The global or wind tunnel fixed coordinate system is denoted by XYZ where positive X runs in the streamwise

direction parallel to the wind tunnel walls, positive Y is always normal to the plate surface, and positive Z runs from inboard side to the outboard side of the plate. The coordinate systems are presented on 5.3. The geometric parameters of the swept flat plate are presented in 5.1.

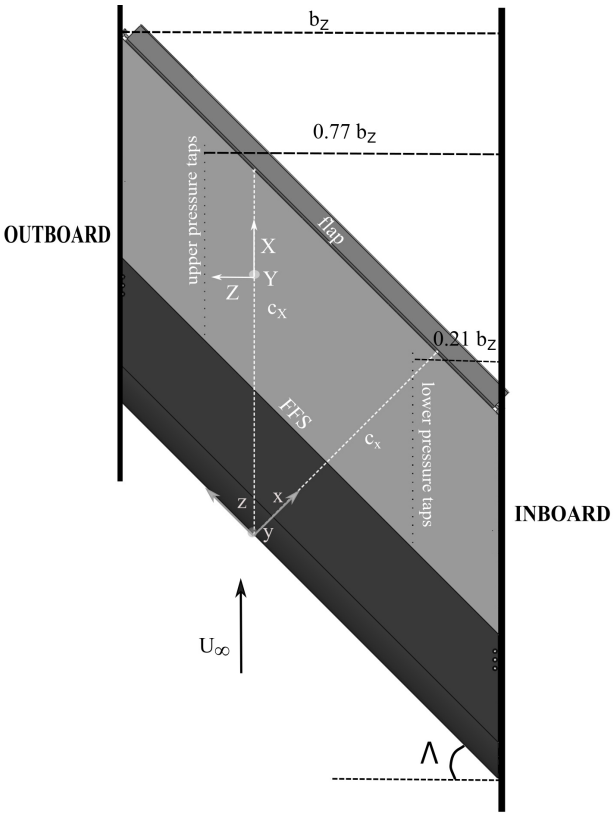

Figure 5.3: Schematic of swept flat plate model indicating the positions of pressure taps. Dashed white lines indicate the streamwise and orthogonal chord.

Λ	c_X [mm]	b_Z [mm]	c_x [mm]	b_z [mm]	X_{step}/c_X	X_{step}[mm]
45^o	848.545	884.00	600.00	1250.165	0.397	337.042

Table 5.1: Geometrical parameters of swept flat plate

5.3. PRESSURE BODY

As the model being studied is a flat plate, the generation of a favorable pressure gradient needed to destabilize cross-flow is created by a pressure body made of polyethylene terephthalate (PET) . The pressure body made of PET is movable at multiple locations by computer controlled actuators positioned on the door of the test section. The PET foil although transparent to visible light, is opaque to infrared radiations. To be able to visualize the flow close to the step, an infrared transparent Silicon based optical access port is installed. Furthermore, to facilitate attached flow over the pressure body, a zig zag strip is installed at the leading edge to the pressure body to trip the boundary layer flow. The pressure body connected to the actuator rods is shown in Figure 5.4. The preliminary experiments characterizing the pressure gradient with the pressure body are discussed in the next chapter.

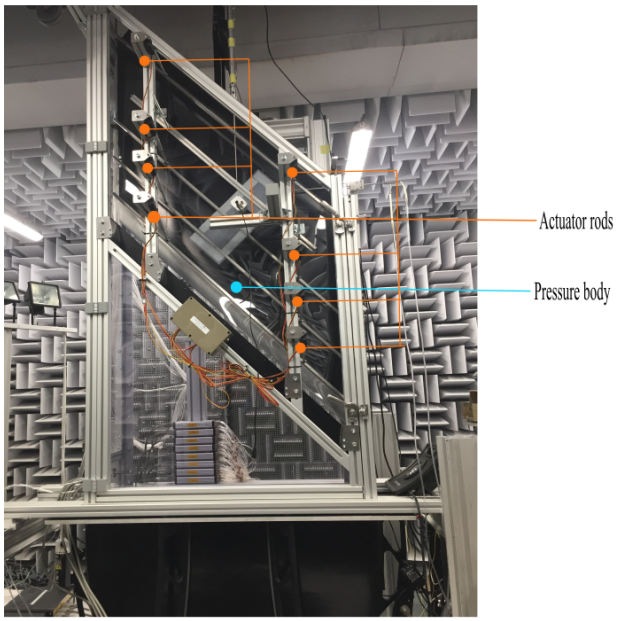

Figure 5.4: Flexible wall with series of actuators to create target pressure distribution on swept flat plate

6

PRELIMINARY MEASUREMENTS

The following chapter presents the preliminary measurements performed on the clean swept flat plate without steps. The characterization of step heights and pressure gradients have been performed. The flowfield for the swept plane without steps is quantified using hot-wire anemometry with and without forcing.

6.1. CHARACTERIZATION OF STEP HEIGHTS

The leading edge of the swept plate is movable by two manual linear stages, which allows for the generation of FFS and BFS. The step heights have been characterized by traversing a micro-epsilon scanCONTROL 30xx LASER scanner along the spanwise direction for 80 mm. For this characterization, the nominal step heights were varied from 0 mm to 2 mm in steps of 0.1 mm. The LASER projects a number of points in a line orthogonal to the step direction centered at each spanwise (z) position. The traversing speed is 5% such that there is no distortion in the collection of profiles in steps of 0.05 mm along the span (z).

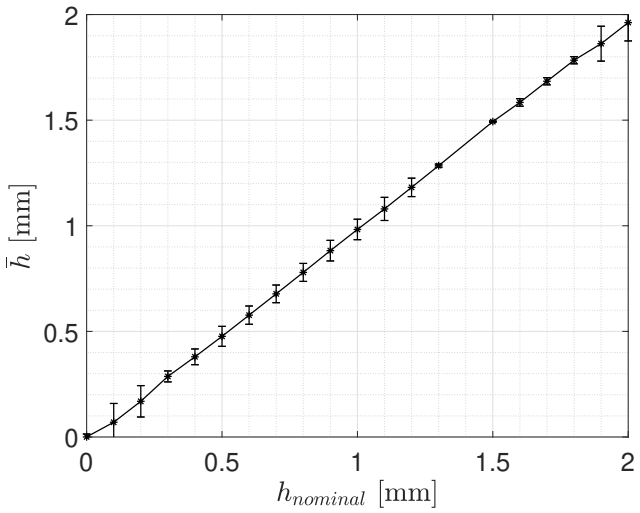

Figure 6.1: LASER characterization of step heights with traverse

Exposure time [ms]	profiles/s	z distance [mm]	step in z [mm]	steps/mm	Traversing speed
10	50	80	0.05	20	0.92

Table 6.1: Specifics of the LASER characterization of step heights

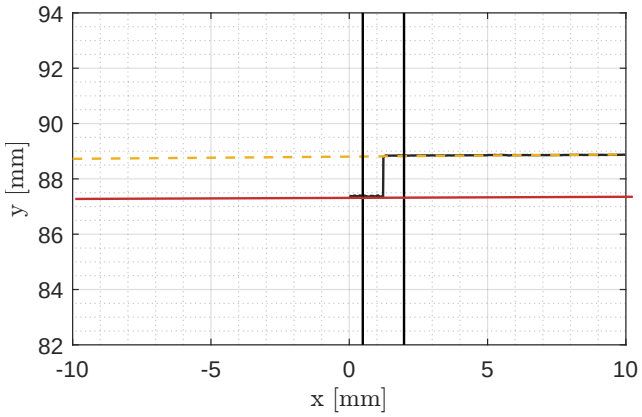

Figure 6.2: Measurement of step height from scanCONTROL 30xx LASER scanner data. Black lines mark the streamwise limits of the analysis.

An in-house code is used to estimate the step heights from the measured data. Of the points projected in a line orthogonal to the step direction, two lines are drawn: the first from the points upstream of the step (red line), and the second from the points downstream of the step (yellow dashed line) as shown in Figure 6.2. The measured step height is calculated as the distance between the two lines, averaged over the spanwise domain. The LASER measured average step heights against the nominal step heights are presented with error bars indicating the standard deviation along the span (z) in figure Figure 6.1 . Besides this characterization performed before the experiment, a real-time measurement of the step heights was additionally performed during the campaign.

6.2. CHARACTERIZATION OF THE PRESSURE GRADIENT

To study crossflow instability, a favorable pressure gradient must be imposed on the flat plate. A favorable pressure gradient is defined mathematically as $-\frac{dP}{dx}$ where flow moves from a region of higher pressure to lower pressure.

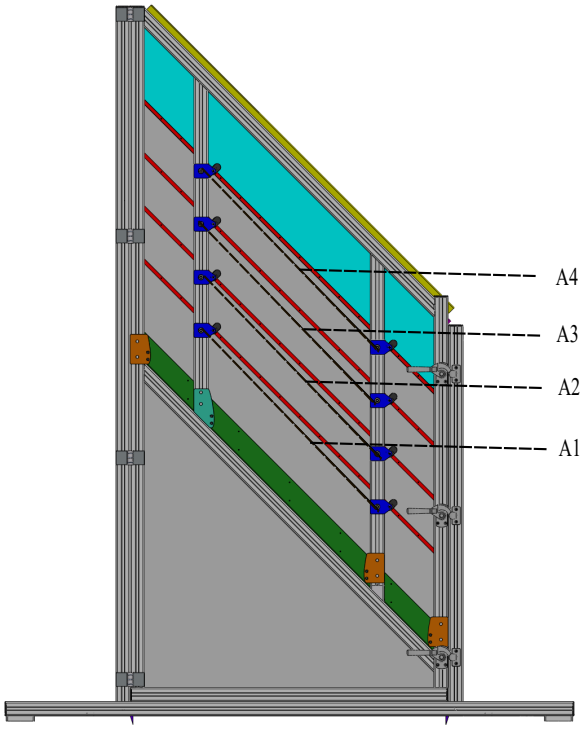

Figure 6.3: Nomenclature for actuator rod pairs fixed to pressure body

The characterization of a spanwise invariant and suitably favorable pressure gradient was performed by an iterative process changing three variables, one at a time : actuator rod positions, angle of the flap and Reynolds number. The pressure distribution along the chord was studied for every iteration . In the swept flat plate model, the pressure taps found flush on the model surface measure the static pressure by pressure modules of varying pressure ranges. The taps close to step are connected to pressure modules of a smaller pressure range. Lower pressure ranges are associated with higher accuracy percentage. In the present study as discussed by Tufts et al. [48], varying the the step height, varies the pressure signature close to the step. Thus, to ensure accurate pressures are measured close to the step, smaller pressure range modules are used. The pressure coefficient is calculated as below:

$$C_P = \frac{P - P_{Static}}{\frac{1}{2}\rho U_\infty^2} \tag{6.1}$$

Here, P is the static pressure measured from the taps on the model. The pressure coefficient is calculated with respect to the Pitot static pressure in this study P_{static}. It is assumed to be close to the ambient pressure as the pitot tube is positioned close to the entrance of the test section, sufficiently far away from the leading edge. The denominator in Equation 6.1 is the dynamic pressure q which is estimated from the difference between the static and total pressures measured by the Pitot tube.

The pressure gradient signature can be understood by the interplay between the velocity components which arise on the swept plate. The freestream velocity U_∞ decomposes into U_e and W_e on the swept plate reference system. While on an unswept wing, C_P shows a value of 1 at the stagnation point, on a 45^o swept wing, the C_P shows a value less than 1 which is calculated from the formula :

$$C_P = 1 - \left(\frac{U_e}{U_\infty}\right)^2 = 1 - \left(\frac{U_\infty \cos 45}{U_\infty}\right)^2 = 0.5$$

This is reflected as -0.5 in the $-C_P$ distribution presented below. The pressure body is connected to the door of the test section by four pairs of actuators. These are positioned such that they span almost the entire chord of the swept plate model. The controller for the actuators allowed for each actuator pair to be moved in tandem and also offset the inboard actuator with respect to its outboard pair. The naming of the actuator pairs is presented in Figure 6.3. Figure 6.4a shows the first trial of the pressure gradient characterization study, where from a zero pressure gradient signature, a preliminary favorable pressure gradient was achieved.

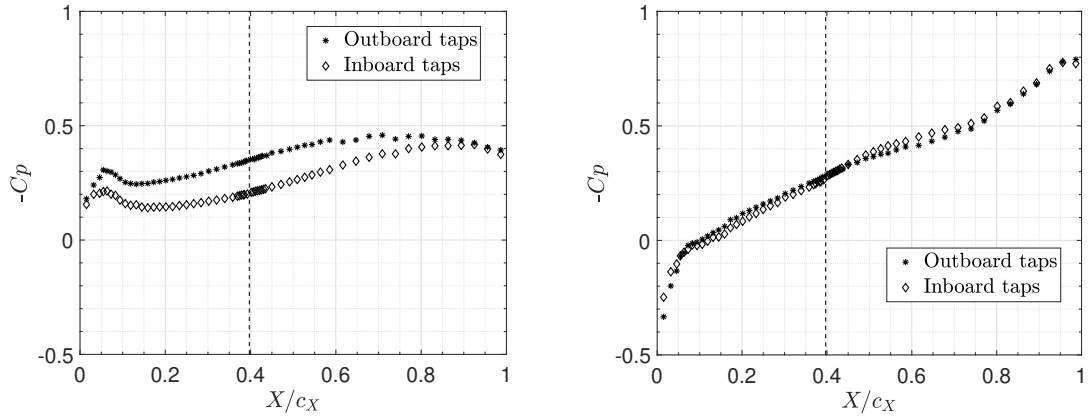

Figure 6.4: Effect of variation of actuator rod positions. Dashed line indicate the position of step. a) $A1 = A2 = A3 = A4 = 40mm, D1 = D2 = D3 = D4 = 0, Re_{c_X} = 1.2E+6$ b) $A1 = 66.2mm, A2 = 79.6mm, A3 = 84.6mm, A4 = 91mm, D1 = 0, D2 = D3 = -8mm, D4 = 8mm, Re_{c_X} = 1.2E+6$

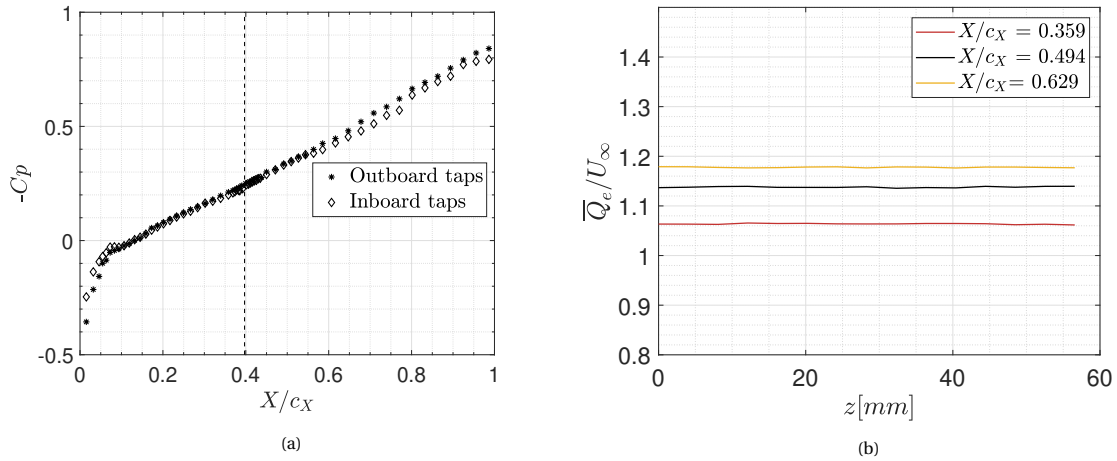

(a) (b)

Figure 6.5: a)Identification of suitable pressure distribution. Dashed line indicates step location. Actuator rod positions and flap angle setting tabulated in Table 6.2, $Re_{c_X} = 1.08E+6$. b) Variation of external velocity (nondimensionalized by U_∞ = 19.45 m/s) along the span for three chordwise stations.

The variation of actuator rods relative to each other along the span corrected the non-uniform blockage effects that appeared in the test section. On observing a non-monotonically varying pressure distribution, structural modifications were made to the pressure body, such as the addition of springs and a rod to keep the PET foil intact on interaction with the flow. The variation of flap angle and actuator rod positions yields the pressure gradient shown in Figure 6.4b.

To ensure the spanwise invariance of the flow field, the external velocity normalized by the freestream velocity over the span is presented for three chordwise stations in figure Figure 6.5b. The minimal variation in the external velocities along the span indicates that spanwise invariance in the flow field was achieved for this study. Furthermore, the velocity is found to increase on moving downstream, corroborating the decrease in pressure coefficient seen in Figure 6.5a.

The free stream velocity and thus the Reynolds number was varied to attain a stronger favorable pressure gradient as shown in Figure 6.5a. The negative pressure distribution signature presented in figure Figure 6.5a, shows high pressures on the the suction side of the model followed by a -Cp of -0.5 at the stagnation point. The pressure decreases monotonically in the chordwise direction with the presence of a strong favorable pressure gradient . The following tables present the settings of the actuator rod positions (A) and offsets (D), flap angle and Reynolds number, at which subsequent measurements would be performed for this study.

A1 [mm]	**A2[mm]**	**A3 [mm]**	**A4[mm]**	**D1[mm]**	**D2[mm]**	**D3[mm]**	**D4 [mm]**
66.2	79.6	84.6	91	0	-8	-8	8

Flap angle	Re_{c_X}
18.2^o	1.08E+6

Table 6.2: Manually optimized pressure coefficient distribution settings

From the set pressure distribution, one can study the external velocity distribution and the pressure gradient distribution along the swept plate chord.

6.3. CHARACTERIZATION OF CLEAN CASE

In studying the interaction of cross flow instability with steps, the characterization of the clean swept flat plate without steps becomes a necessary precursor to appropriately compare results with and without surface irregularities. The measurements were performed with a hot-wire, traversing in the zy plane . The wire was traversed with reference to the model fixed coordinate system. Thus, the crossflow vortices data presented are visualized from downstream. The reader is referred to figure Figure 5.3 for the coordinate system in use.

6.3.1. IDENTIFICATION OF DRE SPACING

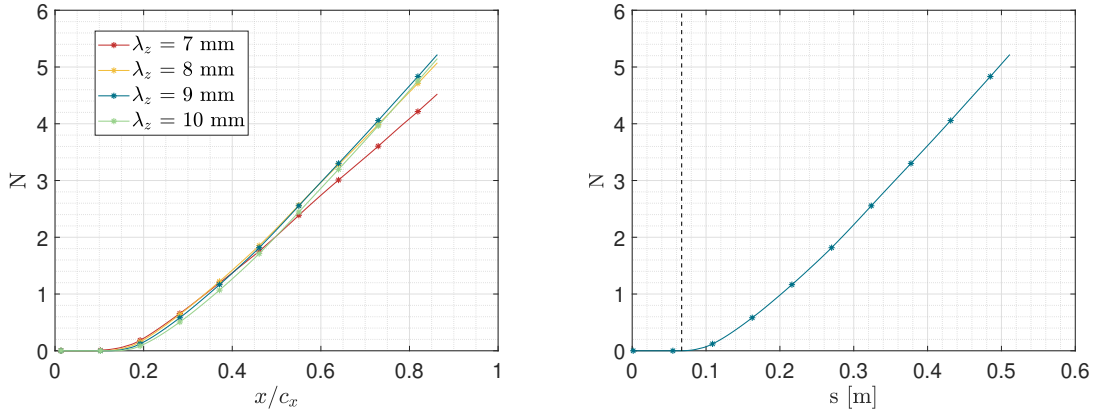

(a) (b)

Figure 6.6: Numerical stability analysis (only one in hundred samples is presented with a marker) a) Evolution of N factor curves along the chordwise direction b) Identification of neutral point at s = 0.067 m for λ_z = 9 mm. Dashed line indicates the neutral point location in surface coordinates.

As mentioned previously , crossflow instability is conditioned in a wind tunnel environment by the use of micron sized discrete roughness elements (DREs) arrays. The spanwise spacing between the DREs is decided by stability analysis. The pressure distribution which was presented in the previous section in Figure 6.5a was utilized to predict the stability characteristics of the flow field. The C_P distribution along the chord was input into an in-house boundary layer solver, and the stability of the resulting boundary layer is studied by solving the Orr-Sommerfeld equations.

The pressure distribution is used to compute the external velocity distribution which goes into a boundary layer solver which in turn computes the base flow from the a specified limit past the stagnation point to the trailing edge in the direction normal to the leading edge. The N factors of the computed base flow are solved for various spanwise wavelengths (λ = 7,8,9,10 mm) and zero angular frequency ω of stationary crossflow. The DREs were spaced corresponding to the spanwise wavelength λ = 9 mm which was found to be the overall maximum amplified wavelength. The maximum amplified mode is found to monotonically grow from the neutral point at 0.11 x/c_X up to 0.86 x/c_X. Since the leading edge of the swept plate plate is curved, the neutral point is identified in the surface coordinates s normal to the leading edge to be 0.067 m. The specifics of the DRE array including the diameter (d_D), height (k_D) , spacing ($\lambda_{z,D}$) and position are reported in Table 6.3

$\lambda_{z,D}$ **[mm]**	d_D **[mm]**	k_D **[mm]**	s_D **[m]**
9	2	0.1	0.067

Table 6.3: Specifics of DRE array

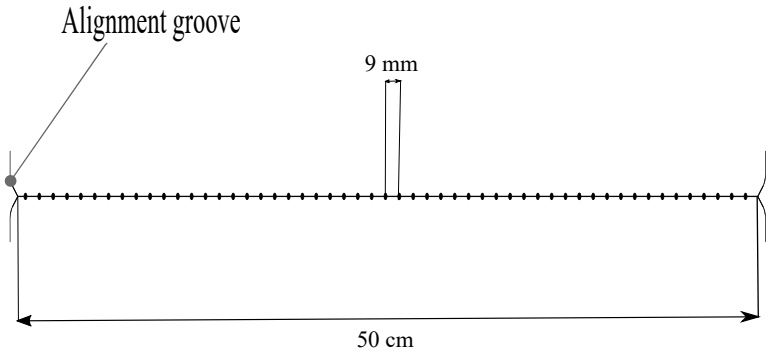

Figure 6.7: DRE design on Inkscape

The DRE cutting stencil was designed as shown in Figure 6.7 with the computed spanwise spacing and with a groove for alignment purposes such that they fall in a straight line. The length of the entire array (50 mm) is set such that the DREs are positioned not too tightly between the inboard and outboard sets of pressure taps. The array is precision cut with a LASER on an adhesive transfer vinyl tape of nominal thickness k_D. Finally , the cylindrical roughness elements are carefully transferred using a template on to the desired location s_D on the surface of the swept plate. To obtain, thicker DRE elements, multiple layers of the vinyl tape are pasted on top of each other before LASER cutting. The specifics of the DREs and their positioning on the swept plate for the present study are illustrated in Figure 6.8

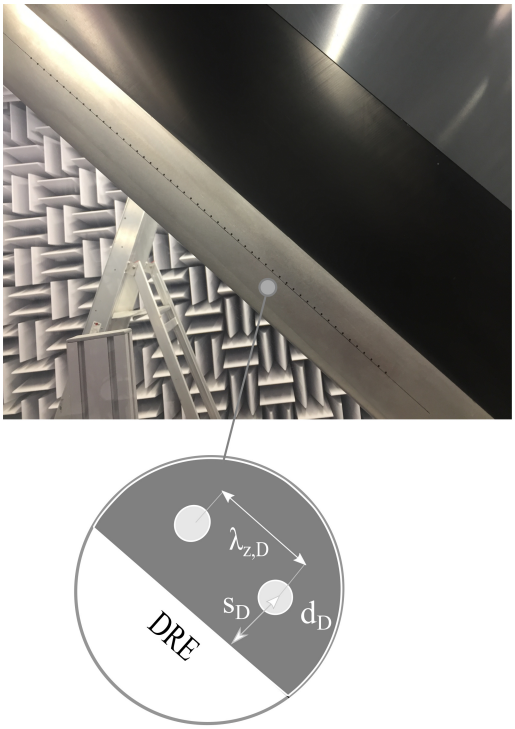

Figure 6.8: DRE positioned on the swept flat plate. Zoomed schematic shows the DRE geometry and location from leading edge.

6.3.2. COMPARISON OF UNFORCED AND FORCED MEASUREMENTS

Hot-wire anemometry was employed to study the effect of forcing on the crossflow instability in a clean configuration. The theoretical background and the arguments for the choice of this measurement technique are elaborated upon in subsection 4.1.2. The variation in atmospheric conditions between two given days can result in differences in the calibration curve. Therefore, the hot-wire is calibrated twice, once for the unforced case and once for the forced to correct for changes in atmospheric pressure and temperature.

Case	DX [mm]	DY [mm]	Dz [mm]	nX	nY	nz	Measurement time [s]
Unforced	28	0.0625	4	10	40	15	2
Forced	28	0.0714	0.5	10	35	50	2

Table 6.4: HWA experimental matrix for preliminary measurements

The hot-wire measurements were performed in zy planes between X/C_X 0.359 to X/C_X 0.629. The hot-wire was traversed in steps of 4 mm for 56.56 mm centered around the midspan in the unforced case and steps of 0.5 mm for 27 mm centered at the midspan in the forced case along the z axis. The hot-wire was traversed in the wall normal direction in steps of 0.0625 mm in the unforced case and steps of 0.0714 mm in the forced case. The steps in the wall normal direction were performed upto a computed boundary layer thickness δ_{99} of 2.5 mm. In order to account for

the misalignment in the traverse and/or the plate in the spanwise direction, the wall was found at the first and last points of each stream wise measurement plane and the misalignment angle was computed. The reader is referred to Figure 4.1 for clarity on the location of the measurement planes under study.

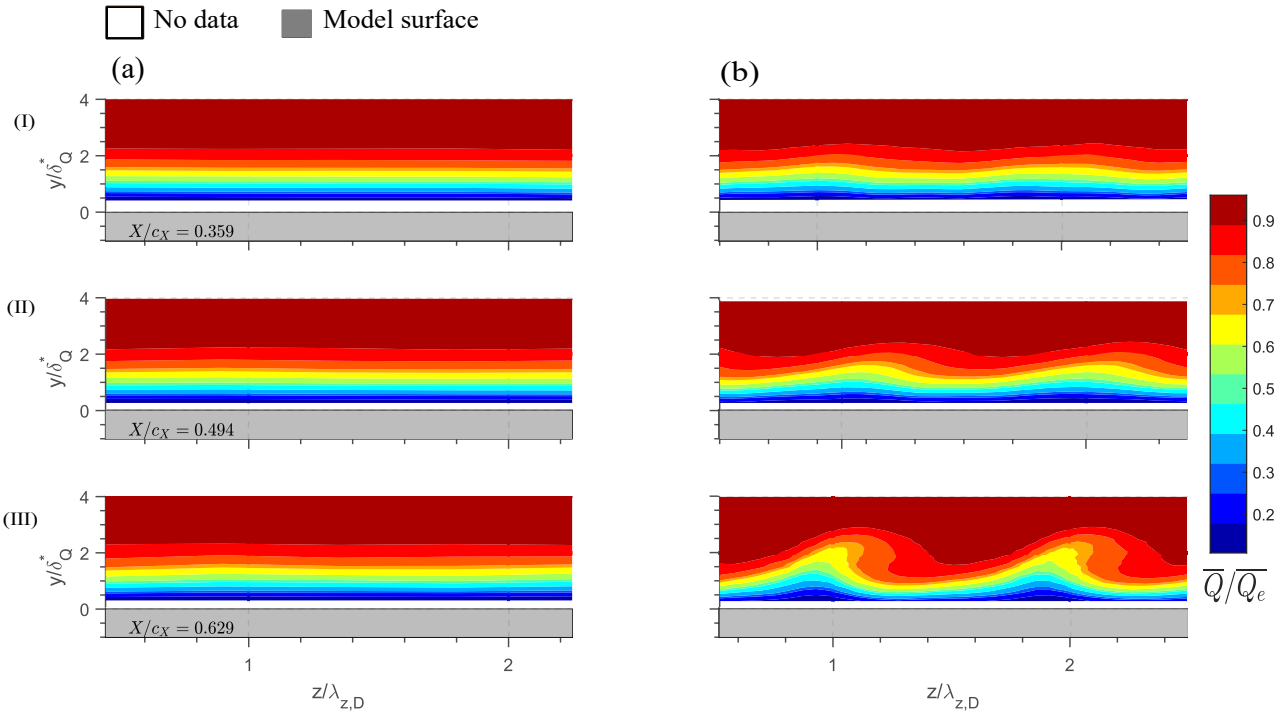

Figure 6.9: Contours of nondimensionalized mean velocity (12 levels) a) Unforced b) Forced with DREs spaced at $\lambda_{z,D}$ =9 mm. Re_{c_X} = 1.08E+6

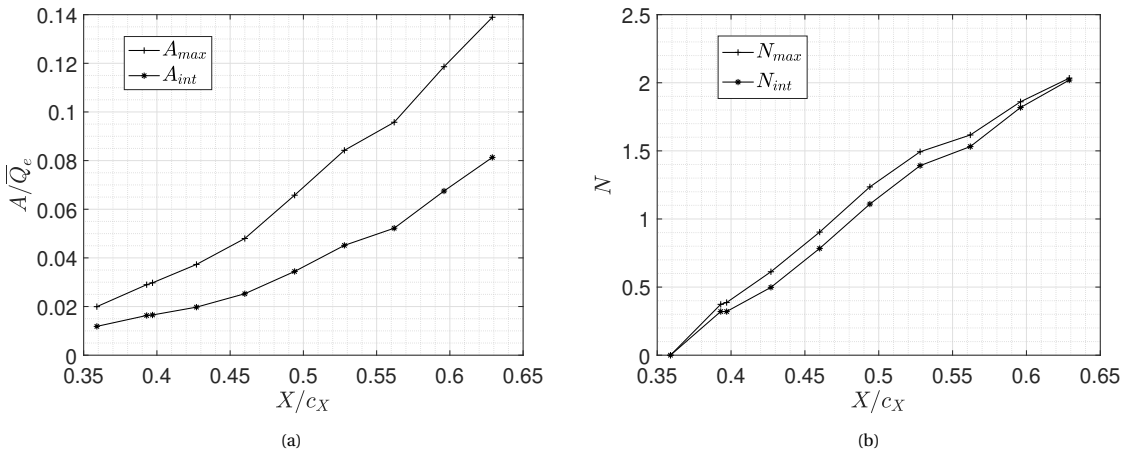

Figure 6.10: a) Stationary crossflow amplitudes along the streamwise direction b) N factors trend along the streamwise direction estimated from stationary crossflow amplitudes for the forced case

The use of DREs narrows the band of modes which destabilize the boundary layer flow, restricting the destabilization to occur for the forced mode and its harmonics [5]. To justify the need for DREs to control the flow, Figure 6.9 presents the mean velocity ($\overline{Q}$) nondimensionalized by the external velocity ($\overline{Q_e}$) contours for the forced case (right) and the unforced case (left) for three streamwise planes: the first (X/c_X = 0.359), middle (X/c_X = 0.494) and last plane (X/c_X = 0.629), cropped to the same location about the midspan. The mean velocity contours for the unforced case show the evolution of waves within the boundary layer. The axes are nondimensionalized: the wall normal axis (y) with the displacement thickness of the most upstream plane (δ^*_Q = 0.5910 mm for forced and δ^*_Q = 0.5890 mm for the unforced case) calculated with the resultant velocity measured by the hotwire (Q) from Equa-

tion 2.2, and spanwise axis (z) with the wavelength of the initial crossflow vortices ($\lambda_{z,D}$ spacing between the DREs). These perturbations remain unamplified as we progress in the streamwise direction (I-III a). On the other hand, as we move downstream within the boundary layer forced by DREs (I-III b), the contours exhibit mean flow distortion. Furthermore, the mean flow in the last plane of measurement (III b) indicates the onset of the rollover phenomenon (as discussed in Reibert et al. [51]), wherein low momentum fluid is brought to the upper part of the boundary layer and high momentum fluid near the wall. This signals the onset of nonlinear evolution. The mean flow shows an arrangement of co-rotating crossflow vortices spaced in the spanwise direction by the fundamental forcing wavelength of 9 mm. The lack of growth of crossflow vortices when moving in the streamwise direction in the unforced case as opposed to the very apparent growth of the vortices in the forced case, indicates a requirement for controlling the flow at the most amplified mode.

Figure 6.10 depicts the stationary crossflow amplitude trends calculated from Equation 4.9 and Equation 4.10 and the N factor curves calculated by the two methods given in Equation 4.12 and Equation 4.13 presented for the forced case. It should be noted that although N factor at a streamwise plane is generally estimated as the logarithm of the ratio of stationary CF amplitude at a streamwise plane to the stationary CF amplitude at the neutral point , the measurement planes for the preliminary measurements only begin at $X/c_X = 0.359$ and so the amplitude of this upstream measurement is taken to be A_o. The N factors and stationary crossflow amplitudes show a monotonic growth along the streamwise direction as anticipated for the controlled growth of crossflow vortices. The amplitudes trend continues to grow indicating the absence of amplitude saturation. The amplitude trend is used to study the mode shape in the coming section. Evidenced by the controlled growth of crossflow in the mean velocity contours in Figure 6.9, N factor and amplitude trends for the forced case in Figure 6.10, the above section reinforces the need for DREs to control the flow. Thus, remainder of the results presented in this chapter would be with the use of DREs.

6.3.3. COMPARISON WITH NUMERICAL DATA

The numerical data obtained from an in-house boundary layer solver is compared with the experimental data from hot-wire anemometry. The boundary layer displacement and momentum thicknesses δ^*, θ are derived from the equations Equation 2.2 and Equation 2.4 respectively. The δ_{99} is obtained as 99% of the maximum spanwise averaged velocity. In the boundary layer solver, the steady and incompressible 2.5D (spanwise invariance) laminar boundary layer equations are numerically solved orthogonal to the leading edge (along x in Figure 5.3), from the external (inviscid) velocity calculated from the measured pressure distribution for the clean case (no FFS) with 1 layer of DREs at the neutral point. The velocities measured in the reference frame orthogonal to the leading edge are then projected to obtain the effective velocity measured by the hot-wire, based on Equation 4.1. It is seen from Figure 6.11 that the boundary layer thickness measured experimentally compare well with the numerically solved thicknesses.

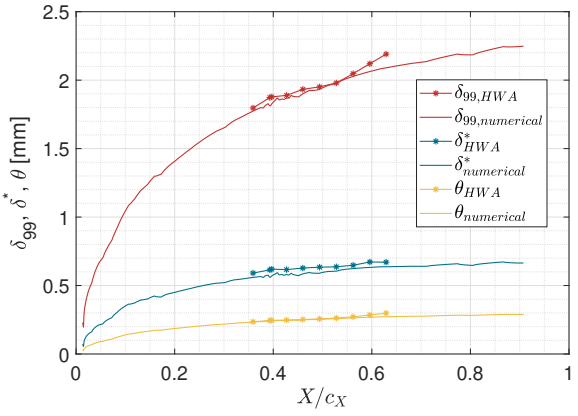

Figure 6.11: Boundary layer thicknesses estimated from hot-wire data compared with boundary layer solver

The mean velocity profiles from hot-wire data at three streamwise locations are compared with boundary layer solver in Figure 6.12. The velocities are non-dimensionalized with the external velocity and the profiles are plotted until δ_{99}. The profiles show a good comparison at the most upstream streamwise location and the hot-wire profiles show deviation from the numerically solved profiles at the most downstream one. The boundary layer solver solves for the baseflow without crossflow instability. However, the mean flow distortion due to crossflow is captured in hotwire measurements. Thus when spanwise averaging the velocity profiles, the mean flow distortion is reflected in the spanwise averaged profile.

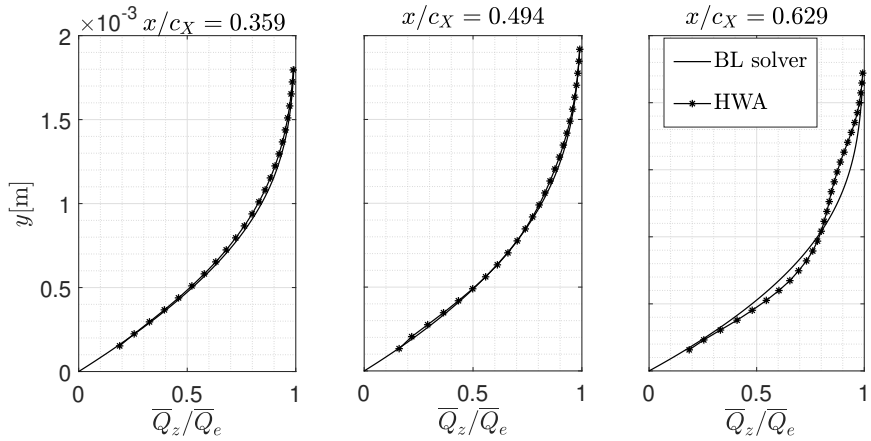

Figure 6.12: Nondimensionalized mean velocity profiles comparison with boundary layer solver

6.3.4. STATIONARY CROSSFLOW MODE SHAPE

The stationary crossflow mode shape $\langle \hat{q} \rangle_z$ as defined in subsection 4.2.3 nondimensionalized with the external time averaged velocity is presented in Figure 6.13 to study how the crossflow vortex progresses in the streamwise direction. From Figure 6.10a, the amplitude of the stationary crossflow mode (A) estimated by the maximum of the mode shape from Equation 4.10 and the integral of the mode shape from Equation 4.9, is found to consistently increase as we progress from one streamwise station to the next, indicating the monotonic growth of the crossflow vortices. Another important feature of the steady disturbance profile is the development of a bilobed structure. Downs and White [59] in their hot-wire studies on crossflow development reported the appearance of a second lobe in the stationary crossflow mode shape. This second lobe signals strong mean-flow distortion, which precedes amplitude saturation of crossflow vortices and the onset of secondary instability. From Figure 6.10a, it is seen that the crossflow vortices are not strong enough to reach saturation (which is found to happen when the amplitudes reach 25% of $\overline{Q}_e$). These weak crossflow vortices develop due to low initial amplitudes triggered by the 1 layer of DREs. However, it is still beneficial to characterize the spectral content in the clean configuration, such that it becomes easier to classify the spectral content in more complex step configurations. The investigation of secondary instabilities however calls for a power spectral density analysis, which is treated in the next section.

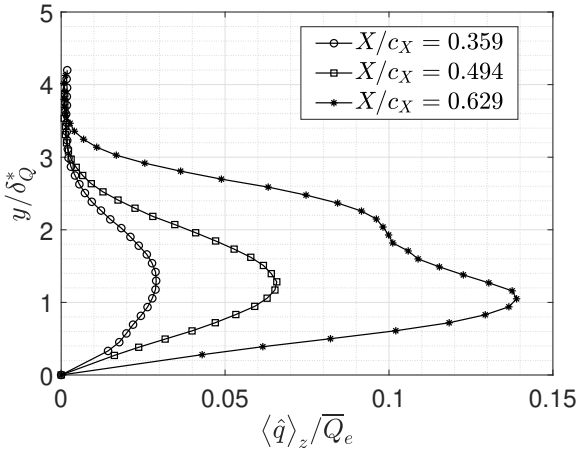

Figure 6.13: Stationary crossflow mode shape at three streamwise locations

6.3.5. CHARACTERIZATION OF UNSTEADY EFFECTS IN CLEAN CONFIGURATION

The frequency spectra of the clean forced case would help in identifying the sources of amplitude peaks that appear in the step cases. The spectra are obtained at selected locations within the crossflow vortex where it is known from the literature that secondary crossflow instability develops. As elaborated upon in subsection 3.1.4, the secondary instability modes are classified as Type 1,2, and 3 based on the spatial organisation of the velocity fluctuations within the boundary layer. The wall normal and spanwise gradients of velocity are presented to support the spectral anal-

ysis. Figure 6.14 shows the contours of the time averaged wall normal and spanwise velocity gradients with isolines of mean velocity. The gradients are studied at the first ($X/c_X = 0.359$), middle ($X/c_X = 0.494$) and last plane ($X/c_X = 0.629$) and the axes are non-dimensionalized as in Figure 6.9. The time-averaged velocity contour lines are superimposed to study the evolution of the vortices and their effect on the gradients. The locations of maximum (C) and minimum (B) of spanwise and maximum (A) of wall normal velocity gradients are identified to delineate the frequency bands corresponding to the secondary instability modes.

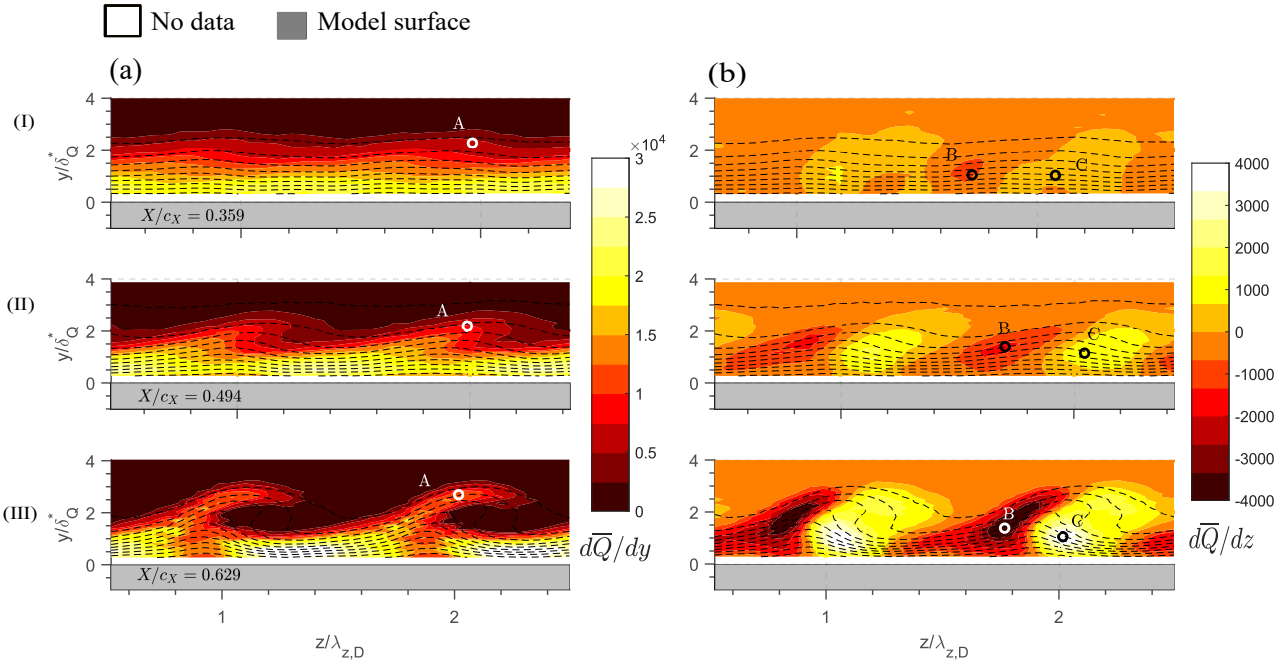

Figure 6.14: Contours of time averaged wall normal (left) and spanwise velocity gradients (right) with dashed isolines of mean velocity. Re_{c_X} = 1.08E+6

The spectra at three locations within the crossflow vortex and at a free stream location are illustrated in Figure 6.15. The increase in high frequency on band B_H in all streamwise locations is identified to be a hot-wire artefact. When experiments were conducted using different hot-wire anemometers in different laboratories [62], under all these different experimental conditions, the f^2 behaviour was present in all spectra. The identified source of this persistent phenomenon was the anemometers. The authors concluded that, at low turbulence levels,the performances of all hot-wire bridges at high frequencies were limited by this f^2 noise. To be able to identify the sources of the peaks in the power spectrum, bandpass filtered fields of temporal velocity fluctuations (nondimensionalized with external velocity $\overline{Q}_e$) are shown for the last plane under study ($X/c_X = 0.629$) in Figure 6.16. The bandpass filtered field in the frequency band $B_{L1} = 40 - 240Hz$ illustrates a contour Figure 6.16 a) which resembles the wall normal gradient contour in Figure 6.14. As detailed in [42], thin laminar boundary layers have high velocity gradients close to the wall. This is illustrated in Figure 6.12, where the spanwise and time averaged velocity $\overline{Q}_z$ reaches 80% of the external velocity $\overline{Q}_e$ within 1 mm. The frequency band associated with the bandpass filtered temporal fluctuations is linked to probe vibrations. This is equivalent to considering a fixed and a moving probe. For a probe traversing the wall normal direction, the wall normal gradient of the time averaged velocity would qualitatively align with a fixed probe measuring the velocity fluctuating in time at one location close to the wall. The frequency band for probe vibration is validated theoretically by considering the probe to be a simple beam cantilevered at one end. By beam theory, the natural frequency of the steel beam is calculated by [68] :

$$f_n = \frac{K_n}{2\pi}\sqrt{\frac{EIg}{wl^4}} \tag{6.2}$$

where n is the fundamental mode, Kn is the mode constant, E is the Young's modulus of steel, I is the area moment of inertia of the probe, w is the uniform loading due to the pressure, l is the length of the beam. The natural frequency is estimated to be 100.98 Hz, which lies in the frequency band estimated from the spectra.

The bandpass filtered field in the frequency band $B_{L2} = 240 - 310Hz$ presented in Figure 6.16 b), indicates the coherence in the location of the temporal velocity fluctuations with travelling crossflow. When travelling crossflow

interacts with the corrotating stationary crossflow vortex tubes (characterized by alternating high velocity and low velocity tubes), the travelling modes bring about fluctuations in the stationary modes. The fluctuations about higher velocity are relatively lower than that of fluctuations about a lower velocity. This becomes the reason why the inner side of the low momentum upwelling carries the Type 3 mode.

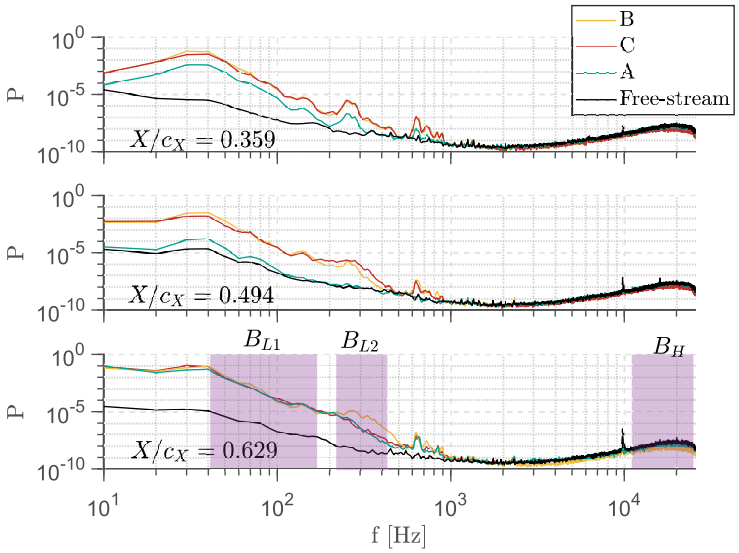

Figure 6.15: Power spectral densities of probe on different locations in crossflow vortex

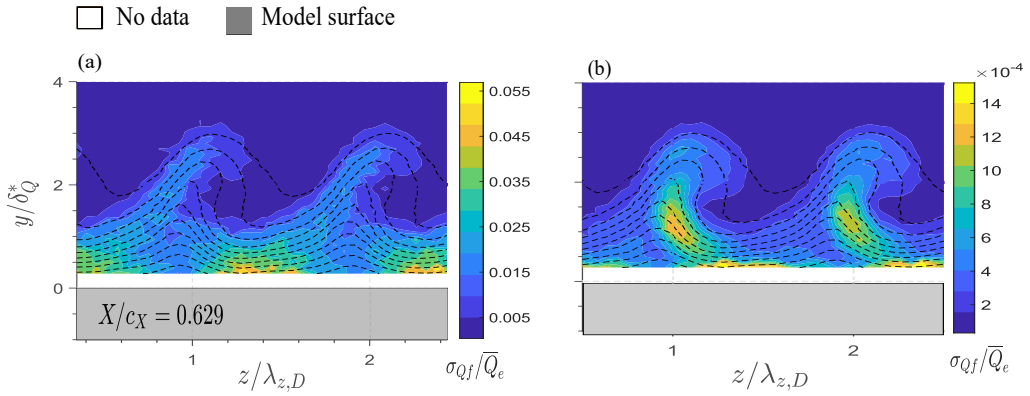

Figure 6.16: Bandpass filtered contours temporal velocity fluctuations (12 levels) at $X/c_X = 0.629$, with dashed isolines of mean velocity. $Re_{c_X} =$ 1.08E+6

7

CROSSFLOW INSTABILITY INTERACTION WITH STEPS

In the present chapter, the effect of initial crossflow amplitude on the interaction of crossflow vortices with steps is addressed. In this regard, the crossflow amplitudes at the step and chordwise locations are estimated. Based on the Tufts-Reed criterion, the critical step height is estimated and compared with the one observed experimentally. For different combination of step heights and initial amplitude of the crossflow vortices, the transition location is presented. Finally, the flow in the vicinity of the step for two initial crossflow amplitudes, for the clean, short FFS and supercritical FFS configurations is quantified through hot-wire anemometry.

7.1. INITIAL CROSSFLOW AMPLITUDES

In this section, a numerical/experimental method is described to determine the amplitude of the CF vortices at the step location $X/c_X = 0.397$ for different positions of the DREs. A linear stability analysis was performed using the in-house stability solver. The stability of the two dimensional boundary layer calculated from the external pressure distribution by solving the Orr-Sommerfeld equations (OS). The Orr-Sommerfeld equation was solved using the spatial formulation, where the angular frequency ω is real, and the stream-wise (α) and spanwise (β) wavenumbers are complex. The reader is referred to subsection 2.2.2 for a more elaborate description of linear stability analysis. The end result of the stability solver is the amplification N-factor curves of a given spanwise wavelength crossflow instability mode. From Equation 2.15 the ratio of the stationary crossflow amplitude (A/A_o) with respect to the amplitude at the location of the DREs is estimated.

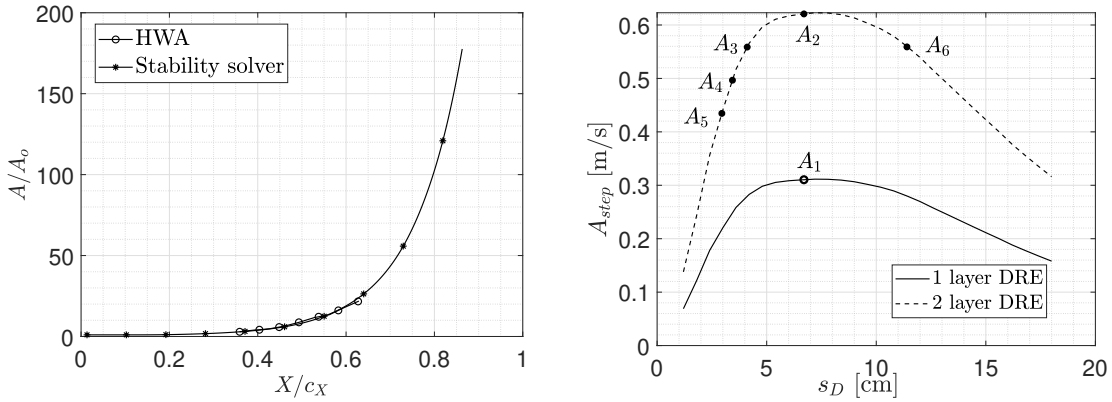

Figure 7.1: a)e^N curve fit to estimate A_o. Markers shown for every hundred points. b) Stationary crossflow amplitude at step location against DRE location in surface coordinates.

In order to find the stationary crossflow amplitude at the step location, one must first obtain the crossflow ampltidue at the first streamwise location A_o . The estimation of this parameter is done by least mean squares fit of the

trend of A/A_o from hot-wire on the trend from the stability solver. A_o was found to be 0.0870 m/s from the curve fit shown in Figure 7.1a . The stability solver was run once more but varying the chordwise location of the DREs and the effective N factor is calculated as the integral of the streamwise growth rates (α_i) from the DRE location. Deriving from Equation 2.14, we have:

$$N_{effective} = \int_{x_{DRE}}^{x} -\alpha_i dx \tag{7.1}$$

From the effective N factors, the crossflow amplitude at the step location is obtained by multiplying with A_o estimated from the curve fit. The stationary crossflow amplitude A associated with the DRE location (in surface coordinates in the direction orthogonal to the leading edge s) is plotted in Figure 7.1b. The curve corresponding two DRE layers is generated assuming that the amplitudes are twice the amplitudes associated with the one layer DREs predicted by the linear stability solver. This assumption is valid since linear theory still holds in the absence of steps. This assumption is confirmed in the upcoming section where the hot-wire results are documented in Figure 7.15b.

7.2. VORTEX CORE HEIGHT AT STEP

To be able to study the interaction of crossflow vortices with steps, it is desirable to have a rudimentary prediction of the critical step height. The purpose of this prediction is twofold: Firstly, to design and plan experiments and secondly to serve as a numerical validation of experimental observations. As reported in Rius-Vidales et al. [4], the term critical is assigned to the cases where the step has a noticeable effect on the transition location. An initial prediction of the critical step height comes from the vortex core height y_c at the step location as suggested by the Tufts-Reed criterion [48]. In this work, for the wavelength corresponding to the maximum amplification of the crossflow vortices (highest overall N factor, $\lambda_{Z,D} = 9$ mm) by linear stability theory, the vortex core height was taken to be the wall normal distance corresponding to approximately 97% of the maximum amplitude of the Y velocity perturbation profile [48].

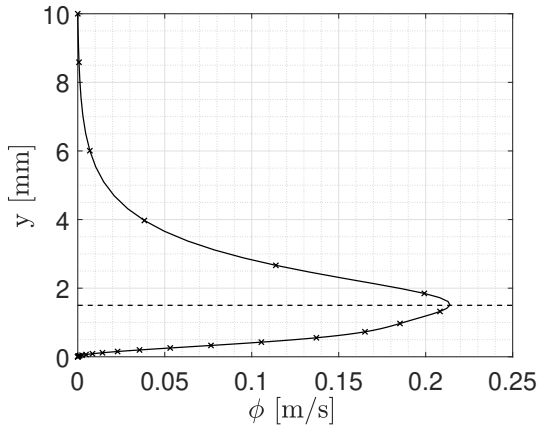

Figure 7.2: Eigenfunction profile for determination of vortex core height (only 1 in 50 samples is presented with a marker). Dashed line indicates the estimated vortex core height y_c. $\lambda_z = 9$ mm

To estimate the vortex core height, the eigenfunction is calculated from linear stability theory. y_c is estimated from the stability solver to be 1.5 mm, indicating that this is an estimate of the critical step height. The estimated y_c is in close accordance with Eppink's [40] recorded critical step height of 1.6 mm for the author's crossflow interaction studies on a 30^o swept flat plate. The eigenfunction velocity profile calculated from the stability solver is plotted in Figure 7.2, and y_c is demarcated in dashed lines at 1.5 mm.

7.3. IDENTIFICATION OF TRANSITION FRONT LOCATION

The transition location is a critical metric in boundary layer flow stability, which incorporates the effects of various parameters and instabilities in the boundary layer. A quick and visual indication of transition location is obtained through Infrared thermography. The reader is referred to subsection 4.1.1 for a more elaborate description of the technique.

In the present study, IR images are collected and post-processed to study the movement of the transition front with varying step heights and initial amplitudes of the CF vortices. To attain the estimated amplitudes A1-A6 at the step location shown in Figure 7.1b, 1 and 2 layers of DREs are positioned at different locations on the swept flat plate. The wind tunnel was set at a low Reynolds number $Re_{c_X,l}$ and a high Reynolds number $Re_{c_X,u}$ conditions to aid in extracting the location of the transition front through differential infrared thermography. The process of DIT is elaborated upon in subsection 4.2.5. The step heights were varied from the clean configuration up to a supercritical step height in steps of 0.1 mm. At this juncture, it is important to clarify the use of the terms critical and supercritical, which are found to vary in different works on the effects of steps on transition. In the present study, a critical step height is used when there is a noticeable change in the transition location when compared to the clean configuration. The term supercritical step height is used when the flow is found to 'trip' in the presence of the step, that is, when the transition front is found to appear at or very close to the step location (in agreement to the definition by Ruis-Vidales et. al [4]).

The spacing between the DREs and the diameter of the DREs was maintained a constant in this study. However, it has been shown from Rius-Vidales et al. [5], that the wavelength of crossflow vortices is a contributing factor in the interaction of the incoming crossflow with the FFS. For additional information on the same, the reader is referred to a summary of the work in Figure 3.2.2.

Case	A_{step}	x_D/c_x	$\lambda_{z,D}$ **[mm]**	d_D **[mm]**	k_D**[µm]**	$Re_{c_X,l}$	$Re_{c_X,u}$	**h [mm]**
F1	A1	0.11	9	2	100	1.08E+6	1.28E+6	0-1.3
F2	A2	0.11	9	2	200	1.08E+6	1.28E+6	0-0.9
F3	A3	0.068	9	2	200	1.08E+6	1.28E+6	0-0.9
F4	A4	0.057	9	2	200	1.08E+6	1.28E+6	0-0.9
F5	A5	0.049	9	2	200	1.08E+6	1.28E+6	0-0.9
F6	A6	0.19	9	2	200	1.08E+6	1.28E+6	0-1.1

Table 7.1: IR experimental matrix

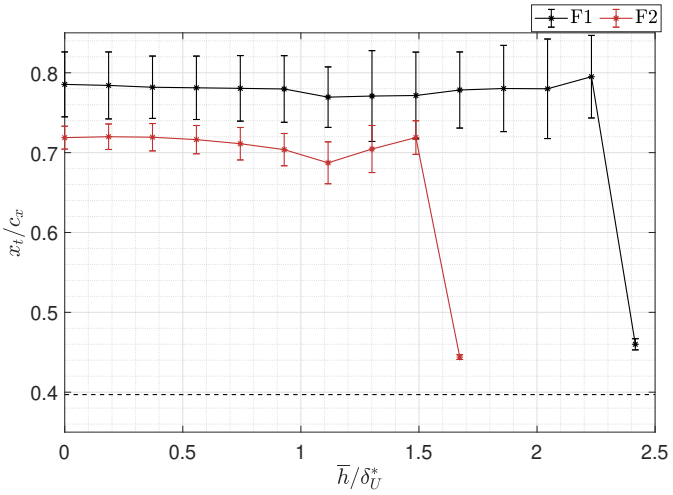

Figure 7.3: Transition locations at Re_{c_X} = 1.08E+6, keeping DRE location fixed and increasing DRE height (δ^*_U =0.538 mm). Dashed line indicates the location of the step.

Figure 7.3 presents the transition locations against step height for different initial amplitudes (cases F1 and F2). The error bars are confidence bands which indicate the minimum and maximum extent of laminar flow for each measured configuration. The confidence bands are found to be wider when the transition front shows turbulent wedges making demarcation of said transition front difficult. The step height is nondimensionalized by the displacement thickness at the step location estimated from the boundary layer solver. The displacement thickness δ^*_U is measured from the stream wise velocity component. The transition locations downstream of $x/c_x = 0.5$ are estimated from the dewarped images of camera IR-A (Figure 4.1) and the transition locations upstream of $x/c_x = 0.5$ are estimated from the dewarped images from camera IR-B. This is because close to the step dewarped images of IR-B are more reliable.

The location of transition for the clean configuration forced by one layer of DREs was identified to be $x_t/c_x = 0.78$, whereas the last plane of measurement in the HWA study presented in the previous chapter was $X/c_X = 0.629$. The significant difference between the planes explains why amplitude saturation and thus the development of secondary instability was not detectable on the results presented in chapter 6.

On comparing the cases where 1 and 2 layers of DREs were placed at the neutral point (F1 and F2), it is seen that the transition locations for the higher initial amplitude case appear upstream of the F1 configuration for all step heights. An abrupt transition advancement with respect to the clean configuration is seen at a supercritical step height of 0.9 mm ($\overline{h}/\delta^*_U$=1.6) for F2 configuration, while it's lower amplitude counterpart is found to trip at the step only at a step height of 1.3 mm ($\overline{h}/\delta^*_U$=2.4) . A marginal advancement in transition location towards the step is seen first at a step height of 0.6 mm ($\overline{h}/\delta^*_U$=1.1) for both the F1 and F2 cases which is treated cautiously. There is not enough evidence to treat this step height as critical since interestingly, there is seen to be a nonlinear trend post the step height for the F1 and F2 configuration until the supercritical step height is reached. So, henceforth the case is referred to as short FFS when indicating the marginal movement towards the step location.

Since there is an ambiguity in the presence of a critical step in the present study, the estimated y_c by linear stability theory from the previous section (1.5 mm) cannot be verified.

Moreover, as the step height increases an abrupt movement of transition front towards the step is observed for the supercritical step height. This is in agreement with the observations of Duncan et al. [21] and Eppink [38]. However the observations disagree with Rius-Vidales et al. [5] and [4], where the authors report a gradual movement of transition front with increasing step heights. Notwithstanding the nonlinearity in the trends, a key takeaway from this comparison is that an increase in DRE height, at a fixed chord location (neutral point), results in transition advancement. This can be attributed to the fact that an increased initial amplitude forcing associated with an increase in DRE height, advances the stages of growth, saturation, and breakdown of the crossflow instability. This result is found to be in agreement with the receptivity study of Zoppini et al. [20] where the authors investigated the effect of DRE heights and chord locations on transition on a 45^o swept wing without steps.

It is important to note that the confidence bands are also wider in the F1 case when compared to the F2 configuration. As the DRE size is smaller, the variations in size that exist between adjacent DRE elements is greater. Consequently, the crossflow vortices which develop from these DRE elements are unequal in size, and thus grow and breakdown at different chord locations. This forms a highly jagged transition front, which results in wider confidence bands.

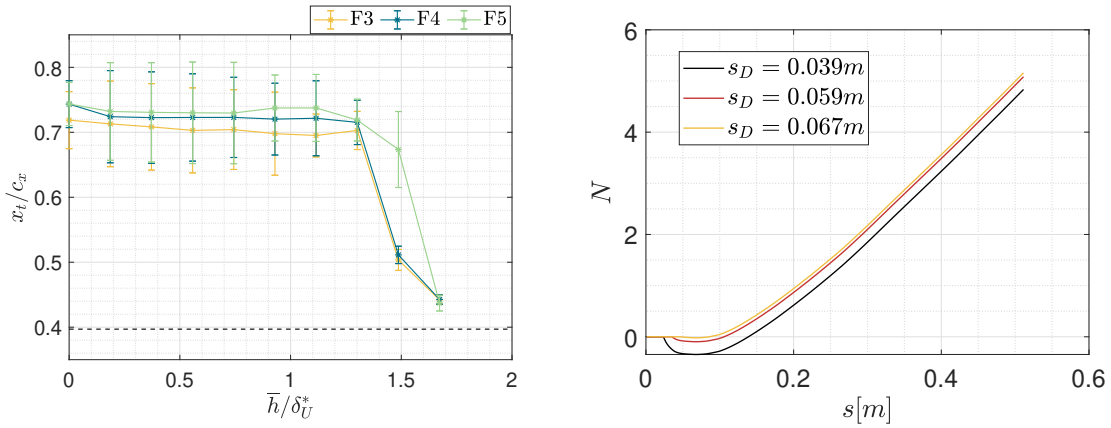

Figure 7.4: a)Transition locations at Re_{c_X} = 1.08E+6, keeping DRE height fixed, moving DRE array to chordwise locations upstream of neutral point (δ^*_U =0.538 mm). Dashed line indicates the location of the step. b) N factor trends for upstream movement of DREs

In the next set of trends shown in Figure 7.4a, the DRE is moved to chordwise positions upstream of the neutral point. On moving the DRE to upstream locations closer to the leading edge, keeping the DRE element height fixed, as was done for F3, F4 and F5 configurations, a downstream movement of transition location was observed for all step heights. This is in accordance with the work of Radeztsky et al. [58] on a 45° swept wing, where the authors observe a similar movement of the transition front. This can be attributed to an initial decay of crossflow vortices upto the neutral point. To support this argument, Figure 7.4b shows the growth rates for varying DRE locations upstream of the neutral point s_D = 0.067 m. Suppose an N factor corresponding to laminar flow breakdown is 2, the trend of the upstream DRE reaches this N factor at a more downstream location. Thus, the transition locations move

downstream. Here, it is interesting to note that the movement of the transition front towards the step is relatively gradual. The three trends indicate the presence of a critical step at $\overline{h}/\delta_U* = 1.5$.

Here again, it is important to note that the confidence bands grow wider as the DREs move more upstream. This is because as the DREs move upstream, the initial crossflow amplitudes are smaller, and in the presence of perturbations within the boundary layer, the variations between the neighboring crossflow amplitudes increases. This results in non-uniform breakdown of crossflow vortices along the span, causing once again, a jagged front and thus yielding a wider confidence band.

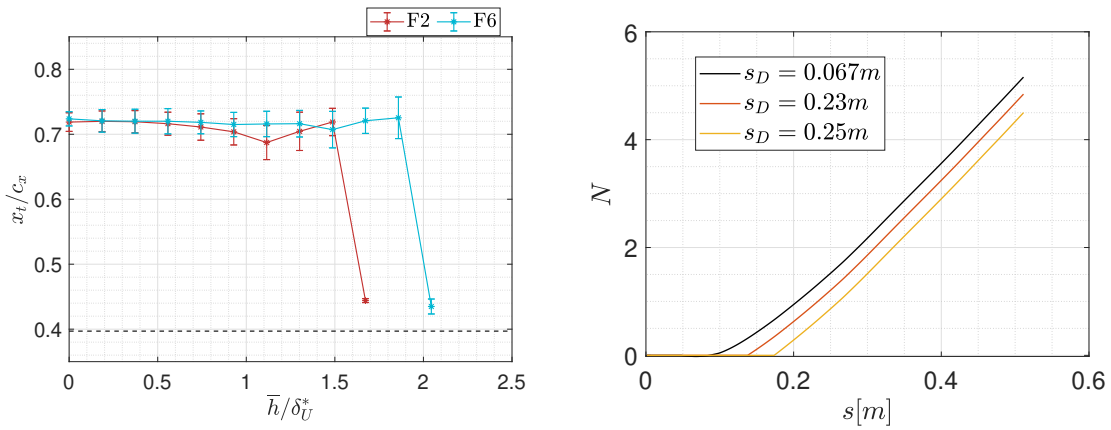

Figure 7.5: a)Transition locations at Re_{c_X} = 1.08E+6 keeping DRE height fixed, moving DRE array moving to chordwise location downstream of neutral point. (δ_U^* =0.538 mm). Dashed line indicates the location of the step. b) N factor trends for downstream movement of DREs

In Figure 7.5a, when maintaining the estimated amplitude at the step a constant (A3 and A6 in Figure 7.1b), when the DRE array was positioned downstream of the neutral point (case F6 in Table 7.1), the transition trend was observed to occur marginally downstream of the F2 trend. As the step height increases, the F2 case is associated with flow tripping at the step for a smaller step height as compared to the F6 case. The higher supercritical step height associated with F6 can be explained by the postponement in the location from where the onset of instability growth occurs. Figure 7.5b shows a similar trend of grow rates where the the growth rates are lower at a particular chordwise station when the DREs are moved downstream of the neutral point s_D = 0.067 m. Consequently, the eventual breakdown of the instability in this case is postponed. These results corroborate the results of Radeztsky et al. [58], where the authors observe a downstream movement of transition front when DREs were moved downstream of neutral stability point. Furthermore, it is observed that the supercritical step height associated with F6 lies between the supercritical step heights of F1 and F2. From Figure 7.5a, a similar nonlinearity in the trends is presented post the short FFS after which an abrupt transition movement towards the supercritical step is observed.

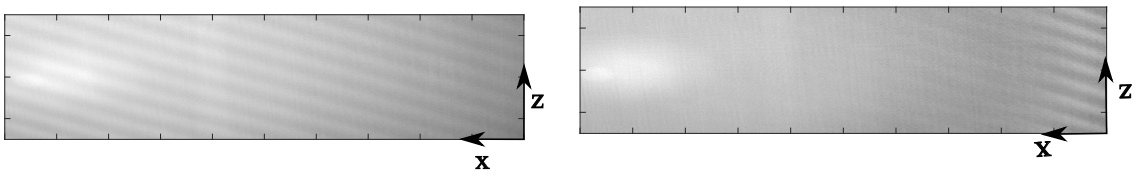

Figure 7.6: Zoomed IR images near step (right edge), a)Clean configuration (F2) b) Supercritical step height configuration (1 mm, F2)

Figure 7.6 presents, the zoomed images near the step captured from camera IR-B (refer Figure 4.1) which was aligned with the model fixed coordinate system. Positive z corresponds to movement from inboard to outboard and positive x indicates movement from upstream to downstream. The right edge of the image is the step. The flow imaged for the supercritical step height configuration in Figure 7.6b, shows the appearance of turbulent wedges at the location of the step. Shortly after the step, the flow is observed to be fully turbulent which is indicated by the darker expanse downstream. The clean configuration in Figure 7.6a shows alternating light and dark streaks which are approximately aligned with X (streamwise direction in wind tunnel fixed coordinate system) which are

characteristic of crossflow dominated boundary layers. The light and dark regions correspond to higher and lower temperature regions respectively. While the light streaks are associated with the region of low velocity found on the upwelling side of the crossflow vortex, the dark streaks are associated with the region of high velocity found on the downwelling side of the vortex. Since the crossflow is modulated by DREs spaced at $\lambda_{z,D}$, distance between any two light or dark streaks would be 9 mm. This is verified by plotting the temperature signal along the spanwise direction as shown in Figure 7.7. The distance between any two peaks is approximately 9 mm, thus implying that the DRE spacing appropriately modulates the spacing between the CF vortices. For a more robust validation and to identify the presence of other modes besides the forced one, spatial PSD could be employed.

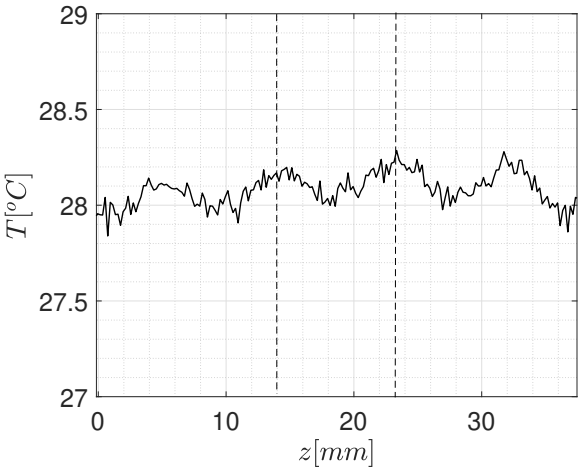

Figure 7.7: Temperature signal along the spanwise direction for the zoomed image at $Re_{c_X} = 1.081E+6$. Dashed lines demarcate the distance between two peaks which is estimated to be 9 mm

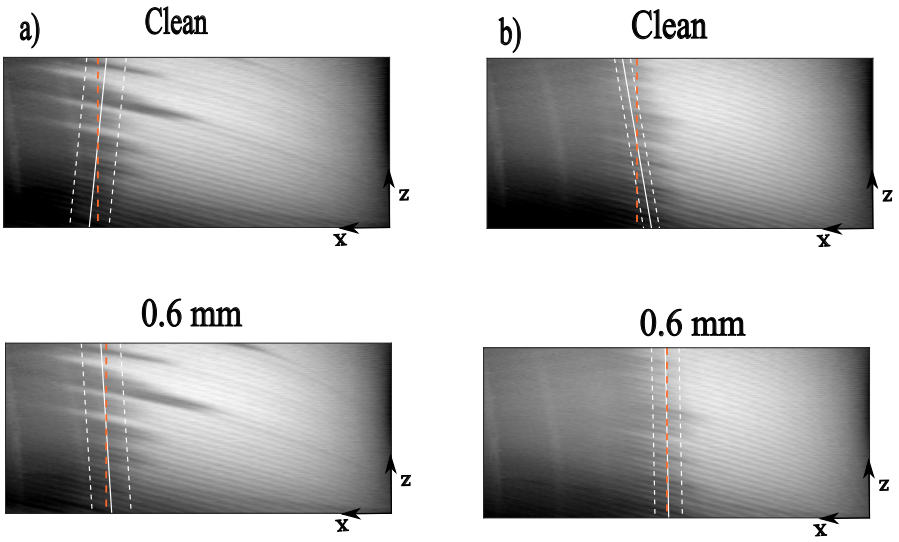

Figure 7.8: Full IR images indicating transition front identification with confidence bands for clean and short FFS associated with lower initial amplitude forcing a) F1 and b) F2 at $Re_{c_X} = 1.081E+6$

Figure 7.8 presents the full field view imaged from camera IR-A (refer Figure 4.1) for the clean and short FFS configurations for selected initial amplitudes. The dashed white lines indicate the confidence bands of the transition front. The solid white line indicates the transition front identified by the gradient of the binarized DIT image. The dashed orange line indicates the linear transition front generated from the midpoint of the domain. The images illustrate the characteristic zig-zag transition front which corresponds to the dominance of stationary crossflow instability on the swept plate [44] [23] [59]. While a travelling crossflow dominated flow is marked by the presence of a non-wedged time averaged transition front due to the sweep of CF vortices in the spanwise direction. The tran-

sition front is marked by turbulent wedges which are non-moving showing jagged pattern. The starting point of these wedges is described by Kohama et al. [75] as the locations where the stationary crossflow has produced highly inflected mean profiles. When comparing the thermal maps of F1 and F2, a consistent uniformity in the transition front ('clean front') is seen associated with the thicker DRE forcing. This can be explained because the difference between the thickness of micron sized roughness present in the flow (e.g., dust particles) and a two layered DRE element is higher than that of a one-layered DRE element. Thus, the fluctuations induced by such small particles in the flow would be relatively lower in the presence of a thicker DRE than in the presence of a thinner one. It could also be linked to the variations in size between adjacent DRE elements as mentioned previously. This leads to a visibly uniform transition front corroborating the smaller confidence bands shown in Figure 7.3.

On comparing the fronts of F1 and F2, There is a noticeable advancement in the transition front in the clean and short FFS configurations for the higher amplitude forcing corroborating the transition location trends presented in Figure 7.3. In order to better understand the flow leading up to the transition fronts, the quantification of the flow field close to the step will be treated in the coming section. The clean configuration, short FFS, and supercritical step height ($\overline{h}$ = 1.3 mm associated with the lower amplitude forcing) for F1 and F2 configurations of DREs will be treated in the next section.

7.4. CONVERGENCE TEST

For the preliminary characterization of the clean case, the hot-wire recorded data at each point in the measurement plane at a default sampling rate of 51 200 Hz for 2 s which resulted in the collection of 102400 samples. Since the time in the wind tunnel is limited, it becomes important to be efficient with the time consumed. Therefore, a convergence test was performed to check if the data converged to an acceptable degree with a smaller number of samples. The convergence error of temporal standard deviation of velocity is plotted against the number of samples in Figure 7.9 at two locations : one close to the wall (Figure 7.9a) and one in the freestream (Figure 7.9b).

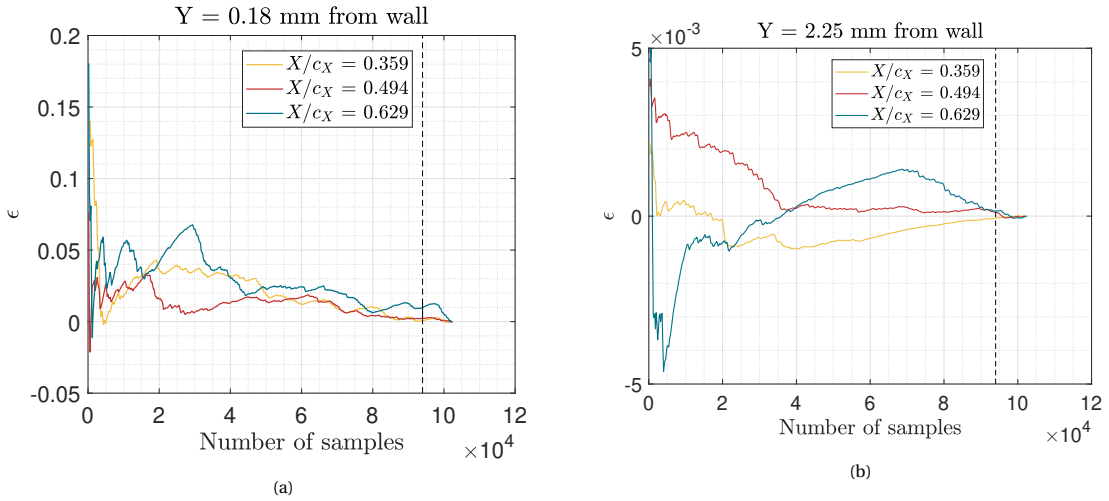

Figure 7.9: Convergence error of temporal standard deviation vs the number of samples a) y = 0.18 mm from wall ($\epsilon < 10^{-3}$) b) y = 2.25 mm from wall ($\epsilon < 10^{-4}$) . Dashed line indicates the minimum number of samples for a converged solution.

The convergence error is estimated by the difference between a fully converged solution and the solutions which have not reached full convergence. The parameter was found to be converged at 87040 samples (shown by the dashed lines in the figures).

$$\frac{87040}{51200} = 1.7\,\text{s} \tag{7.2}$$

This indicates that a measurement time of 1.7 s is sufficient to obtain converged velocities. The data presented in this chapter corresponds to a measurement time of 1.7 s. This resulted in a reduction of 19% in the total measurement time for each $y-z$ plane. This choice of measurement time strikes a balance between the windtunnel time and the convergence of solutions. This measurement time is employed for the hotwire measurements with steps which will be discussed in the upcoming section.

7.5. EFFECT OF INITIAL AMPLTITUDE OF CROSSFLOW VORTICES

From IR images, it is observed that the initial amplitude of crossflow vortices play a critical role in upstream and downstream shift of transition. The short FFS and supercritical step height have been identified from the movement of the transition fronts in the IR images on varying the initial amplitudes. It was identified that the flow tripped at the step, at a smaller step height when a higher initial amplitude was imposed. To further understanding of the flow close to the step, 1 and 2 layer DRE were placed at the neutral point (corresponding to A_1 and A_2 from Figure 7.1b) and hot-wire measurements were performed for the clean ($\overline{h}$ = 0 mm), short FFS ($\overline{h}$ = 0.6 mm) and supercritical step height ($\overline{h}$ = 1.3 mm). The hot-wire measurements were run for this study with the measurement time estimated from the previous section, and the specifics of the experiment are tabulated in Table 7.2. The reader is referred to Figure 4.1 for the measurement planes under study.

Case	DX [mm]	DY [mm]	Dz [mm]	nX	nY	nz	Measurement time [s]
F1	4.9	0.08	0.6	4	35	50	1.7
F2	4.9	0.08	0.6	4	35	50	1.7

Table 7.2: HWA experimental matrix

7.5.1. INFLUENCE OF FFS ON MEAN FLOW

To illustrate the effect that the step has on the mean flow, Figure 7.10a presents the span-wise averaged boundary layer velocity profiles $\overline{Q}_z$ nondimensionalized with the span-wise averaged external velocity $\overline{Q}_e$. A deceleration in the flow is observed in the step configurations when comparing with the clean case just before the step and at the step location ($X/c_X = 0.385$, $X/c_X = 0.397$). This deceleration upstream of the step corresponds with the adverse pressure gradient seen in Figure 7.10b. The velocity profiles associated with the step configurations show an acceleration in the flow soon after the step ($X/c_X = 0.402$). This flow acceleration is in accordance with the abrupt favorable pressure gradient observed in Figure 7.10b. The 0.6 mm FFS profile at the last measured streamwise station ($X/c_X = 0.408$) is found to decelerate its flow speed to the clean configuration, indicating that a second adverse pressure acts to recover the flow to the external pressure distribution. This adverse-favorable-adverse pressure gradient signature is in accordance with the experimental and computational studies surveyed [48], [21], [4], [29].

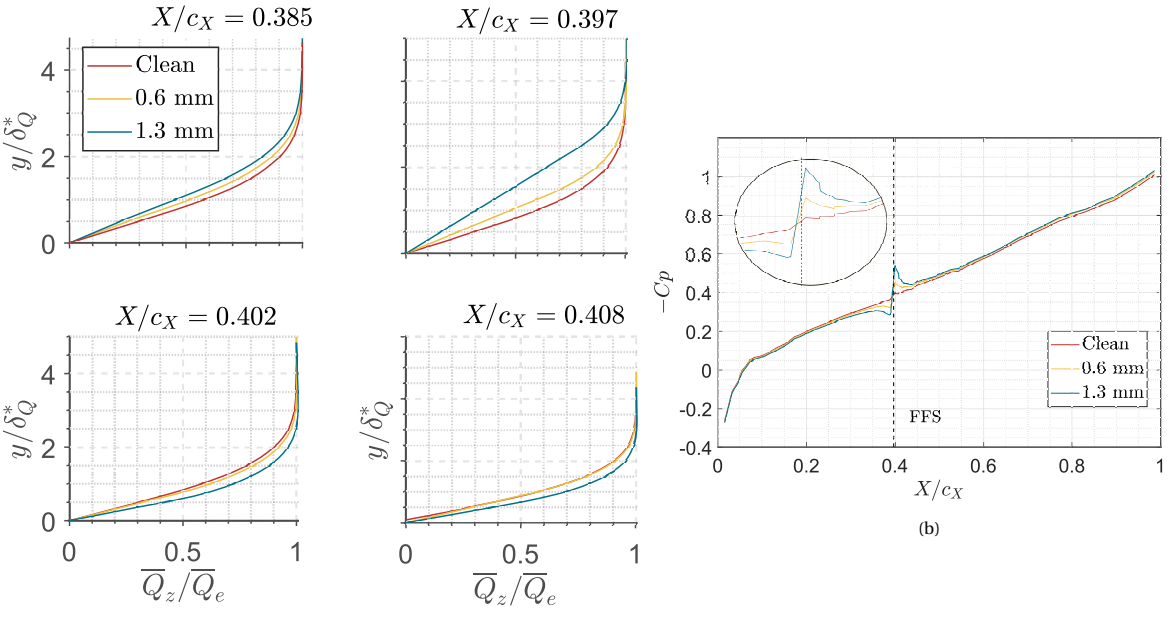

Figure 7.10: a) Boundary layer profiles for measured step heights (F1) b) Pressure gradient signature for the same step heights (only the outboard taps are plotted for clarity) (F1). Dashed line indicates the location of the step. Shown zoomed pressure gradient close to step.

The recirculation regions before the step and on the step as reported by the numerical investigations of Tufts [48], could also be used to explain the origin of the pressure gradient signature. As the flow meets the step, the step becomes a stagnation line and the static pressure increases, thus creating an adverse pressure gradient in that region.

The streamlines that pass over the first recirculation region, accelerate at the step location and a sharp favorable pressure gradient is presented. Finally, as the flow climbs down from the second recirculation region, the flow decelerates and an adverse pressure gradient results. Post the recirculation region, the pressure recovers to the imposed favorable pressure gradient.

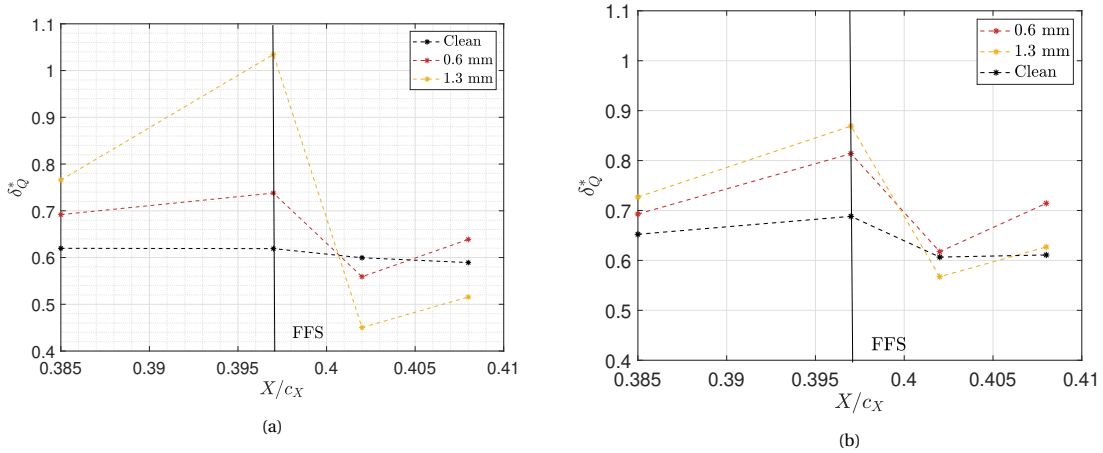

Figure 7.11: Displacement thickness for clean, short FFS (0.6 mm) and supercritical (1.3 mm) step height configurations a) F1 b) F2

The displacement thicknesses estimated from the resultant velocity Q for F1 and F2 are presented in Figure 7.11. As the flow climbs over the step, the boundary layer thickness increases as there is a sharp increase in the vertical velocity component v as reported by Rius-Vidales et al. [4] and Eppink [39]. It is seen that the thickness trends shows a steeper slope before the step for higher step heights. This corroborates the results of Rius-Vidales et.al [4] and Eppink [39], where they observe the v component increase is higher for higher step heights. Also, it is observed that there is an abrupt reduction in the boundary layer thicknesses after the step. The amount of thickness reduction increases as the step height increases. This can be accounted for by the acceleration of the flow over the recirculation region. Consequently by Equation 2.3, the boundary layer becomes thinner. These thickness trends corroborate the pressure gradient signature presented in Figure 7.10b. It is important to note that the thicknesses for the supercritical step height are greater for the lower amplitude forcing in Figure 7.11a when compared to the higher amplitude forcing in Figure 7.11b. This could be explained by the definition of displacement thickness. Since the higher amplitude forcing is associated with greater base flow modulation and thus a stronger upwelling and downwelling momentum transfer. So, spanwise averaging the time-averaged field yields a smaller velocity deficit region. Therefore, it is associated with a smaller displacement thickness at the step.

It is also seen that the thicknesses for the supercritical step height cases decrease to values lower than the clean configuration post step. This increase in step height could thus affect the stability of the flow as reported by Eppink [39] and Tufts et al.[48], wherein smaller wavelength disturbances could be amplified.

The mean velocity contours nondimensionalized with the external velocity are presented for the DRE 1 layer (F1) case in Figure 7.12. The wall normal axis (y) is nondimensionalized with the displacement thickness of the most upstream plane in the clean configuration (δ^*_Q= 0.6198 mm for F1 and δ^*_Q = 0.6523 mm for F2) calculated with the resultant velocity measured by the hotwire (Q) from Equation 2.2, and spanwise axis (z) with the wavelength of the initial crossflow vortices ($\lambda_{z,D}$ spacing between the DREs). An integral number of crossflow vortices (two) is visualized and studied, as spanwise averaging the fields would then be comparable across varying conditions and locations. The contours show high velocity gradient (indicated by the closely packed contour levels) near the wall for the step configurations at the step plane. This is attributed to the increase in the wall normal velocity component, pushing the flow up the step. The presence of this vertical velocity component was reported in Eppink [40] (Figure 4b), Rius-Vidales et al. [4] (Figure 7 II).

Along any wall normal line, it is seen that the stationary crossflow vortices show a high velocity and low velocity region. This is in accordance with the streaks of high and low velocity found in the thermal maps presented in Figure 7.6. On progressing downstream , in the clean configuration (I-IV a), the stationary vortices show only minor growth and movement in the spanwise direction. This is due to the fact that the measurement planes are in close proximity to the step plane (X/c_X = 0.397). The boundary layer becomes thinner when moving from the clean configuration to the step configuration (II a - c) which corresponds well with the spanwise averaged velocity profiles illustrated in Figure 7.10a. As we move downstream in short FFS configuration (I-IV b), the crossflow vortices are

shown to lose spanwise coherence. This is also evident in the supercritical step height configuration (IV c), wherein the vortices are shown to lose spanwise coherence as laminar turbulent boundary layer transition occurs, and flow mixing prevails indicating the onset of turbulence. However, it is known from the transition locations presented in Figure 7.3 that the transition front appears downstream of the last plane of investigation at $x_t/c_x = 0.44$. The spectral content will be studied in subsection 7.5.3.

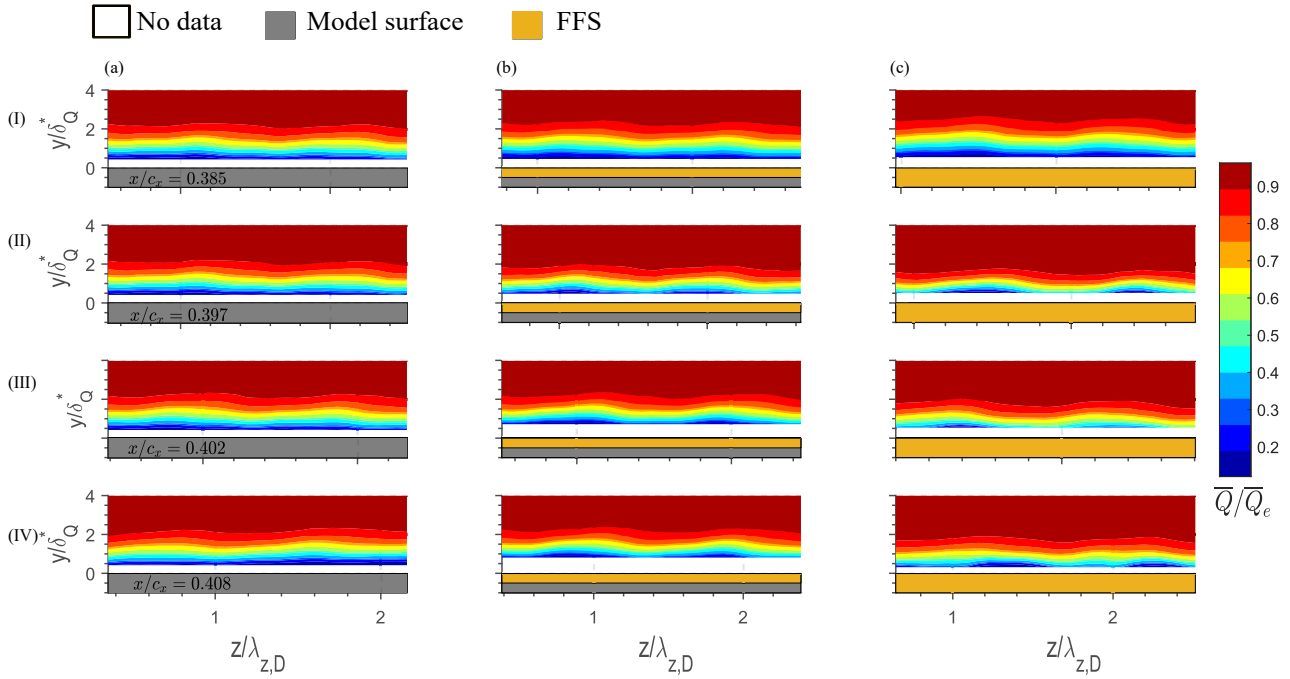

Figure 7.12: Time averaged mean velocity contour (12 levels) for the lower initial amplitude forcing (F1) a)Clean configuration b) $\overline{h}$ = 0.6 mm c) $\overline{h}$ = 1.3 mm, Re_{c_X} = 1.08E+6

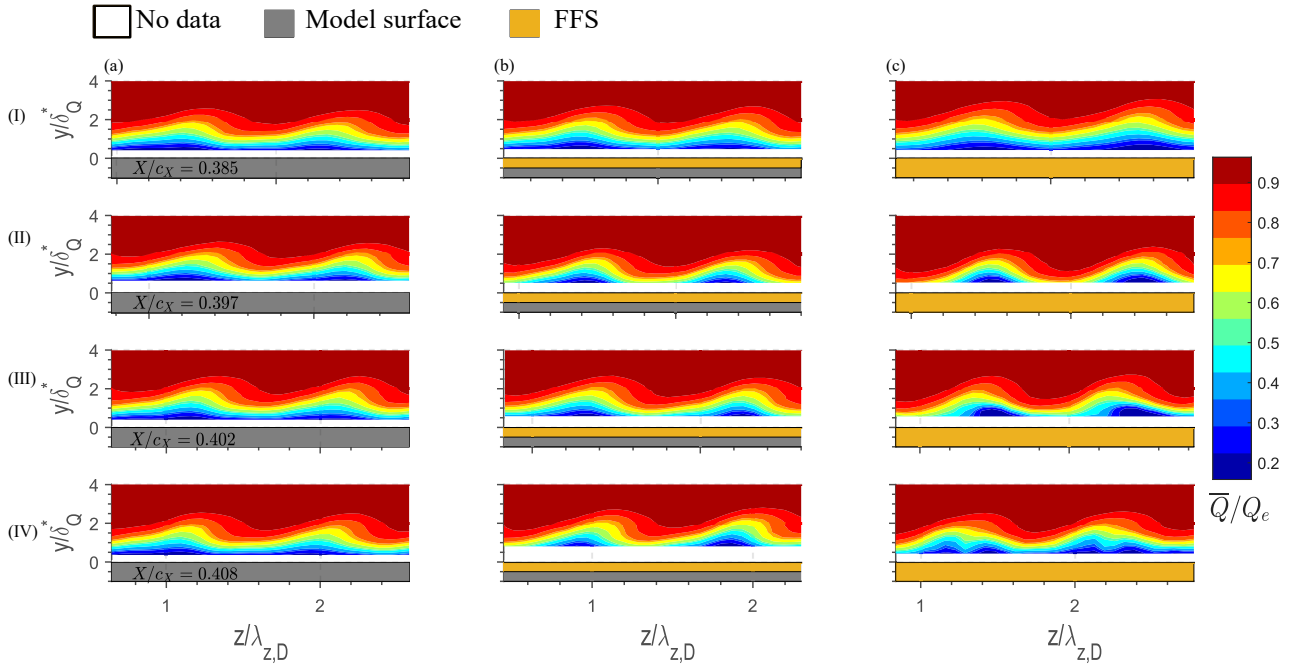

Figure 7.13: Time averaged mean velocity contour (12 levels) for the higher initial amplitude forcing (F2) a)Clean configuration b)$\overline{h}$ = 0.6 mm c) $\overline{h}$ = 1.3 mm, Re_{c_X} = 1.08E+6

The mean velocity contours are presented for the higher initial crossflow amplitude in Figure 7.13 . The higher

initial amplitude forcing produces a more prominent pattern where the crossflow vortices are found to be arranged in the spanwise direction at $\lambda_{z,D}$ =9 mm apart when compared with the DRE 1 layer configuration. On studying the highest step height case (I-IV c), loss of coherence in the stationary crossflow vortex structure is shown. The strong mean flow distortion is indicative of the onset of secondary instabilities and the breakdown of the CF vortices to turbulence.

7.5.2. INFLUENCE OF FFS ON STATIONARY CROSSFLOW

Steady disturbance profiles nondimensionalized with the external velocity are presented at the measured streamwise locations in Figure 7.14a. The stationary crossflow amplitude calculated from Equation 4.11 is nondimensionalized by the external velocity and presented for the three step heights for the F1 case in Figure 7.14b. It is seen from the disturbance profiles that the maximum does not monotonically increase, for instance there is a marginal decrease in the maximum from X/c_X = 0.385 to X/c_X = 0.397 for the short FFS ($\overline{h}$ = 0.6 mm) profile. This could be attributed to the influence of amplification of other modes besides the mode conditioned by DREs.

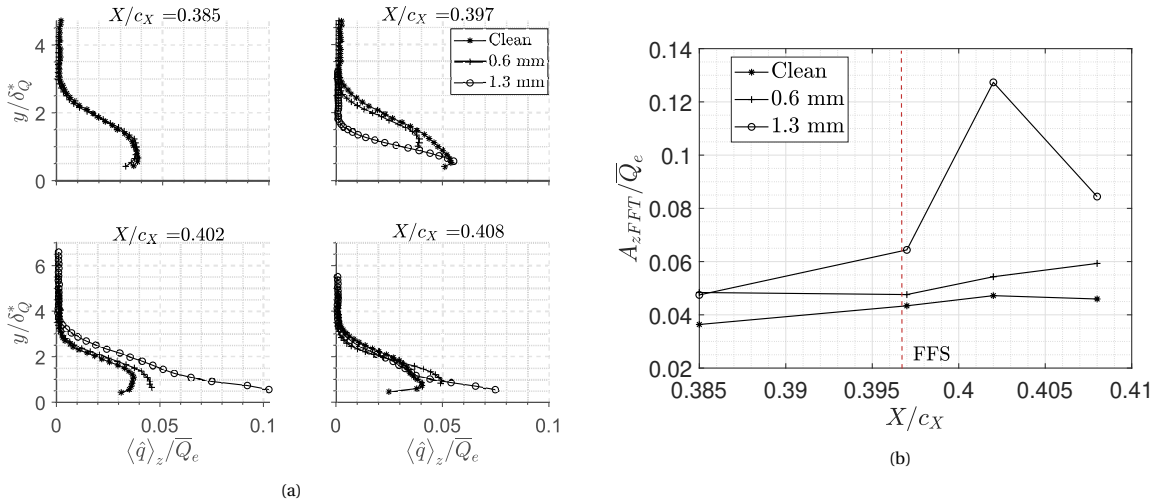

(a) (b)

Figure 7.14: a) Steady disturbance profiles b) Stationary crossflow amplitudes estimated from spatial FFT (F1) for Clean, $\overline{h}$ = 0.6 mm step and $\overline{h}$ = 1.3 mm step at four chordwise stations . Dashed line indicates location of FFS.

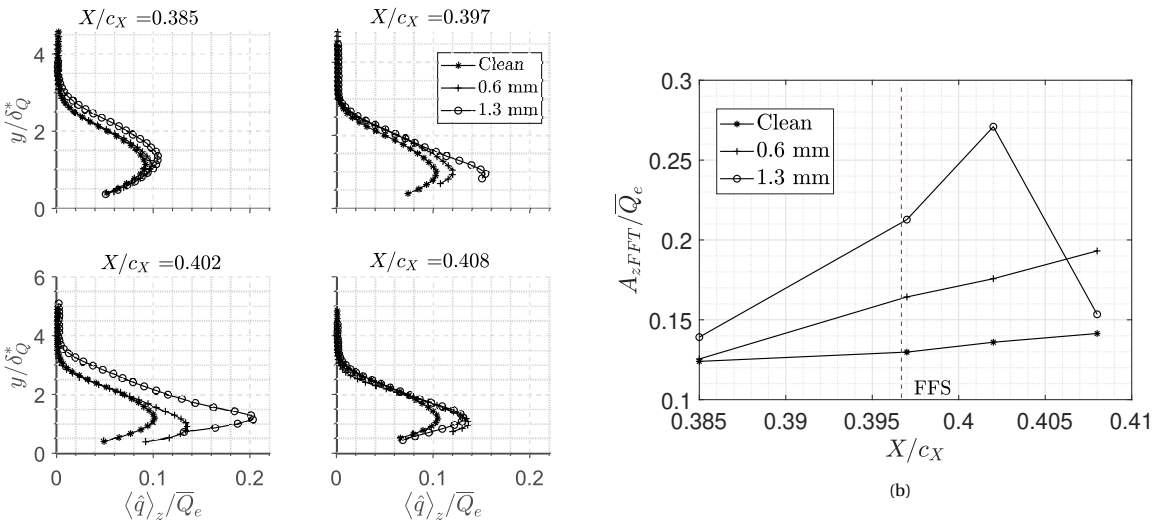

(a) (b)

Figure 7.15: a) Steady disturbance profiles b) Stationary crossflow amplitudes estimated from spatial FFT (F2). for Clean, $\overline{h}$ = 0.6 mm step and $\overline{h}$ = 1.3 mm step at four chordwise stations . Dashed line indicates location of FFS.

From Figure 7.11a, the displacement thickness is found to decrease soon after the step, causing a thinner boundary layer to develop. As mentioned in Tufts et al. [48], a thinner boundary layer can give rise to smaller wavelength disturbances being amplified. In order to identify the conditioned amplitude unadulterated by the influence of other amplified modes in the flow, a spatial fast fourier transform is performed as in Equation 4.11 to generate the stationary crossflow amplitude trend presented in Figure 7.14b. It should be noted that since the crossflow vortices are weak as discussed in section 6.3, the amplitudes are not greater than 12% of the external velocity. It is seen that an abrupt amplitude amplification and decay occurs for the highest step height configuration downstream of the step $X/c_X = 0.402$ unaccompanied by the presence of a bilobed mode shape. This amplitude decay for the highest FFS correlates well with the loss in coherence observed in the mean flow contour.

Nondimensionalized mode shapes and stationary crossflow amplitudes are presented for F2 in Figure 7.15. The stationary crossflow amplitudes seen for the higher initial amplitude forcing (F2) are significantly higher compared to F1, reaching upto 27% of the external velocity. This is comparable to the typical saturation amplitudes reported for various 45^o swept models by Downs and White [59] (Figure 19). Furthermore, the amplitudes at the step location $X/c_X = 0.397$ in the clean configuration presented for F2 are found to reach around twice the amplitudes presented for F1. This validates the assumption employed behind generating Figure 7.1b. The amplitude trends of the clean and the 0.6 mm step height show a monotonic growth. For the highest step height case, the sharp amplitude decay presents itself at the same stream-wise station as for F1. This abrupt drop coincides with the reduction in the maximum of the mode shape from $X/c_X = 0.402$ to $X/c_X = 0.408$. Once again the amplitude decay corresponds with the onset of laminar flow breakdown and the consequent loss in span-wise coherence in the modulated boundary layer for the highest FFS as seen in Figure 7.13.

The growth and decay of stationary crossflow amplitude seen in F1 and F2 for the highest FFS configuration corresponds well to the initial region of growth documented by Eppink [39] and Eppink et al. [41]. The studies observe two regions of growth wherein the first is hypothesized to be attributed to strong inflectional profiles triggered by the adverse pressure gradients near the step. The adverse pressure gradient seen soon after the step Figure 7.10b is a precursor for crossflow reversal and a recirculation region.

The second region of growth in the flow recovery region was deduced to be generated by nonlinear effects due to the modulation of the recirculation region downstream of the forward facing step. Since for the current study, the measurements were restricted to a region in the vicinity of the step, the second region of growth for the smaller step height $\overline{h} = 0.6$ mm could not be validated.

7.5.3. INFLUENCE OF FFS ON UNSTEADY FLOW

Figure 7.16 presents the contours of spanwise gradient of the temporally averaged velocity ($\partial\overline{Q}/\partial z$) at all the measured streamwise stations (I - IV). for F1 configuration. The black dashed lines demarcate the isolines of mean velocity. The plot features alternating negative and positive spanwise gradients of mean velocity. It is observed that a negative spanwise gradient aligns with the outer (left) side of the crossflow vortices and a positive spanwise gradient aligns with the inner side of the vortices for the clean as well as the step configurations. The observations in the present study are in agreement with the work of Eppink (Figure 6c in [37]). The plane presented by the author is 5 mm downstream of a supercritical step (equivalent to III c). The study also presents the alignment of the negative spanwise gradient with the outer side of the crossflow vortices. A region of high spanwise shear is seen in the last plane of the supercritical step IV c. This region is also evident in the higher initial amplitude forcing configuration and will be studied upon in detail.

The contours of spanwise gradient of the mean velocity for 2 layers of DRE configuration (F2) is presented in Figure 7.17. The contour for the highest step height at the last measured plane (IVc) shows a loss in the alternating pattern of positive and negative gradient. This correlates with the breakdown of CF vortices observed in Figure 7.13. In addition, the observations for Figure 7.16 are found to be pertinent to the 2 layer configuration, wherein the negative gradients are aligned with the outer side of the vortex and vice versa. Minor near wall regions of high spanwise shear are seen to appear in the short FFS configuration configuration post the step IIIb, and also in the supercritical step height configuration at the step IIc. The negative spanwise shear for the supercritical step, is observed to increase in amplitude near the wall along the streamwise direction. Most importantly however is the region of high spanwise shear identified in III c (region R). This region will be discussed about in more detail in the coming sections. As discussed in subsection 3.1.4, contours of spanwise gradient of the mean velocity are required to identify the locations to probe for the analysis of the spectral content within the boundary layer. As discussed above, the identification of the type I and III modes is aided by the presence of probes at the minimum and maximum of the spanwise gradient, located on the same crossflow vortex (demarcated as B and C in Figure 7.16 and Figure 7.17 respectively).

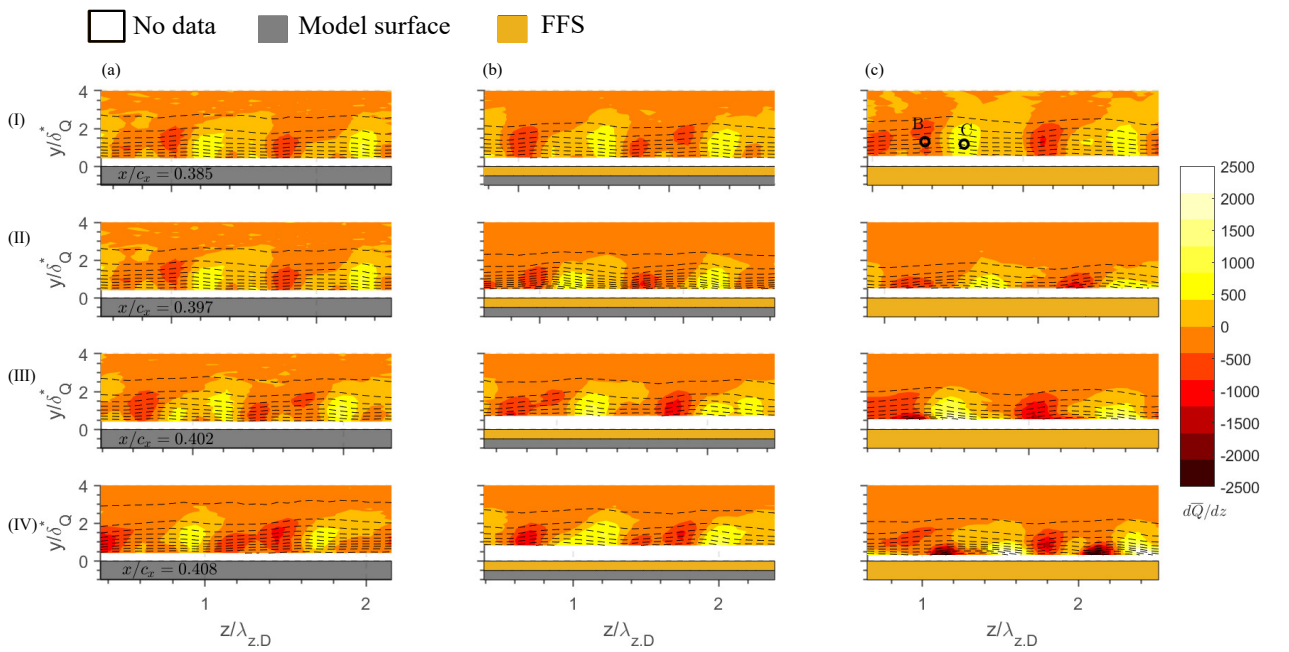

Figure 7.16: Contours of spanwise gradients of time averaged velocity (12 levels), with dashed lines of iso-velocity - F1. a) Clean configuration b) $\overline{h}$ = 0.6 mm c) $\overline{h}$ = 1.3 mm, Re_{c_X} = 1.08E+6

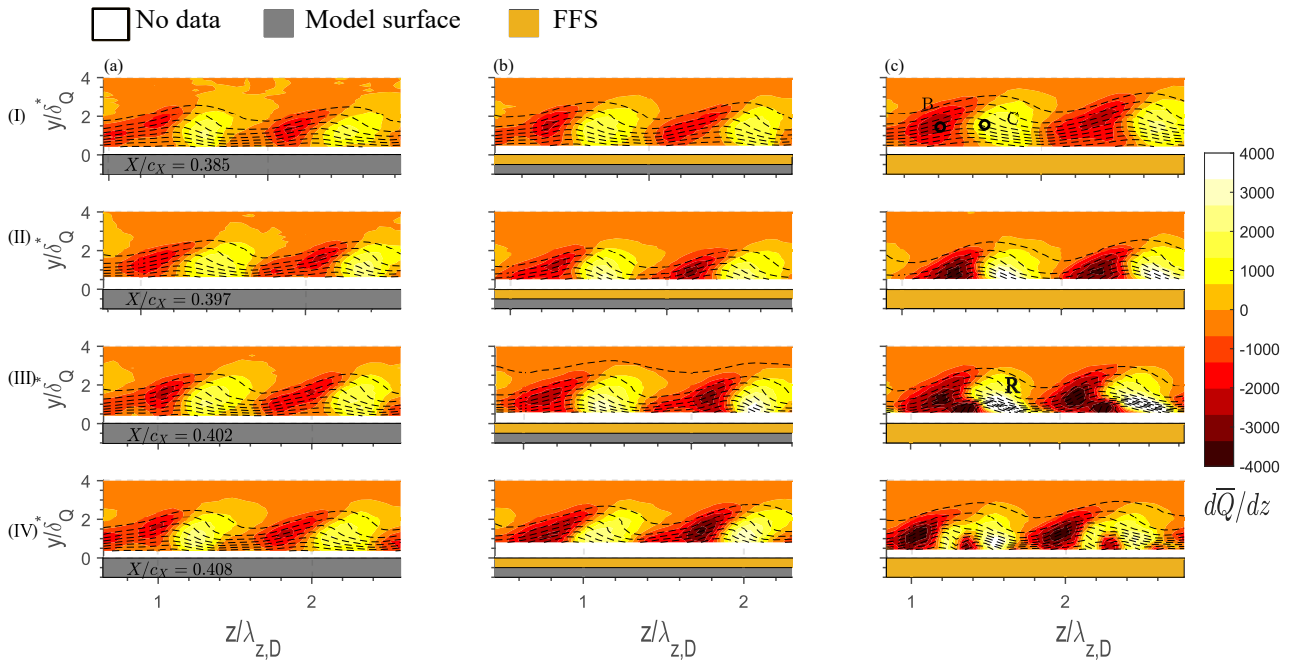

Figure 7.17: Contours of spanwise gradients of time averaged velocity (12 levels), with dashed lines of iso-velocity-F2. a)Clean configuration b) $\overline{h}$ = 0.6 mm c) $\overline{h}$ = 1.3 mm, Re_{c_X} = 1.08E+6

The contours of wall normal gradient of the temporally averaged velocity ($d\overline{Q}/dy$) are illustrated for the DRE 1 layer in Figure 7.18. A consistent observation for the clean and the step configurations is the presence of positive wall normal gradients near the wall. These results are found to be in agreement with the contours of Eppink [37] (Figure 6d). The presence of high gradients arising at the locations where they do for the supercritical configurations downstream of the step (III-IV c) show similarity to the work of Eppink [37] and Rius-Vidales et al. [6], wherein the author also presents the results for a supercritical step height of 1.7 mm. These structures appear with more definition in the case with higher amplitude forcing (F2).

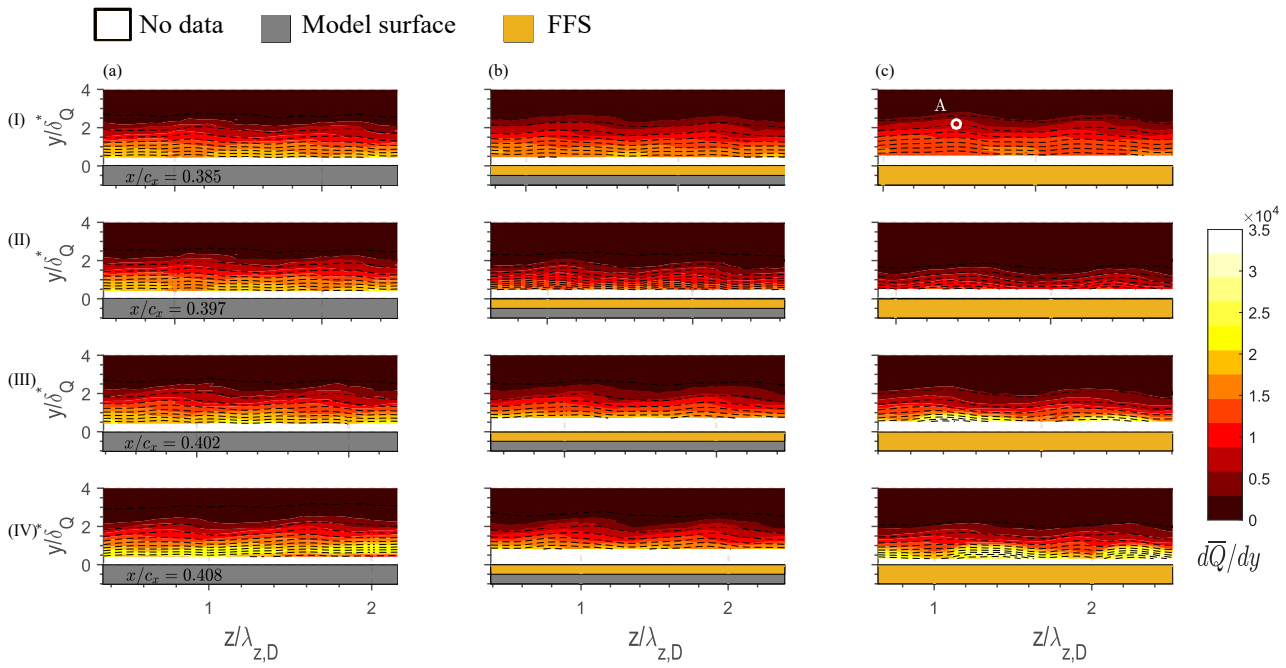

Figure 7.18: Contours of wall normal gradients of time averaged velocity (12 levels), with dashed isolines of mean velocity - F1. a)Clean configuration b) $\overline{h}$ = 0.6 mm c) $\overline{h}$ = 1.3 mm, Re_{c_X} = 1.08E+6

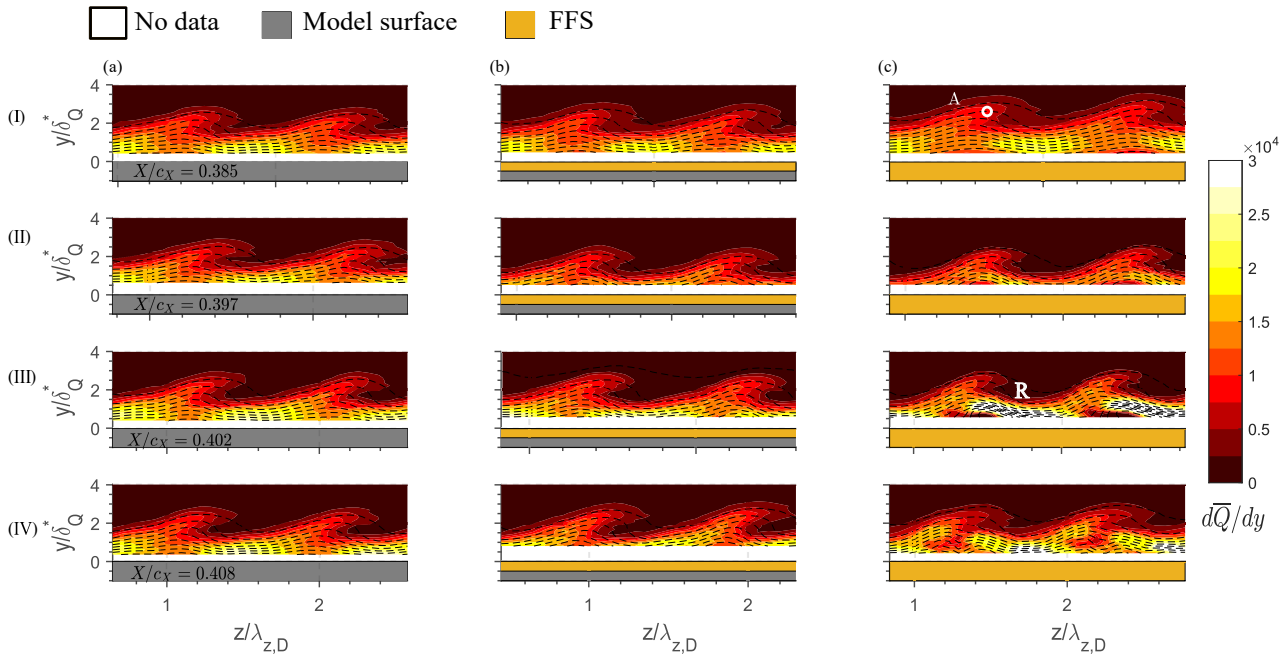

Figure 7.19: Contours of wall normal gradients of time averaged velocity (12 levels), with dashed isolines of mean velocity - F2. a) Clean configuration b) $\overline{h}$ = 0.6 mm c) $\overline{h}$ = 1.3 mm, Re_{c_X} = 1.08E+6

The contours of wall normal gradient of mean velocity are presented for the higher amplitude forcing in Figure 7.19. When the flow interacts with the supercritical step configurations downstream of the step (III-IV c), the contours show high wall normal gradients arising from the wall and extending to the inner side of the upwelling (region R in III c)). This feature, present in similar positions on the vortex structure was also seen by Eppink [37] and Rius-Vidales et al.[6]. The author reports the presence of the high gradients to the shear layer development above the flow recirculation region downstream of the FFS. The work of Eppink [37] [39] showed that the recirculation region present downstream of the FFS was not continuous in the spanwise direction but instead formed isolated flow reversal regions developing into streamwise vortices. Since in the present study, a single wire HWA probe can only

measure the resultant velocity magnitude and not direction, it is not possible to definitively demarcate the recirculation regions as proposed by Eppink [37] [39]. However, the presence of similar features on the wall normal gradient contours points to the evolution of similar flow structures downstream of the step. A similar organisation of wall normal gradient was seen by Rius-Vidales et al. [6] for a supercitical step (Figure 7 IId). Finally, a probe is located at the top of the crossflow vortex (an example demarcated as A in Figure 7.18 and Figure 7.19) to detect the presence of the Type II secondary instability mode. The reader is referred to subsection 3.1.4 for the origin of Type II mode. The spectral content at the probed locations (A,B,C) would help in the identification and comparison of the unsteady features presenting itself in the flow interacting with the short FFS and supercritical step. The spectra for the clean configuration help demarcate the bands not linked to secondary instabilities.

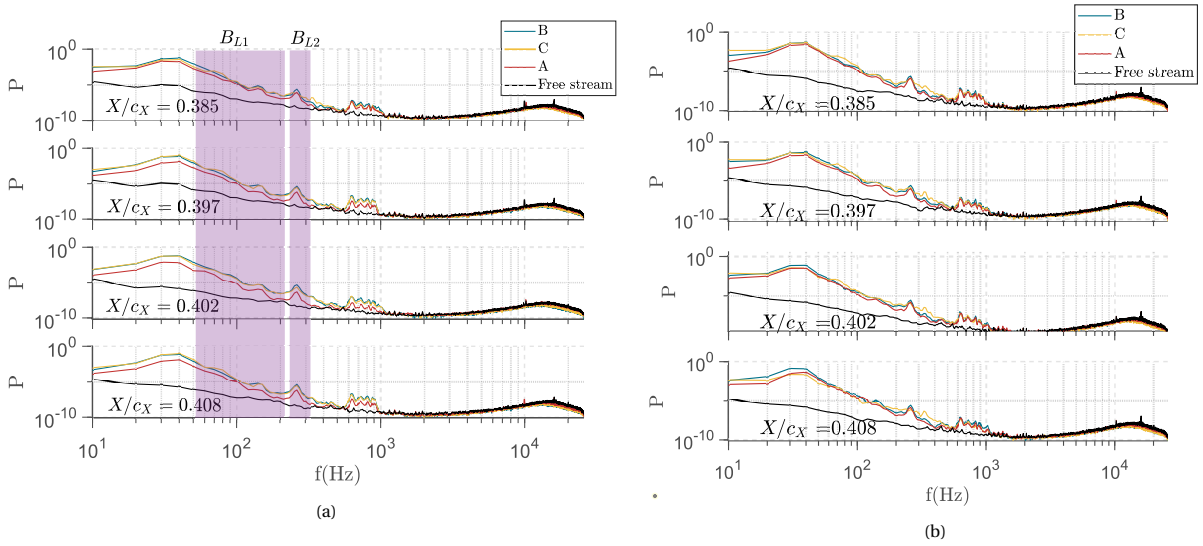

Figure 7.20: Spectral analysis for the probes at A,B C and freestream for the clean configuration associated with a) lower amplitude forcing (F1) and b) higher amplitude forcing (F2)

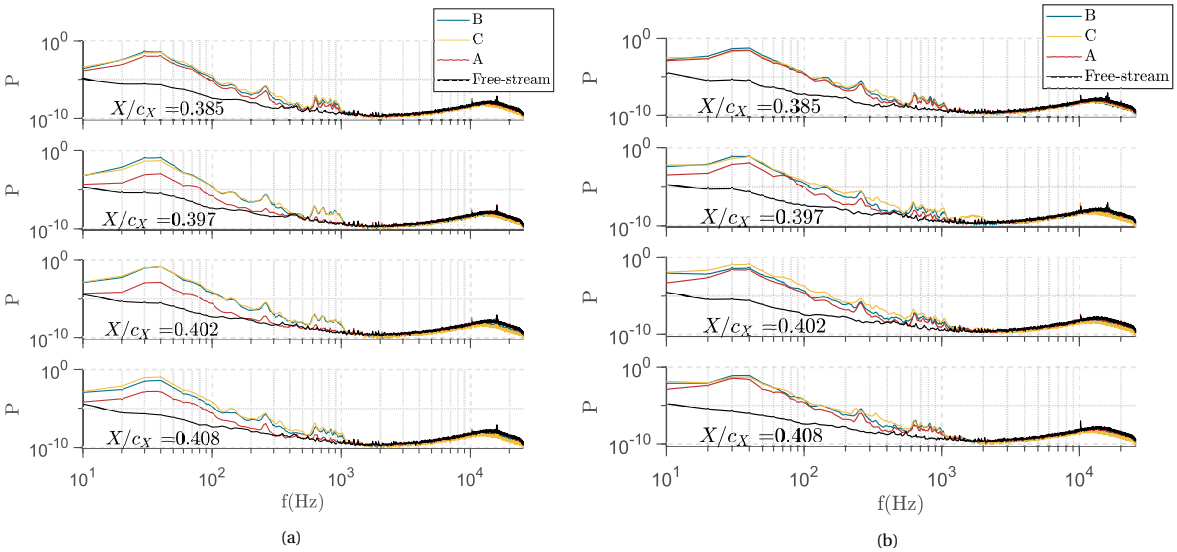

Figure 7.21: Spectral analysis for the probes at A,B C and freestream for the short FFS ($\overline{h}$=0.6 mm) configuration associated with a) lower amplitude forcing (F1) and b) higher amplitude forcing (F2)

The power spectral density at the probed locations (A,B,C) for the clean configuration are presented in Figure 7.20 and for the short FFS configuration in Figure 7.21. In addition, a free stream probe is placed outside the boundary layer to monitor the spectral content of the freestream. Only minor variations are observed among the spectra presented for the lower and higher forcing for the step and clean configurations. This could be attributed to a few

reasons. The steady disturbance profiles presented in Figure 7.14a and Figure 7.15a do not show the characteristic secondary upper lobe which develops as a result of the onset of amplitude saturation in the mean flow. This is corroborated by the absence of strongly modulated mean velocity contours shown in Figure 7.12 and Figure 7.13. Moreover, the measurement planes for this campaign are relatively upstream, close to the step, when compared to the location where transition was seen to occur in Figure 7.3. These factors could contribute to the absence of new peaks in above presented spectral trends. The low frequency ranges identified for the clean configuration for lower amplitude forcing from the preliminary measurements (Figure 6.15) are studied for the current configurations.

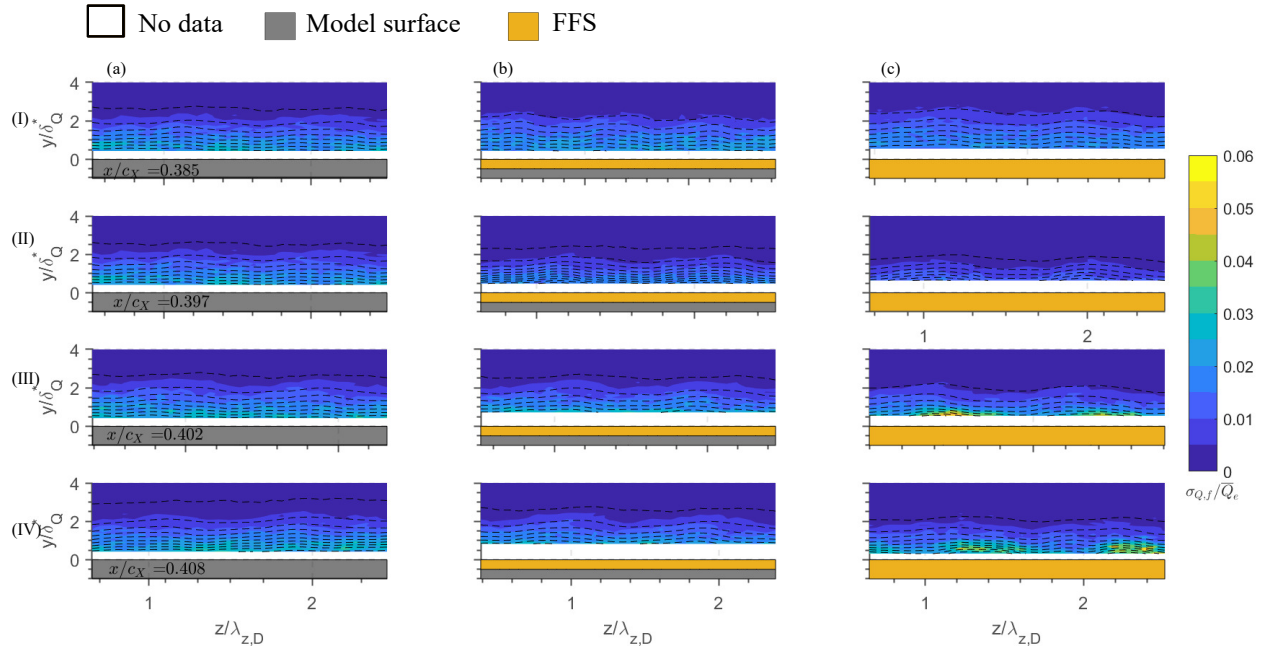

Figure 7.22: Contours of bandpass filtered velocity (BL_1 = 40 - 240 Hz) fluctuation field (12 levels) with dashed lines indicating isolines of mean velocity - F1. a)Clean configuration b) $\overline{h}$ = 0.6 mm c) $\overline{h}$ = 1.3 mm, Re_{c_X} = 1.08E+6

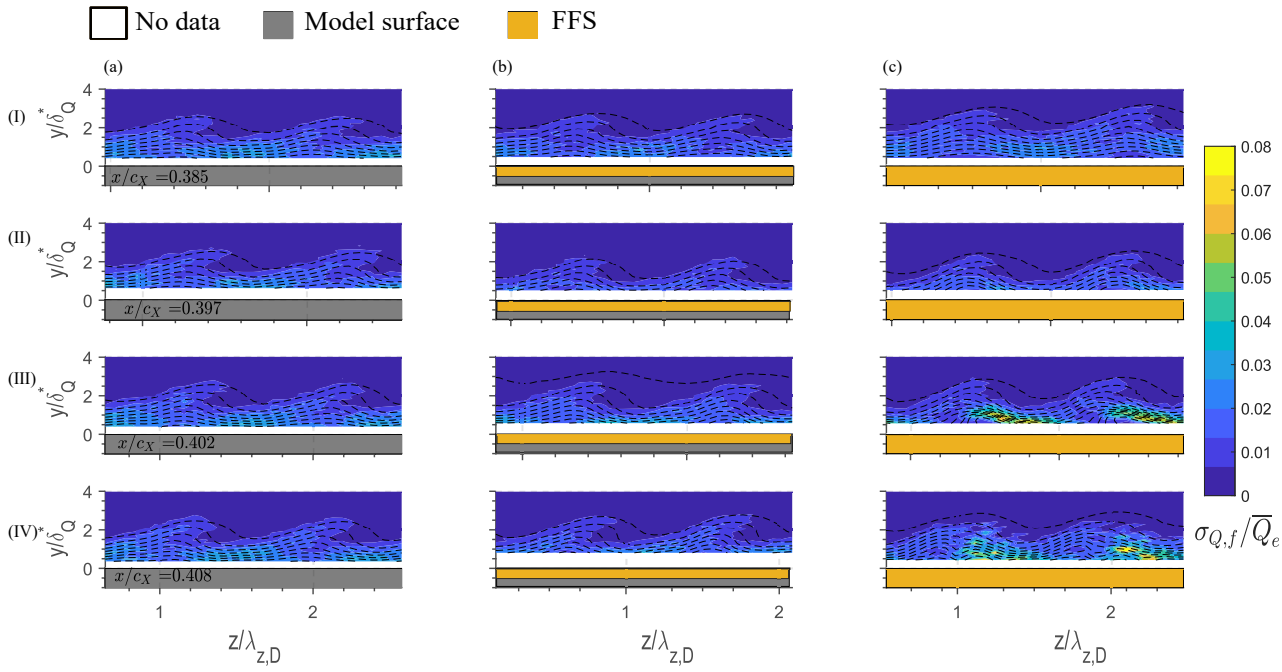

Figure 7.23: Contours of bandpass filtered temporal velocity (BL_1 = 40 - 240 Hz) fluctuations (12 levels) with dashed lines indicating isolines of mean velocity -F2. a)Clean configuration b) $\overline{h}$ = 0.6 mm c) $\overline{h}$ = 1.3 mm, Re_{c_X} = 1.08E+6

Figure 7.22 and Figure 7.23 present bandpass filtered (within B_{L1}, 40 - 240 Hz) contours of temporal velocity fluctuations along with dashed isolines of mean velocity associated with low and high amplitude forcing respectively. In agreement with the bandpass filtered fields illustrated in Figure 6.16, the temporal fluctuations of velocity are found to qualitatively resemble the wall normal gradients presented in Figure 7.18 and Figure 7.19. As discussed for Figure 6.16, the alignment of the fluctuations with the wall normal gradients points to the frequency range being associated with the vibration of the probe.

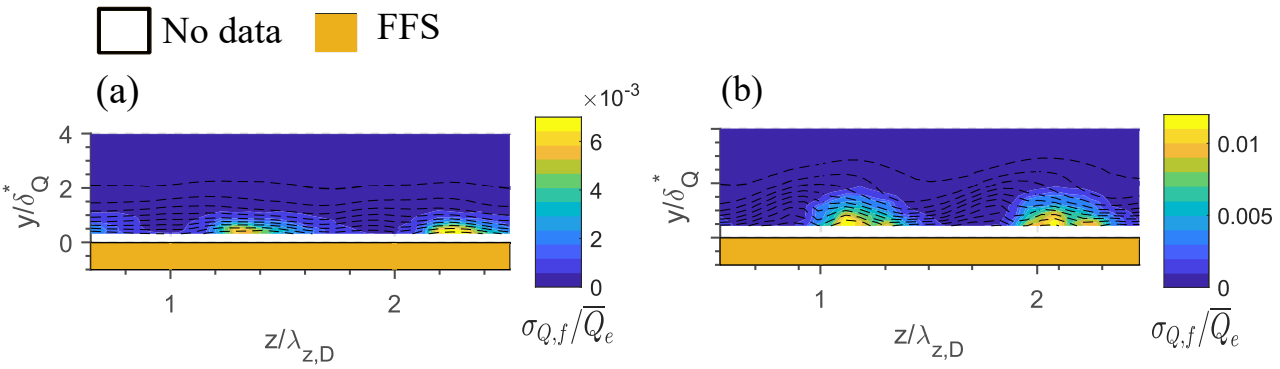

Figure 7.24: Bandpass filtered (BL_2 = 240-310 Hz) temporal velocity fluctuation (12 levels) with dashed lines indicating iso-velocity lines at x/c_X = 0.408 for a) F1 b) F2.Re_{c_X} = 1.08E+6

Figure 7.24 a) and b) present bandpass filtered (within B_{L2}, 240 - 310 Hz) contours of temporal velocity fluctuations along with dashed isolines of mean velocity associated with low and high amplitude forcing, respectively. In agreement with the results presented in Figure 6.16, the temporal fluctuations of velocity are found to appear on the inner side of the upwelling in the vortex for the supercritical step heights at the last plane. The spatial organisation of these fluctuations points to the interaction of travelling and stationary crossflow in the vicinity of the step location.

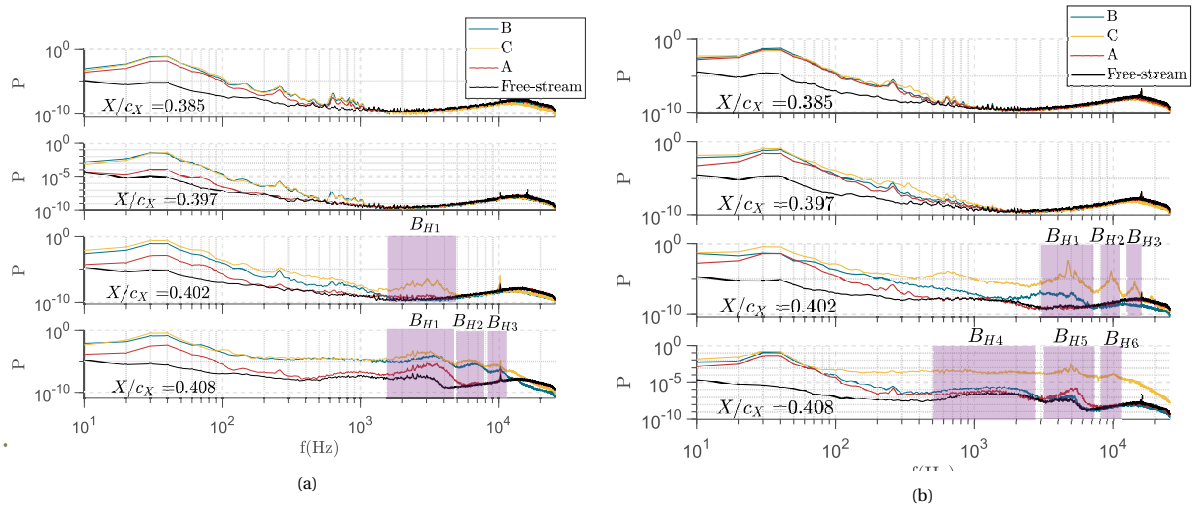

Figure 7.25: Spectral analysis for the probes at A,B C and freestream for the supercritical step 1.3 mm configuration associated with a) lower amplitude forcing (F1) and b) higher amplitude forcing (F2)

When probed within a vortex for the supercritical step configuration, the power spectral density trends are found to exhibit spectral broadening, downstream of the step plane (X/c_X = 0.397). The appearance of new peaks downstream of the step points towards the presence of interesting flow structures in the bandpass filtered plots. The frequency bands around these peaks are delimited and applied to bandpass filter temporal velocity fluctuation field in the figures presented below.

Figure 7.26 presents the bandpass filtered contour of temporal velocity fluctuations at the planes downstream of the supercritical step configuration at a lower amplitude forcing. The frequency band delineated for the plane just downstream of the step (I) from the spectra in Figure 7.25a is 1.6 kHz - 5 kHz. The spatial organisation of the velocity fluctuations shows conjunction with the positive spanwise gradient contours in that plane. However, it

must be noted that the amplitude of fluctuations is low. Although nothing can be conclusively said about this band of fluctuations, it is observed that a bump in the spectrum appears in the same frequency band in the last plane of measurement.

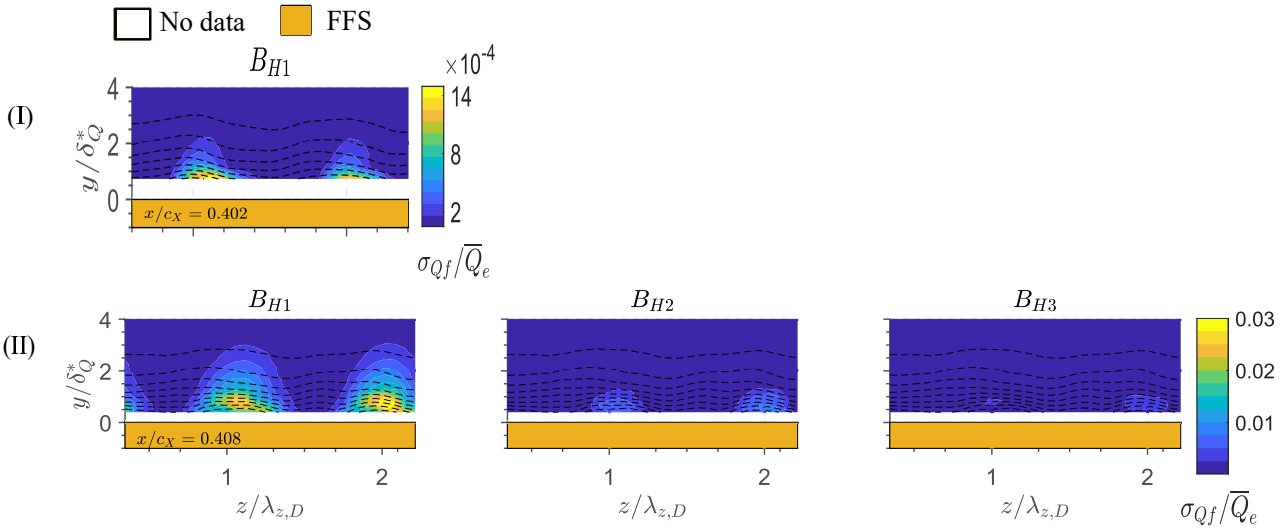

Figure 7.26: Bandpass filtered contours of temporal velocity fluctuations (12 levels) with dashed iso-velocity lines for F1 downstream of supercritical step, B_{H1} : 1.6 - 5kHz, B_{H2} : 5.8 - 8.3 kHz, B_{H3} : 8.5 - 11 kHz.Re_{c_X} = 1.08E+6

At the last plane for the lower amplitude forcing, three frequency bands are identified as B_{H1} : 1.6 kHz - 5 kHz, B_{H2} : 5.8 kHz - 8.3 kHz and B_{H3} : 8.5 kHz - 11 kHz. The contour Figure 7.26 II presents the bandpass filtered velocity fluctuation field within these frequency bands. It is seen that the fluctuations are strongest in the first frequency band. The spatial organization of the structures shows similarity with the previous plane wherein the fluctuations align with the inboard side of the vortex (right) and are stronger close to the wall. Since the first frequency range is comparable to that of the previous plane, it is theorized that onset of an unsteady mechanism in the previous plane pushes energy in the near wall region of the vortex in the last plane.

However, it is important to understand, from the presented mean flow contours, stationary amplitudes, and spectral content that the 1 layer DRE does not serve as a strong enough forcing to study interesting flow features. While the conclusions which can be made with the lower initial amplitude forcing are still ambiguous, the higher amplitude forcing configuration provides a clearer crossflow pattern. This allows for a more definitive identification of the spatial organisation of fluctuations.

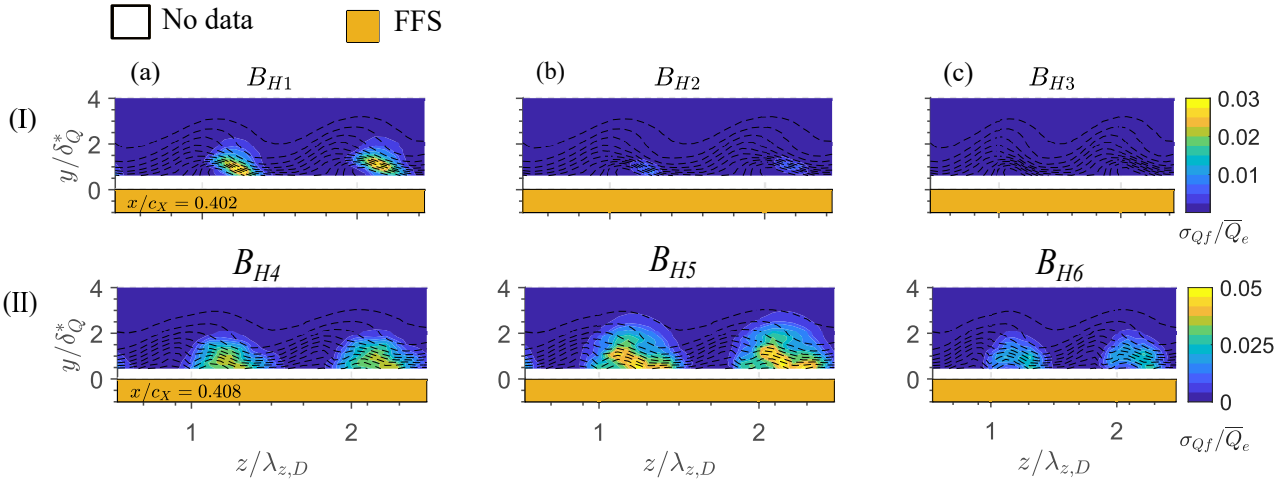

Figure 7.27: Bandpass filtered contours of temporal velocity fluctuations (12 levels) with dashed iso-velocity lines for F2 downstream of a supercritical step. $B_{H1} = B_{H5}$: 3.3 kHz - 6.3 kHz, $B_{H2} = B_{H6}$: 7.7 kHz - 11.5 kHz , B_{H3} : 12.4 kHz - 16.3 kHz and B_{H4} : 0.46 kHz - 2.8 kHz

Figure 7.27 presents the bandpass filtered fluctuation contours for the planes downstream of the supercritical

step configuration. Just downstream of the step (II, $X/c_X = 0.402$) for the higher amplitude forcing (F2), three prominent peaks are identified from Figure 7.25b within the bands, B_{H1} : 3.3 kHz - 6.3 kHz, B_{H2} : 7.7 kHz - 11.5 kHz and B_{H3} : 12.4 kHz - 16.3 kHz. Bandpass filtering the fluctuations within these frequency bands yields stronger fluctuations are presented within the first frequency band B_{H1}. The fluctuations appear within the inner side of the upwelling of the cross flow vortex. The high frequency fluctuations near the wall are found to align with the regions of high wall normal gradient region identified in Figure 7.19 and high spanwise gradient region (R) observed in Figure 7.17. These structures are not associated with any secondary instability, but instead it was reported by Eppink et al. [37] to be associated with flow recirculation downstream of the FFS (also identified by Tufts et al. [48]).

The fluctuations could be a result of vortex shedding attributing to the pressure gradient signature about this plane. The mechanism of vortex shedding is reported by Bhogosian and Cassel [49] to occur where there is an adverse pressure gradient upstream and a favorable pressure gradient downstream. Since a similar pressure gradient signature is found in Figure 7.10b about $X/c_X = 0.402$, the high frequency range B_{H1} could be associated with a vortex shedding mechanism. A similar organisation of fluctuations is also seen in the hot-wire measurements of Rius-Vidales et al. [6] for a supercritical step but for small amplitude forcing in a comparable frequency range (Figure 13 IIId in [6]).

This vortex shedding mechanism is posited to occur from the shear layer of the laminar separation bubble. Hosseinverdi and Fasel [61] in their DNS study, suggested the shedding of vortices in the shear layer to occur by the following steps in two-dimensional flows:

- There occurs an onset roll-up of vorticity in the shear layer upstream of the maximum bubble height.
- The developed vortex grows due to the Kelvin-Helmholtz instability.
- The shedding of this vortex occurs at the maximum bubble height.

The growth of the vortices in the shear layer is corroborated by the increase in crossflow amplitude A_{zFFT} identified in Figure 7.15b.

At the last plane of measurement for the higher amplitude forcing, three frequency bands are identified from Figure 7.25b as follows, B_{H4} : 0.46 kHz - 2.8 kHz, B_{H5} : 3.3 kHz - 6.3 kHz and B_{H6} : 7.7 kHz - 11.5 kHz. From the mean velocity contours in Figure 7.13, breakdown of CF vortices occurs, and loss in the fine structure of the vortices. Furthermore, the spectra Figure 7.25b, shows spectral broadening, associated with the onset of turbulence. From the bandpass filtered contours shown in Figure 7.27 II, the second frequency band B_{H5} yields the highest level of fluctuations with the fluctuations aligned in the same region within the vortices . It should be noted that this frequency band is equal to B_{H1} in $X/C_X = 0.402$. This implies that the vortices could be shed in the second frequency band. The equally high levels of fluctuations in the other two frequency bands could be associated with turbulent fluctuations.

If the vortex shedding frequency range is taken as 3.3 kHz < f_s < 6.3 kHz, the Strouhal numbers for vortex shedding (fL_z/U_e) reported by Eppink [38] is 0.6-0.7. This gives the range of length of the laminar separation bubble 2.3 mm < L_z < 3.9 mm. The Strouhal number for vortex flapping also reported by the author is 0.12-0.2, which gives the flapping frequency range to be 1 kHz < f_s < 1.1 kHz. A low frequency band close to this estimated f_s, is observed in Figure 7.25b for $X/C_X = 0.402$ in the range of 440 Hz-990Hz, where the PSD varies greatly from the clean configuration at the same plane Figure 7.20b. The fluctuations at this frequency band are found to be aligned in the same region as vortex shedding. This implies that a low frequency flapping of the shear layer could also be persistent at $X/C_X = 0.402$.

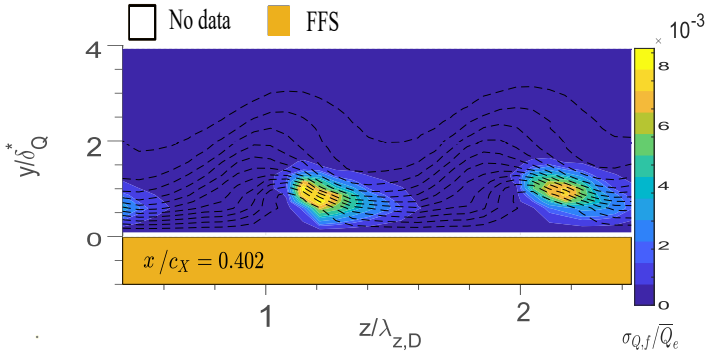

Figure 7.28: Bandpass filtered contours of temporal velocity fluctuations (12 levels) with dashed iso-velocity lines for F2 at $X/c_X = 0.402$ with a supercritical step, 440 Hz < f_F <990 Hz

As a common theme for all the cases studied thusfar, the spectral content was not associated with the presence of secondary instabilities. This is because the Type 1 and Type 2 modes are associated with strong regions of velocity shears which come from amplitude saturation. Wasserman and Kloker [56], in their computational study report the formation of finger vortices starting from the wall and wrapping around the shear layer on the outer side of the upwelling. The mean velocity contours do not show amplitude saturation in the clean configuration, which is also corroborated by the absence of the secondary lobes in the mode shapes presented. This could be linked to the measurement planes under study being located rather upstream of the transition locations from Figure 7.3.

From spectral analysis of the hot-wire data, it has been possible to validate and identify important structures which have been seen in literature. The presence of fluctuations arising from the inner side of the upwelling near the wall paves a new avenue for extensive study. While it was not possible to conclusively indicate the nature of these fluctuations owing to the choice of flow measurement technique in this study, the identification of the frequency bands within which these structures arise, is a first step to understanding the flow structures which arise in the vicinity of the step.

8

CONCLUSIONS AND RECOMMENDATIONS

The demand to improve the aerodynamic efficiency of commercial transport aircraft is constantly rising, owing to the commitments made by the aerospace sector to curtail fuel emissions. In this regard, there have been many researchers directing their efforts towards controlling laminar turbulent boundary layer transition on swept wings, developing active and passive techniques under the umbrella of laminar flow control (LFC). However, to effectively apply LFC in flight environments, the crossflow instability that arise on swept wings needs to be thoroughly understood. Moreover, the interaction of crossflow with forward facing steps that inevitably arise on the wing surface requires deeper understanding.

Drawing upon the recent research efforts of Eppink [38] and Rius-Vidales et al. [6], the research object has been formulated as follows:

To understand the effect of initial crossflow amplitude on the interaction of stationary crossflow vortices with a forward facing step on swept flat plate flow

Preliminary experiments are conducted to characterize the pressure gradient on the novel swept flat plate model. Stability analysis performed with the characterized pressure gradient generates the spanwise wavelength associated with the overall maximum amplified mode. This spanwise wavelength is used to estimate the spacing between the discrete roughness elements (DREs) which in turn is employed to facilitate the conditioning of the crossflow vortices. The hot-wire measurements in the clean configuration without steps, shows distinction in the growth and development of CF vortex structures between the forced and unforced cases. The configuration forced with one layer of DREs is associated with a strong modulation of the mean flow in the mean velocity contours, and monotonic increase in N factors. Moreover, numerically estimated boundary layer thicknesses and the velocity profiles are found to compare well with the experimentally collected data. The mode shapes reveal the presence of a secondary upper lobe indicating the onset of amplitude saturation at the most downstream measurement plane. Spectral analysis is performed to characterize the developing secondary instabilities over the primary crossflow. Although secondary instabilities are not observed, the bandpass filtered fluctuations studied aided in demarcating the low frequency bands associated with probe vibration and the interaction of stationary and travelling crossflow.

The final experiment is performed for the purpose of studying the effect of initial crossflow amplitudes on the interaction of stationary crossflow with steps. Using the data from the preliminary measurements, a convergence test is performed to reduce the measurement time taken for the final hot-wire anemometry study. An estimate of the initial crossflow amplitudes at the step is obtained from a least mean square fit of the growth rate trend from the hot-wire data with the stability solver data. Six initial crossflow amplitudes are chosen from the generated trend. Thermal maps are obtained for the six configurations on varying the step height from the clean case to the tripping step height. When the DRE height is increased, keeping the location of the DREs a constant, the transition locations are found to move upstream for all the step heights. This is attributed to the advancement in the growth, saturation and subsequent breakdown of the crossflow vortices. On keeping the DRE height constant, when the DREs are moved upstream of the neutral point, the transition locations are consistently moved downstream for all the step heights. This downstream movement is attributed to the initial decay of the crossflow vortices up to the neutral point. Similarly, when the DREs are moved downstream of the neutral point, a minor movement of the transition downstream is observed. This is explained by the delay in the growth and breakdown of the crossflow vortices.

Overall, the results of the infrared study paints a clear picture of the movement of the transition front for varying step heights and initial crossflow amplitudes, answering part of the research question posed in section 3.4.

Furthermore, the pressure measurement collected shows the characteristic pressure gradient signature: adverse-favorable-adverse as reported in the computational study of Tufts et al. [48]. Hot-wire anemometry is employed to study the flow near the step for the 1 layer and 2 layer DRE configurations for the clean, short FFS and supercritical step heights. The mean velocity contours associated with the smaller initial amplitude forcing shows breakdown of CF vortices at the most downstream plane for supercritical step configuration. The mean velocity contours associated with the higher initial amplitude forcing presents a stronger modulation of the boundary layer where the breakdown of CF vortices is seen in the second last plane for the supercritical step configuration. The stationary crossflow amplitudes are studied to illustrate the effect of FFS and initial crossflow amplitudes on the steady flow. The crossflow vortices are found to show notable growth in the case of higher initial amplitude forcing.

Under these forcing conditions, the contours of bandpass filtered fluctuations reveal a significant region where the velocity fluctuations align with the regions of high wall normal and spanwise shear, which point to the presence of vortex shedding for the supercritical step as reported previously in Rius-Vidales et al. [6] and Eppink et. al. [37]. It has been postulated in this study that the shear layer developing on the recirculation region downstream of the FFS edge, sheds vortices at a frequency 3.3 Hz<$f_{shedding}$<6.3 Hz. From the shedding frequency, the length of the recirculation region is estimated to be 2.3 mm< l <3.9 mm, based on the Strouhal number range reported by Eppink [38]. From the estimated length of the separation bubble, a flapping frequency range is estimated to be 1 Hz<f_f<1.1 Hz again from another Strouhal number range reported by the same author. The band closest to this estimate where the spectra of the supercritical step differs most from the spectra of the clean configuration is identified at 440 Hz<$f_{flapping}$<990 Hz, wherein the bandpass filtered fluctuations are found to align with the near wall region of importance.

The spectral peaks studied for the above cases show no presence of secondary instability. This is attributed to the upstream location of the measurement planes when compared to the location of transition for the clean configuration as identified from the thermal maps. Since the unsteady effects in this study are only discernible when the flow interacted with the supercritical step, the absence of prominent unsteady effects associated with lower step heights and the clean configuration can be explained by a weaker or lack of flow recirculation on the FFS edge. This could impede the presence of vortex shedding. Furthermore, conclusions from spectral data could not be made for the lower amplitude forcing, due to the relatively insignificant amplitudes that crossflow vortices reach at the location of the step. The spectral analysis of the hot-wire data provides insight into the complex unsteady mechanisms at play on the novel swept flat plate. The presence of similar structures identified in literature points to the reliability of the observed phenomena, and thus, answering the other part of the research question posed in section 3.4.

While important features in the vicinity of the step have been identified and studied in this research work, more conclusive evidence is needed for a definite picture of the transition process. As it has been identified that the amplitudes reached by the crossflow vortices at the step are very low with one layer of DREs, it is recommended to employ atleast two layers of DREs to generate sufficiently strong crossflow vortices.

In this study, the limitations of hotwire anemometry as a flow measurement technique are highlighted when the presence of recirculation regions could not be validated. Moreover, since the technique only measures the resultant velocity, it was not possible to measure and validate the velocity profiles of the individual components, in this three dimensional boundary layer flow. Stereo particle image velocimetry (SPIV) should provide more comprehensive picture of the flow with its ability to image flow reversal regions and the measurement of the individual velocity components. A combined HWA and SPIV study would be beneficial in obtaining a spatio-temporal picture of the flowfield.

While the present research work explores the effect of varying DRE height on the crossflow vortices in the vicinity of the step, the effect of varying DRE locations on the flow field further downstream of the step location could be a possible research avenue for future work. This could help further the understanding behind the observed non-linearity in the transition location trends post the short FFS for F2 and F6 cases. On exploring the flowfield further downstream of the step, interesting spectral content is expected to be seen for the clean configuration afnd short FFS.

The extension of this research works in different wind tunnel environments and models could provide more insight on whether the observations are consistent across different conditions. This would paint a more conclusive picture on the unsteady interactions that occur in the presence of steps.

BIBLIOGRAPHY

[1] Drake A., Bender A.M., and Westphal R.V. “Transition due to surface steps in the presence of favorable pressure gradients”. In: *AIAA 2008-7334* (2008).

[2] Sciacchitano A. and Wieneke B. “Piv uncertainty propagation”. In: *Measurement Science and Technology,Vol. 27 (8)* (2016).

[3] Rius-Vidales A.F. and Kotsonis M. “Effect of Two-Dimensional Surface Irregularities on Swept Wing Transition: Forward Facing Steps”. In: *AIAA-3075* (2018).

[4] Rius-Vidales A.F. and Kotsonis M. “Impact of a forward-facing step on the development of crossflow instability”. In: *Journal of fluid mechanics 924(A):34* (2021).

[5] Rius-Vidales A.F. and Kotsonis M. “Influence of a Forward-Facing Step Surface Irregularity on Swept Wing Transition”. In: *AIAA Volume 58, Number 12* (2020).

[6] Rius-Vidales A.F. and Kotsonis M. “Unsteady interaction of crossflow instability with a forward-facing step”. In: *Manuscript submitted for revision* (2021).

[7] Thomas A.S.W. “Aircraft drag prediction and reduction”. In: *AGARD Report no.723* (1985).

[8] Holmes B. “Manufacturing tolerances for natural laminar flow airframe surfaces”. In: (1985).

[9] Muller B. and Bippes H. “Experimental study of instability modes in a three dimensional boundary layer”. In: *Fluid dynamics of three dimensional turbulent shear flows and transition, AGARD CP 438, pp.1-15. NATO AGARD* (1989).

[10] Jones B.M. “Flight experiments on the boundary layer”. In: *Journal of Aerospace sciences,Vol. 5(3), pp.81–94* (1938).

[11] Arnal D. and Casalis G. “Laminar-turbulent transition prediction in three-dimensional flows”. In: *Progress in Aerospace Sciences.,Vol.36, pp.173-191* (2000).

[12] Bushnell D.M. “Aircraft Drag Reduction - A review”. In: *Proceedings of the institute of mechanical engineers, Part G: Journal of Aerospace engineering* (2003).

[13] White E., Saric W., Gladden R., and Gabet P. “Stages of swept wing transition”. In: *AIAA-0271* (2001).

[14] White E.B. and Ergin F.G. “Using laminar -flow velocity profiles to locate the wall behind roughness elements”. In: *Experiments in fluids, Vol.36, pp.805-812* (2004).

[15] White E.B. and Saric W.S. “Secondary instability of crossflow vortices”. In: *Journal of fluid mechanics* (2005).

[16] Cooke E.E., Mughal S., Sherwin S.J., Ashworth R., and Rolston S. “Destabilization of stationary and traveling crossflow disturbances due to steps over a swept wing”. In: *AIAA Paper 2019-3533* (2019).

[17] Houghton E.L., Carpenter P.W, Collicott S.H., and Valentine D.T. *Aerodynamics for Engineering Students (Seventh Edition)*. Seventh Edition. 2017, pp. 591–634.

[18] Scarano F. “Experimental aerodynamics course notes”. In: (2004).

[19] Collier F.S. “An overview of recent subsonic laminar flow control flight experiments”. In: *AIAA Pap. No. 93-2987* (1993).

[20] Zoppini G. “Experimental Investigation on Receptivity of Crossflow Instability to Discrete Roughness Amplitude and Location”. In: *AIAA Scitech* (2021).

[21] Duncan G.T., Crawford B.K., Tufts M.W., Saric W.S., and Reed H.L. “Effects of Step Excrescences on a Swept Wing in a Low Disturbance Wind Tunnel”. In: *AIAA SciTech Forum* (2014).

[22] Boeing Commercial Airplane Group. “High Reynolds number hybrid laminar flow control (HLFC) flight experiment: final report”. In: *Vols I–VI, D6-55648-1 to D6-55648-6.* (1993).

[23] Bippes H. “Basic experiments on transition in three-dimensional boundary layers dominated by crossflow instability”. In: *Progress in Aerospace Sciences, Vol.35, pp. 363-412* (1999).

[24] Deyhle H. and Bippes H. “Disturbance growth in an unstable three dimensional boundary layer and its dependence on environmental conditions”. In: *Journal of Fluid Mechanics, Vol. 316, pp.73-113* (1996).

[25] Reed H., Saric W., and Arnal D. “Linear stability theory applied to boundary layers”. In: *Annual Review of Fluid Mechanics* (1996).

[26] Schlichting H. *Boundary layer theory*. 1968. ISBN: 9780070553293.

[27] Bruun H.H. *Hot Wire Anemometry : Principles and signal analysis*. 1996. ISBN: 0198563426.

[28] Coleman H.W. and Steele G.W. *Experimentation, validation, and uncertainty analysis for engineers*. 2018. ISBN: 9781119417668.

[29] Casacuberta J., Hickel.S, and Kotsonis M. “Mechanisms of interaction between stationary crossflow instabilities and forward-facing steps”. In: *AIAA SciTech Forum* (2021).

[30] Crouch J., Kosorygin V., and Ng L. “Modelling the effects of steps on boundary layer transition”. In: *Govindarajan R. (eds) IUTAM Symposium on Laminar-Turbulent Transition, Fluid Mechanics and Its Applications, vol.78, pp.37-44* (2006).

[31] Matishek J. “Introduction to the Aerion supersonic business jet.” In: *Canadian Aeronautics and Space Inst. Symp.* (2007).

[32] Perraud J. and Serraudie A. “Effects of steps and gaps on 2D and 3D transition”. In: *European Congress on Computational Methods in Applied Sciences and Engineering ECCOMAS* (2000).

[33] Serpieri J. “Crossflow instability : flow diagnostics and control of swept wing boundary layers”. In: (2018). DOI: 10.4233/uuid:3dac1e78-fcc3-437f-9579-048b74439f55.

[34] Serpieri J. and Kotsonis M. “Three-dimensional organisation of primary and secondary crossflow instability”. In: *Journal of Fluid Mechanics, vol. 799, pp. 200-245*. (2016).

[35] Thibert J., Reneaux J., and Schmitt V. “Onera activities on drag reduction”. In: *17th Congress on International Council of the Aeronautical Sciences* (1990).

[36] Van-Ingen J., Smith A.M., and Gamberoni N. “A suggested semi-empirical method for the calculation of the boundary layer transition region Transition, Pressure Gradient and Stability Theory”. In: *Tech. Rep. ES, vol.26, issue.4, p.388* (1956).

[37] Eppink J.L. “High-Frequency Secondary Instabilities Downstream of a Forward-Facing Step”. In: *AIAA - 2243* (2020).

[38] Eppink J.L. “Mechanisms of stationary cross-flow instability growth and breakdown induced by forward-facing steps”. In: *Journal of fluid mechanics 897 A15* (2020).

[39] Eppink J.L. “Mechanisms of stationary cross-flow instability growth and breakdown induced by forward-facing steps”. In: *Journal of fluid mechanics, Vol.897* (2020).

[40] Eppink J.L. “The effect of forward-facing steps on stationary crossflow instability growth and breakdown.” In: *AIAA 2018-0817* (2018).

[41] Eppink J.L. and Casper C. “Effects of Forward-Facing Step Shape on Stationary Crossfow Instability Growth and Breakdown”. In: *AIAA Paper-3532* (2019).

[42] Eppink J.L. and Wlezien R. “Data analysis for the NASA/Boeing Hybrid laminar flow control crossflow experiment”. In: *AIAA - 3879* (2011).

[43] Floryan J.M. “On the Gortler instability of boundary layers”. In: *Prog. Aerospace Sci. Vol. 28, pp. 235-271* (1991).

[44] Dagenhart J.R. and Saric W.S. “Crossflow stability and transition experiments in swept wing flow”. In: *NASA Tech. Pub - 209344* (1999).

[45] Mack L.M. “Boundary-layer linear stability theory.” In: *AGARD Rep. No. 709* (1984).

[46] Schrader L.U., Brandt L., Mavripilis C., and Henningson D.S. “Receptivity to free-stream vorticity of flow past a flat plate with elliptic leading edge”. In: *Journal of fluid mechanics* (2010).

[47] Costantini M., Risius S., and Klein C. “Experimental Investigation of the Effect of Forward-facing Steps on Boundary Layer Transition”. In: *Procedia IUTAM, Vol. 14,pp. 152-162,* (2015).

[48] Tufts M., Reed H.L., Crawford B.K., Duncan G., and Saric W.S. “Computational Investigation of Step Excrescence Sensitivity in a Swept Wing Boundary Layer”. In: *AIAA - 2775* (2015).

[49] Boghosian M.E. and Cassel K.W. “On the origins of vortex shedding in two-dimensional incompressible flows”. In: *Theoretical and Computational Fluid Dynamics 30(6), pp. 511–527* (2016).

[50] Malik M.R., Li F., Choudhari M., and Chang C.L. “Secondary instability of crossflow vortices and swept wing boundary layer transition”. In: *Journal of fluid mechanics, vol. 399, pp. 85-115* (1999).

[51] Reibert M.S., Saric W.S., Carrillo R.B., and Chapman K.L. “Experiments in nonlinear saturation of stationary crossflow vortices in a swept-wing boundary layer.” In: *AIAA Paper 96–0184.* (1996).

[52] Morkovin M.V. “Critical evaluation of transition from laminar to turbulent shear layers with emphasis on hypersonically travelling bodies”. In: *Report AFFDL-TR-68-149* (1968).

[53] Beck N., Landa T., Seitz A., Boermans L., Liu Y., and Radespiel R. “Drag reduction by laminar flow control”. In: *Energies, Vol. 11, pp. 252* (2018).

[54] Otsu N. “A threshold selection method from gray-level histograms”. In: *IEEE transactions on systems, man, and cybernetics, Vol. 9, No. 1, pp. 62–66.* (1979).

[55] Stoica P. and Moses R. *Spectral analysis of signals.* 2005. ISBN: 0-13-113956-8.

[56] Wassermann P. and Kloker M. “Mechanisms and passive control of crossflow induced transition in a three dimensional boundary layer”. In: *Journal of fluid mechanics* (2002).

[57] Klebanoff P.S., Tidstrom K.D., and Sargent L.M. “The three-dimensional nature of boundary-layer instability”. In: *Journal of Fluid mechanics.,Vol.1, pp.1-34* (1962).

[58] Radeztsky R.H., Riebert M.S., and Saric W.S. “Effect of Isolated micro sized roughness on transition in swept wing flows”. In: *AIAA J 37(11), pp.1370-1377* (1999).

[59] Downs R.S. and White E.B. “Free-stream turbulence and the development of cross-flow disturbances”. In: *Journal of Fluid Mechanics, Vol. 735, pp.347-380* (2013).

[60] Butterworth S. “On the theory of filter amplifiers.” In: *Experimental Wireless and the Wireless Engineer Vol.7, pp.536–541* (1930).

[61] Hosseinverdi S. and Fasel H.F. “Direct Numerical Simulations of Laminar-to-Turbulent Transition in Laminar Separation Bubbles in Three-Dimensional Boundary-Layer”. In: *AIAA* (2016).

[62] Saddoughi S.G. and Veeravalli S.V. “Hot-wire anemometry behaviour at very high frequencies”. In: *Measurement science and technology 7 (10) 1297–1300* (1996).

[63] Herbert T. “Secondary instability of boundary layers”. In: *Annual Review of Fluid Mechanics.,Vol.20, pp.487-526* (1988).

[64] Saeed T.I., Mughal M.S., and Morrison J.F. “The Interaction of a Swept-Wing Boundary Layer with Surface Excrescences”. In: *AIAA 2016-2065, Session: Incompressible Flow Transition* (2016).

[65] Haynes T.S. and Reed H.L. “Simulation of swept-wing vortices using nonlinear parabolized stability equations.” In: *Journal of Fluid Mechanics, 405, 325–349.* (2000).

[66] Pfenninger W. “Laminar flow control—laminarization”. In: *Special course on drag reduction. AGARD report 654* (1977).

[67] Pfenninger W. and Bacon J.W. “Amplified boundary layer ocscillations and transition at the front attachment line of a 45o swept flat nosed wing with and without boundary layer suction”. In: *Wells C.S. (eds) Viscous Drag Reduction* (1969).

[68] Young W. and Budynas R.G. *Roark’s Formulas for Stress and Strain.* McGraw Hill, 2002.

[69] Gray W.E. “The effect of wing sweep on laminar flow”. In: *RAE TM Aero 256* (1952).

[70] Saric W.S. “Gortler vortices”. In: *Annual Review of fluid mechanics, Vol.26, pp.379-409* (1994).

[71] Saric W.S., Carpenter A.L., and Reed H. “Passive control of transition in three-dimensional boundary layers, with emphasis on discrete roughness elements”. In: *Phil. Trans. R. Soc. A 2011 369* (2011).

[72] Saric W.S. and Reed H.L. “Toward Practical Laminar Flow Control- Remaining Challenges”. In: *AIAA Paper-2311* (2004).

[73] Saric W.S., Reed H.L., and White E.B. “Stability and transiton of three dimensional boundary layers”. In: *Annual Review of Fluid Mechanics,Vol. 35, pp. 413–40* (2003).

[74] Kachanov Y. “Physical mechanisms of laminar boundary layer transition”. In: *Annual Review of Fluid Mechanics.,Vol.26, pp. 411-82* (1994).

[75] Kohama Y. “Three-dimensional boundary layer transition on a concave-convex curved wall”. In: *IUTAM Symp. Turbulence Management and Relaminarization, India, pp. 215-226* (1987).

[76] Wang Y.X. and Gaster M. “Effect of surface steps on boundary layer transition”. In: *Experiments in fluids, vol.39, pp.679-686* (2005).